F I N A L   R E P O R T

Nondestructive Method to Detect Corrosion of Steel Elements in Concrete

Marcelo DaSilva, Graduate Student

Saeed Javidi, Graduate Student

Aaron Yakel, Ph.D., Research Associate

Atorod Azizinamini, Ph.D., P.E.

National Bridge Research Organization (NaBRO)

(http://www.NaBRO.unl.edu)

Department of Civil Engineering

College of Engineering and Technology

W150 Nebraska Hall

Lincoln, Nebraska 68588-0528

Telephone (402) 472-3462

Fax (402) 472-6658

April, 2009

Table of Contents

Chapter 3   37

Finite Element Modeling of Magnet and Damaged Rebar   37

List of Figures

List of Tables

Acknowledgement

Executive Summary

This report provides an outline of a novel approach, methodology, and equipment needed to detect corrosion of any steel element that is embedded in the concrete bridges. Further, within this project, a complete non-destructive system is developed that can detect the presence and extent of corrosion in any steel elements in concrete bridges. Possible applications include:

a) Detecting corrosion of reinforcing bars in concrete deck

b) Detecting corrosion of prestressing strands in prestressed girders

c) Detecting corrosion of prestressing strands in post tensioned concrete bridges and placed in steel or plastic duct

d) Evaluating the condition of bridge deck with respect to corrosion

The method is specifically developed for post tension concrete bridges, which is the most challenging condition. Application to other conditions will be an easy transition.

The method is referred to as non-destructive since it can detect the presence of corrosion without drilling holes or similar approaches for visual inspection. It is in that sense a "blind" technique, where condition of the embedded steel is assessed similar to taking x-ray or having an MRI on human body.

The foundation of the method is based on a simple concept in physics called The Hall effect. The principle is based on creating a magnetic field around the embedded steel element and studying the resulting magnetic field changes using Hall-effect sensors. The idea is that the magnetic field will change in the presence of corrosion.

The development of the concept and non-destructive equipment started with a very primitive device and evolved into a system that can be applied to field conditions.

A series of laboratory tests were carried out to develop the methodology and the non-destructive device itself. An extensive amount of numerical analyses were carried out to comprehend the meaning of different signal types that were being obtained from the non-destructive device. Finally, limited field studies were carried out to develop a comprehensive methodology adoptable to field conditions.

Corrosion of steel reinforcing bars or strands in concrete bridges present a great challenge for inspection and safety evaluation of these structures. The non-destructive equipment and associated methodology developed in this project allows effective and rapid assessment of bridges for the presence of corrosion.

Chapter 1

Introduction

Detecting corrosion in embedded steel elements is of great interest to many bridge owners. The challenge is being able to detect partial, as well as extensive corrosion on these steel elements. The loss of these steel elements, such as strands, may cause partial or even complete collapse of bridge structures. Fortunately, the inherent conservatism in design has provided additional factors of safety beyond that implied by governing codes.

1.1 Background of the Magnetic-Based Method

Various non-destructive evaluation techniques (NDT) are available to evaluate existing concrete structures to detect corroded strands and/or rebars embedded in concrete. Magnetic Flux Leakage (MFL) is a non-destructive testing method which was first developed in the late 1970s to allow inspection of prestressed concrete bridges (1-2). The instrumentation was subjected to evaluation and upgrade through the years. Various data analysis techniques were developed to aid the interpretation of relevant test results. Many research studies have been carried out to detect corrosion in tendons using the MFL method.

The study performed by Ghorbanpoor et al. (3) has shown the promise of the methodology for detecting corrosion in post-tensioned concrete bridges. Ghorbanpoor concluded that MFL signals from flaws in test specimens of prestressing steel could be identified by studying the signal amplitude. Flaws were recognizable when the flaw size was larger than approximately 10 percent of the cross-sectional area of the specimen. With flaws smaller than 10 percent of the cross sectional area, the correlation method -- a signal analysis method based on the correlation concept -- was shown to be effective (3). A study comparing residual magnetic field measurements to magnetic flux leakage measurements, as a method to detect broken prestressing steel, was done by Makar, J. M. et al. (4). According to this investigation, analyses of two and three dimensional

magnetic field plots show that the residual magnetic field technique is capable of detecting breakage of a single wire in a seven-wire strand located up to 70 mm from the cable surface. H. Scheel and B. Hillemeier (5) in Germany used the MFL method and reported that the parameters associated with fractured wires are quantitatively identifiable in the laboratory. They also reported application of the method in the field.

1.2 MFL Theory

Magnetism is caused by the presence of molecular current loops, which is caused by two phenomena: the motion of electrons within the atoms and the spin direction of the electrons within the magnet material. In the presence of a magnetic field, a moving charge has a magnetic force exerted upon it. The relationship that governs the force on moving charges through a magnetic field is called Faraday's Law and implies that as a charge q moves with a velocity $\mathbf{V}$ in a magnetic field $\mathbf{B}$, it experiences a magnetic force $\mathbf{F}$. The U.S. unit of magnetic field is the Gauss (1 T "one Tesla" is equal to 10,000 G).

$$\mathbf{F} = q \cdot \mathbf{V} \cdot \mathbf{B}$$

where:

    $\mathbf{F}$ = Magnetic force

    q = Charge

    $\mathbf{V}$ = Velocity

    $\mathbf{B}$ = Applied magnetic field

When a magnetic field comes near ferromagnetic (steel) material, the magnetic flux lines will pass through the steel bar (9) because the steel offers a path of least resistance due to high magnetic permeability compared to the surrounding air or concrete. When discontinuities of defects (corrosion) are present, this low resistance path becomes blocked and the remaining steel may become saturated, forcing some of the flux to flow through the air. Figure 1-1 shows the schematic of these fluxes. In fact, total saturation is not required for detection as orientation of the magnetic field can be altered by even small levels of corrosion. However, there is a saturation level at which all dipoles are aligned and no further alignment is possible. At saturation level, the following relationship is valid:

$$\mathbf{B} = \mu \cdot \mathbf{H}$$

where:

$\quad$ $\mathbf{B}$ $\quad$ = Magnetic flux (weber/m^2)

$\quad$ μ $\quad$ = Magnetic permeability of the material (weber/ampere meter)

$\quad$ $\mathbf{H}$ $\quad$ = Magnetic field strength (ampere/meter)

$\quad$ To use the concept of MFL as a non-destructive evaluation (NDE) tool, the device must have the ability to measure changes in the path of magnetic field force lines near a ferromagnetic material. Such changes in the components of the flux can be detected by one or more sensors and can be analyzed to determine the extent or severity of the flaw.

$\quad$ Hall-effect sensors are often used to detect and measure MFL. The sensors are made with semi-conductor crystals that when excited by a passage of current perpendicular to the face of crystal, react by developing a voltage difference across the two parallel faces. The possibility of fabrication of those sensors at any size allows the detection of small flaws on the steel.

$\quad$ There are two primary methods for detecting these field anomalies. These methods are referred to as active and residual.
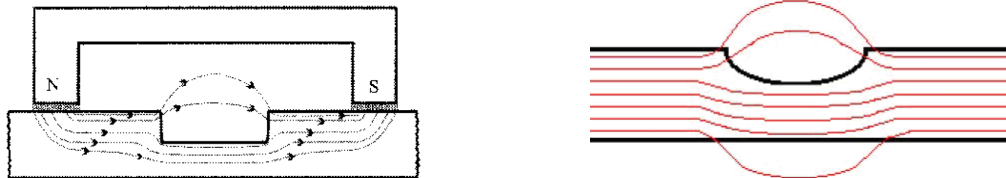
Figure 1-1: The schematic of changes in flux in the location of the corroded area of the strands in active and residual methods

1.2.1 Active Magnetic Flux Leakage Method

$\quad$ In the active method, the sensors are placed between the poles of the magnet and readings are obtained as the device is passed over the specimen. This is the method depicted on the left in Figure 1-1. Because the amount of flux in the ferrous materials depends on the magnetic field near the materials, the location of the magnet and the magnitude of the field are the main variables that significantly affect the signals collected. The measured magnetic flux can be affected by many variables. These include concrete cover, type of duct used (steel versus plastic), distance between the ducts,

number of strands in the duct, level of corrosion, transverse reinforcement in the vicinity of the corroded area, level of tension force in the steel strands and the distance between the sensor and the corrosion point. The interaction among these parameters is very complex and adds to the difficulty of interpreting the signals obtained. In addition, it is very important that the metal become magnetically saturated. If the object to be inspected is not close to saturation, no field will leak from the defects and no flux lines will be able to travel within the surrounding metal. Consequently, no corrosion will be detected.

1.2.2 Residual Magnetic Flux Leakage Method

In the residual system, the specimen is first magnetized, and then the device is passed over the system to read the residual magnetic field. Figure 1-1 (right) show the flux lines after the magnetic passes over the metal. Usually, the active MFL method is appropriate when there are large areas of corroded regions. However, when the corroded area is small, the active MFL approach is no longer effective. Even though, little published work exists about residual MFL, probably because of the comparatively weak leakage flux signals, which require sensitive detectors. The introduction of the residual MFL method was primarily meant to detect areas of small corrosion. In this approach, the detection of a corroded area is accomplished in two stages. First, all strands and bars are magnetized by a magnet; then, the device is passed over the surface of the concrete to measure the residual magnetic flux.

1.3 Scope of the Study

This report presents the development of a non-destructive device and testing procedures that utilize magnetic flux leakage theory to detect the corrosion of reinforcing and prestressing steel embedded within concrete. Most of the effort in the current study was devoted to the development and fabrication of the new MFL device. An extensive numbers of laboratory tests were carried out in order to evaluate the condition of reinforcing and prestressing steel with manmade flaws and corrosion. Results from the laboratory tests are here presented and discussed.

1.4   Organization

This report provides information on the development of a nondestructive evaluation (NDE) device for assessing the condition of steel embedded in concrete.

This report begins with an introduction and a review of the magnetic flux theory previously described in this chapter.

Chapter 2 provides a detailed summary on the earliest stage of development of a non-destructive device capable of detecting corrosion.   Different magnetic configurations, sensor arrangements and a wide number of specimens were tested and their results analyzed.

Chapter 3 contains the results from numerical simulations obtained using the finite element method. In addition, a parametric study was carried out to determine the variables that influence the magnetic field associated with the MFL technique. A finite element model of the best magnet shape was created to better comprehend the behavior of magnetic flux through the steel.

Chapter 4 discusses the results obtained using the MFL device with three Hall-effect sensors. The corrosion at this stage was simulated with a full cross section loss. In addition, the presences of transverse rebars are here considered. The results are presented and discussed.

Chapter 5 concentrates on the results using an MFL device with 15 Hall-effect sensors. A detailed description of the final MFL device is presented. A total of 14 different situations were simulated. A wood frame covered by plywood was designed to keep all parts including ducts, transverse rebars, longitudinal rebars, and strands in place. Two different heights of the sensors were considered.

Chapter 6 is devoted to experiments that consider strands with actual corrosion. The corrosion was obtained using electrolysis method. Comparison between the signal obtained by discontinuous and corroded strands are discussed. The MFL device was capable of determine the location of the corroded region with 8% and up of loss.

The report finishes with the conclusions and recommendations for further researchers. Three appendices have additional information related to the laboratory tests and a denoising technique, which could be applied to the signal to remove the rebar influence.

Chapter 2

Development of a Non-Destructive Device

2.1 Introduction

This chapter summarizes initial attempts in the investigation of the merits of the magnetic flux leakage method and the development of early versions of the non-destructive device.

2.2 Description of MFL Devices

The early versions of the non-destructive device developed under this study are comprised of a magnetic field source, a series of magnetic field detection sensors, electrical control devices and circuits and a multimeter device. A significant portion of the effort of this study was devoted to the development of the magnetic field source and the best sensor arrangement. The material presented here addresses the details of the magnetic field source, along with all relevant components that compose the MFL device. Five different magnet configurations were developed and the results are here presented and discussed.

2.2.1 Magnet Configuration No. 1

The earliest version of the magnet is shown in Figure 2-1. Magnet configuration no. 1 (MC1) consists of a series of rectangular-shaped magnets inserted between two steel plates. The magnet type used was hard ferrite ceramic grade 8. The dimensions of each magnet were 6" x 4" x 1", with a residual flux density of 3,900 Gauss where the North and South Poles of each magnet were located on each 6" x 4" surface, respectively. Four wheels were attached to the device, allowing the equipment to move during testing. One Hall-effect sensor was placed underneath the magnets to measure the magnetic field. The components that compose the MC1 are identified in Figure 2-1.

Four different variations of MC1 were evaluated. The considered quantities for each variation were three, five, seven and nine magnets. Figure 2-2 shows MC1 with nine magnets.
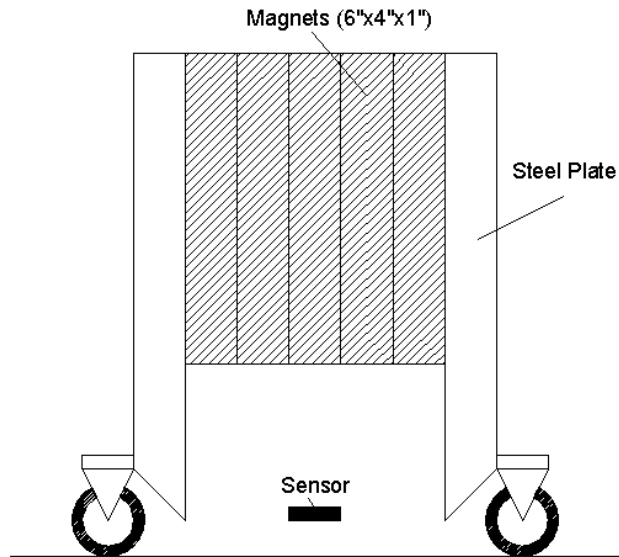
Figure 2-1: Drawing of magnet configuration no. 1

Figure 2-2: Magnet configuration no. 1 with nine magnets

2.2.2 Magnet Configuration No. 2

Figure 2-3 shows the drawing of magnet configuration no. 2 (MC2), which consists of magnets stacked vertically, and attached to a movable cart similar to the previous configuration. At this stage, the magnetic type was replaced by neodymium. Each magnet was 2" x 1" x 1/2" in size, with a residual flux density of 12100 Gauss. The North and South Poles of each magnet were located on opposite faces, having a 2" x 1" dimension. One Hall-effect sensor was placed underneath the magnets as shown below.
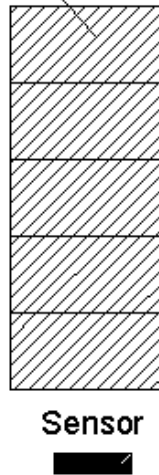
Figure 2-3: Drawing of magnet configuration no. 2

2.2.3 Magnet Configuration No. 3

Figure 2-4 identifies the components of magnet configuration no. 3 (MC3). Configuration no. 3 consists of magnets stacked in a "U" shape. V-shaped spacers, made of 1010 alloy, were used to obtain the desirable curvature. The magnetic yoke was placed upside down on a wood board such that the poles were parallel to the longitudinal axis of the specimens. The magnet type used was the same used in configuration no. 2. MC3 was later modified by increasing the number of magnets. Figure 2-5 shows the two groups of 15 sensors used to measure the magnetic field. Sensor group B was placed under the U-shaped magnet, while sensor group A was placed adjacent to the magnets.

The number of active sensors was varied according to each test. For each point, the results from all active sensors were added and then plotted. No wheels were used in this configuration.
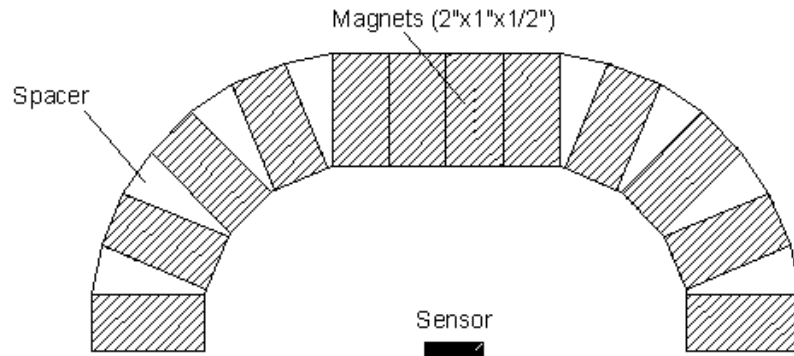
Figure 2-4: Drawing of magnet configuration no. 3
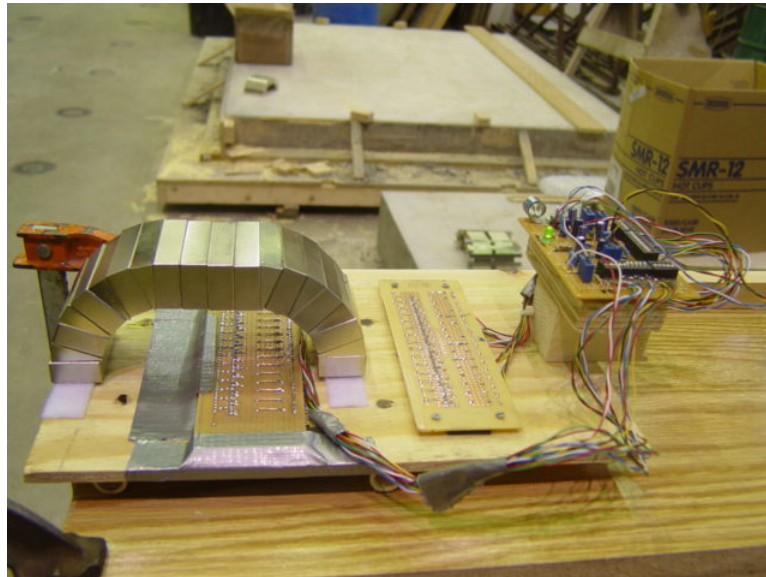
Figure 2-5: Magnet configuration no. 3

2.2.4 Magnet Configuration No. 4

Figure 2-6 shows magnet configuration no. 4 (MC4). For this arrangement, another stack of magnets, with the same magnetic properties of MC3, were added. A gap of 1" was left between the two U-shaped magnets. For this configuration, longer V-

shaped spacers were used. The same two groups of sensors and a position similar to that used at the previous configuration were considered here. The number of active sensors was varied according to each test. For each point, the results from all active sensors were added and then plotted. No wheels were used.
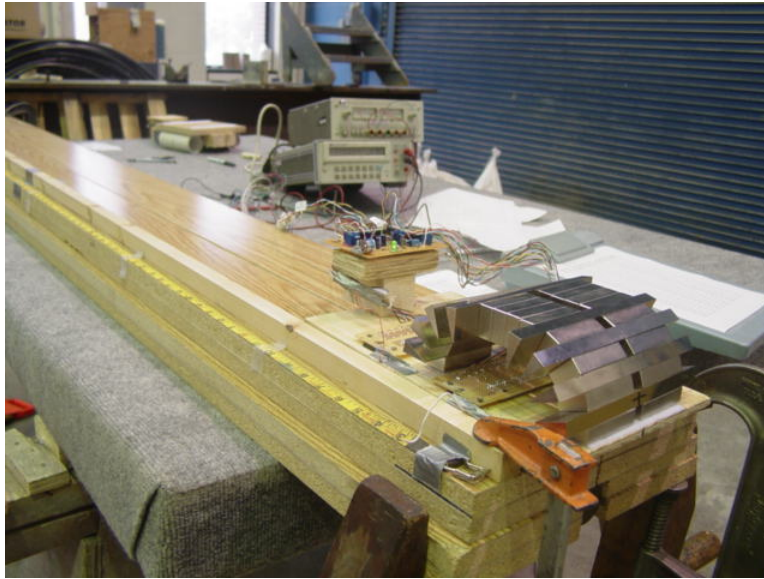
Figure 2-6: Magnet configuration no. 4

2.2.5 Magnet Configuration No. 5

In this configuration, the U-shape magnetic yoke was kept but the grade 35 neodymium magnets were replaced with grade 45 neodymium magnets. Figure 2-7 shows magnet configuration no. 5 (MC5), which consists of seven magnets alternating with V-shaped. The magnetic yoke was placed upside down on a wood board such that the poles of the U-shaped magnet were parallel to the longitudinal axis of the specimen. The spacers were made of a highly permeable, high saturation, magnet iron, which is commonly used in transformers and electromagnets. The size of the magnets was increased where each magnet was 2" x 2" x 1" in size, with a residual flux density of 13300 Gauss. The North and South Poles of each magnet were located on opposite faces, having a 2" x 2" measurement. Similar to previous configurations, two groups of sensors were used here. The same two groups of sensors and a position similar to that used at the previous configuration were considered here. The number of active sensors was varied

according to each test. For each point, the results from all active sensors were added and then plotted. No wheels were used in this configuration.
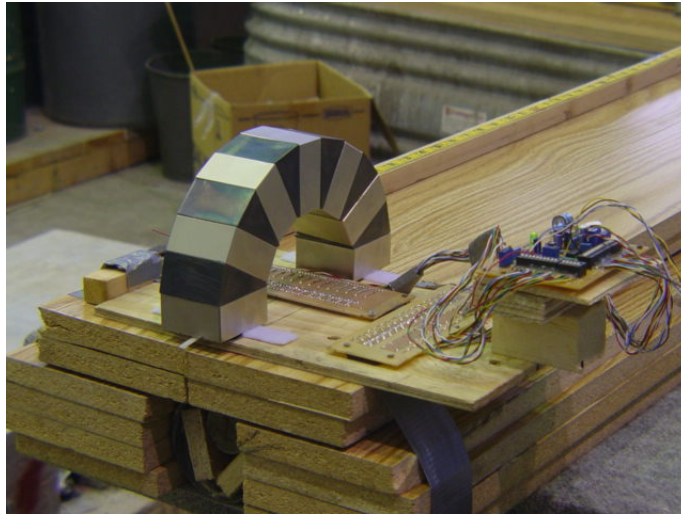
Figure 2-7: Magnet configuration no. 5

2.3   Test Specimens

2.3.1 Plywood Specimens

A typical plywood test specimen is here described. A carpeted wooden table was used to conduct each plywood test. The specimen was placed on the table and secured on both sides with two or three ¾" boards. Additional ¾" boards were then placed over the specimen and clamped or taped to the table. The number of boards placed over the specimen was varied according to each test. Plastic spacers were also used in several tests to provide adequate clearance between the specimen and the boards. The boards were also clamped or taped at one side creating a centerline in the specimen, which was used to align the center of the magnet with the specimen. A tape measure was used to measure the distance along the specimen. A wire was taped to each magnet to provide a point of reference while moving the magnet. Voltage readings were recorded at every 1" interval throughout the length of each specimen. Graphic chart was considered to be the best way of showing the results, where the vertical axis represents voltage and the horizontal axis represents the location of the device. Auxiliary lines were drawn, in some

chart, to identify the location of induced damages. Some plywood specimens were tested using different magnet configurations. A typical setup can be seen in Figure 2-8.

Figure 2-8: Typical plywood specimen test setup

2.3.1.1   Plywood Specimen No. 1

Figure 2-9 shows a drawing of plywood specimen no. 1 (PS1), which identifies the location of induced damages. This specimen included one rebar of 1 ½" diameter with three manmade flaws. The damages were made perpendicular to the length of the bar with differing lengths and depths. The first cut was ¾" in length and 1" in depth and started at 23 ¼" from the beginning of the bar. The second cut was 1/8" in length and ¾" in depth and started at 47 ¾" from the beginning of the bar. The third cut was ¼" in length and 1" in depth and started at 79 ¾" from the beginning of the bar. The third cut was also rotated 90 degrees with respect to the first two cuts. This specimen was used for the majority of the plywood tests and was tested with most of the magnet configurations.
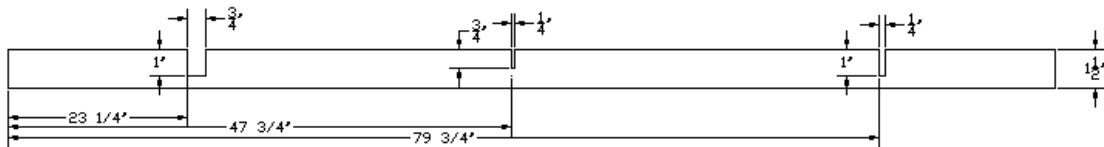
Figure 2-9: Plywood specimen no. 1

2.3.1.2   Plywood Specimen No. 2

Figure 2-10 shows plywood specimen no. 2 (PS2), which includes three 1 ½" diameter bars with different lengths. The two shorter bars, measuring 29" and 32" in length, respectively, were placed beside the same bar described in plywood specimen no. 1. The cuts in the shorter bars were made in the center of each and were perpendicular to the length of the bar, measuring ¾" in length and 1" in depth. The cuts in the shorter bars were then lined up with the cut in the longer bar at 23 ¼", measured from the beginning of the bar. This specimen was tested with magnet configuration no. 3.

Figure 2-10: Plywood specimen no. 2

2.3.1.3   Plywood Specimen No. 3

Plywood specimen no. 3 (PS3) consisted of two 1 ½" diameter bars with no damage. The bars were positioned such that a gap was left from 46" to 50" along the specimen. This specimen was tested with magnet configuration no. 3.

2.3.1.4   Plywood Specimen No. 4

Figure 2-11 shows plywood specimen no. 4 (PS4). This test considers the same bar described in PC1, now placed inside a 3" diameter corrugated metal duct. The bar was elevated to the top of the duct using plastic spacers. Four boards were placed on each side and spacers were added to provide clearance over the specimen. This specimen was tested with magnet configuration no. 3 and magnet configuration no. 5. The duct alone was tested only with magnet configuration no. 5.

Figure 2-11: Plywood specimen no. 4

2.3.1.5　　Plywood Specimen No. 5

Plywood specimen no. 5 (PS5) consists of two 1 ½" diameter bars with no damage. The bars were placed at the bottom of the corrugated duct. Similar to PS3, a gap of 4", located at 46" to 50", was left. This specimen was tested with magnet configuration no. 5.

2.3.1.6　　Plywood Specimen No. 6

Plywood specimen no. 6 (PS6) includes a bar of 1 ½" diameter placed at the bottom of the duct. A ¾" deep cut in the bar was made from 46 ½" to 49 ½". This specimen was tested with magnet configuration no. 5.

2.3.1.7　　Plywood Specimen No. 7

Figure 2-12 shows one of the strand arrangements considered in plywood specimen no. 7 (PS7). For this setup, several ½" diameter strands with 6' length were used. A 4" gap was left between some strands while others remained continuous. Four different arrangements were considered. The total number of strands was held constant and equal to 13, while the number of continuous varieties assumed the quantities 1, 4, 7 and 10 strands. The bundle of strands were secured with tape and later placed at the bottom of the corrugated duct. This specimen was tested with magnet configuration no. 5.

Figure 2-12: Plywood specimen no.7. Left: 4" gap. Right: strand arrangement

Test results considering plywood specimens do not truly represent a real situation where the bar would be embedded within concrete. To better comprehend whether or not there is any difference between the results, a decision was made to carry out tests considering concrete specimens. Therefore, further conclusions between the results obtained in both concrete and plywood specimens could be drawn.

2.3.2 Concrete Specimens

Three concrete specimens were considered for this study. Each specimen measured 72" long, 6" wide and 8" deep. A 1 ½" diameter bar, with a ¾" deep cut in the center, was placed into each beam. The only difference between each concrete specimen was the location of the 1 ½" diameter bar. Concrete specimens no. 1 (CS1), 2 (CS2) and 3 (CS3) had the bar located at 2 ¾", 4 ¾" and 7", respectively, measured from the top surface of the concrete beam. Figure 2-13 (right) shows all three specimens before pouring the concrete. An X-shaped reinforcement was made using 3/8" diameter bars and was placed at 12" and 60" of each beam. Transverse rebars, of the same diameter, were placed under one of those X-shaped reinforcements. The transverse bars were located at 6", 12" and 18". Figure 2-13 (left) shows the X-shaped reinforcement with transverse bars.

All three concrete specimens were tested with magnet configuration no. 1 and concrete specimens no. 1 and 2 were tested with magnet configuration no. 4.

Figure 2-13: Concrete specimens. Left: X-shaped reinforcement. Right: formwork and rebars

2.4 Test Procedures and Results – Plywood Specimens

2.4.1 Magnet Configuration No. 1 & Plywood Specimen No. 1

2.4.1.1 Magnet Configuration No. 1 with Nine Magnets

PS1 was tested using MC1 with nine magnets. As previously mentioned, PS1 had three manmade flaws located at 23 ¼", 47 ¾" and 79 ¾" (see Figure 2-2). The number of boards over the specimen varied from one through five plywoods. Figure A.1 through Figure A.10, in Appendix A, show test setup and results for all five tests carried out.

Figure 2-14 compares the results from all five tests conducted using MC1 with nine magnets. It can be noted that:

- The measured magnetic field is disturbed at the exact locations of the damages. Even though the third flaw was rotated, the MFL device was capable of detecting its location.

- The signal's strength is directly proportional to how much damage is present in the bar. For a greater amount of section loss, a higher disturbance in the measured magnetic field is expected.

- The signal's strength is inversely proportional to how far the sensors are from the bar. If the sensors are closer to the ferromagnetic material, the signal's strength is expected to be higher.
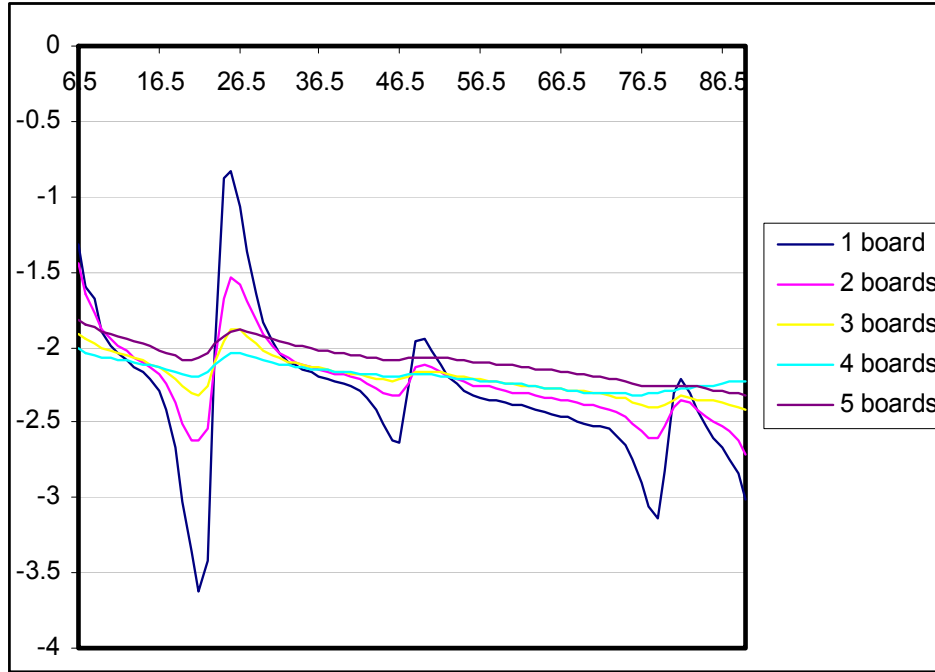
Figure 2-14: Data comparison for PC1 tested using MC1 with nine magnets

2.4.1.2   Magnet Configuration No. 1 with Seven Magnets

PS1 was tested using MC1 with seven magnets. The number of boards over the specimen varied from one to five through five plywood tests. Figure A.11 through Figure A.20, in Appendix A, show test setup and results for all tests carried out.

Figure 2-15 compares results of all tests conducted using MC1 with seven magnets. The results follow the same trend observed in previous testing.
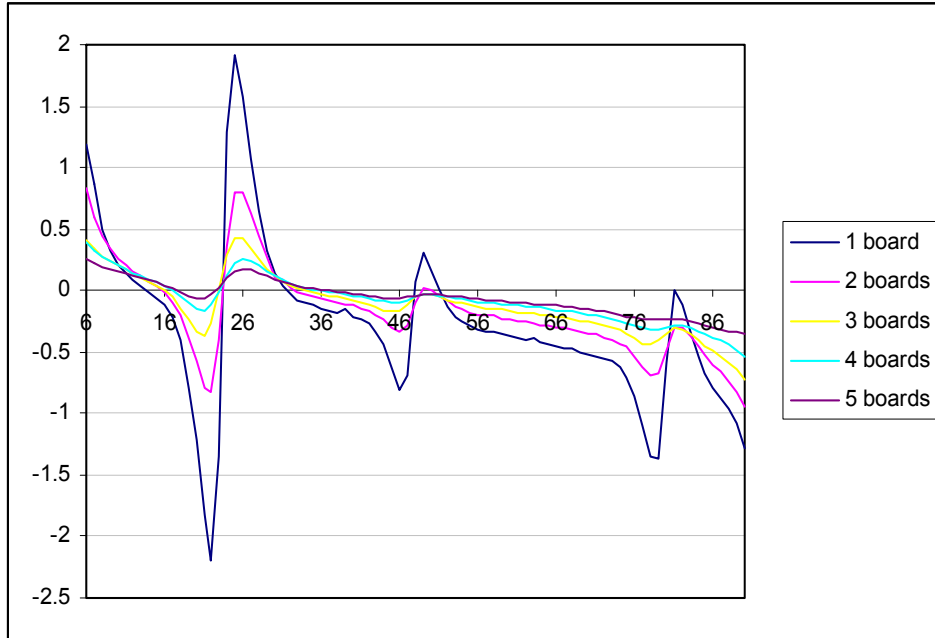
Figure 2-15: Data comparison for PC1 tested using MC1 with seven magnets

2.4.1.3   Magnet Configuration No. 1 with Five Magnets

PS1 was tested using MC1 with five magnets and two boards separating the specimen from the magnetic source. The results follow the same trend observed in previous testing. Figure A.21 and Figure A.22, in Appendix A, show test setup and results for the test conducted.

2.4.1.4   Magnet Configuration No. 1 with Three Magnets

PS1 was tested using MC1 with three magnets and two boards separating the specimen from the magnetic source. The results follow the same trend observed in previous testing. Figure A.23 and Figure A.24, in Appendix A, show test setup and results for the test conducted.

The influence of magnetic density can be observed in Figure 2-16. The plot compares the results from all four tests, which consider MC1 with differing numbers of magnets and with two boards separating the specimen from the magnetic source. It can be seen that the measured magnetic flux is directly proportional to the strength of the

magnetic source. Therefore, a greater disturbance in the signal will occur if a greater magnetic density is used to conduct the test.
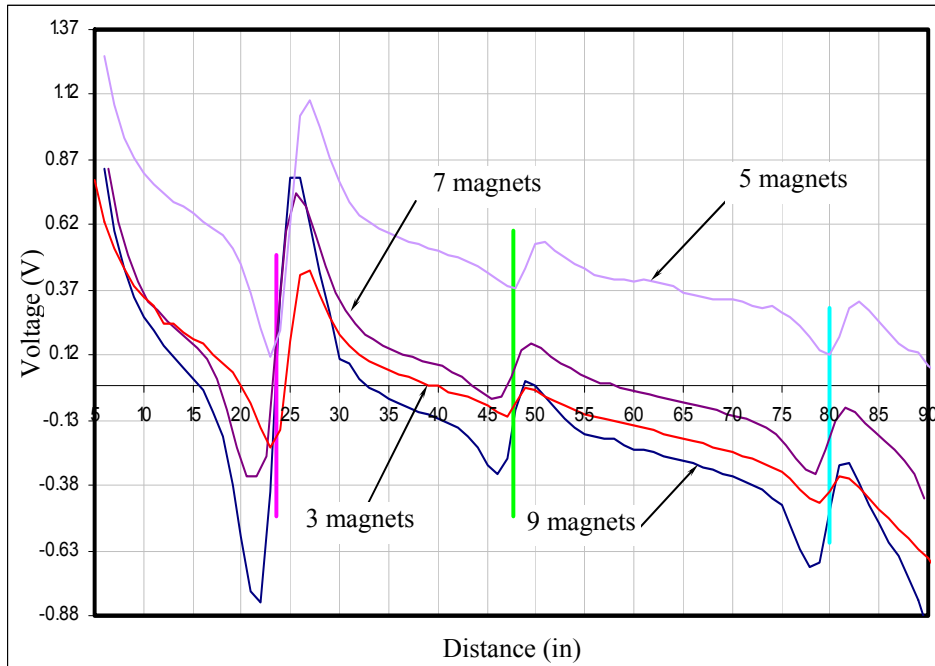
Figure 2-16: Data comparison for PC1 tested using MC1 with 3, 5, 7 and 9 magnets

2.4.2 Magnet Configuration No. 2 & Plywood Specimen No. 1

Plywood specimen no. 1 was tested using magnet configuration no. 2, previously shown in Figure 2-3. Only one board was used to separate the specimen from the magnet source. For this configuration, it was already expected some unusual results because of the peculiar location of the sensor with respect to the magnetic source. In addition, Hall-effect sensor measures the voltage difference between two parallel crystal faces, which is caused by the magnetic field flowing perpendicular to these faces. Figure 2-17 shows the test results carried out at plywood specimen no.1 (PS1) using magnetic configuration no.2 (MC2). No peak-and-valley disturbance is observed in the results. Also, the flaws located at 79" did not cause any disturbance; therefore, the damage could not be detected by analyzing the signal. Those results totally differ from previous testing observations. Based on that, a decision was made to disconsider the used of MC2 for further testing.
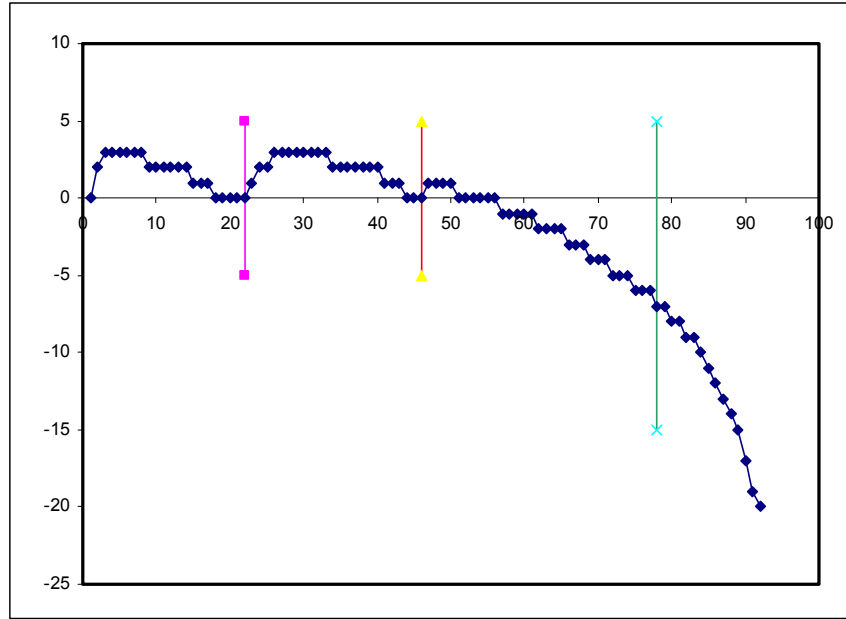
Figure 2-17: Results of PC1 tested using MC2

2.4.3 Magnet Configuration No. 3 & Plywood Specimens

2.4.3.1 Plywood Specimen No. 1

PS1 was tested using the MC3, previously shown in Figure 2-4. Two boards were used to separate the specimen from the magnetic source. Table 2-1 shows the sensor activations where a certain number of active sensors were considered and the results from each measured point are added and lately plotted in charts. Figure A.25 through Figure A.28, in Appendix A, show test setup and results.

Test results considering two different sensor activations are shown in Figure 2-18. It can be seen that signal strength is directly proportional to the number of active sensors. Consequently, a higher signal disturbance is expected at the location of the damage if a greater number of active sensors are considered.

Table 2-1: Sensor activation considered in PS1 tested using MC3

Sensor Activations	Sensor Group A	Sensor Group B
SA#1	6-10 ON	ALL OFF
SA#2	ALL ON	ALL OFF
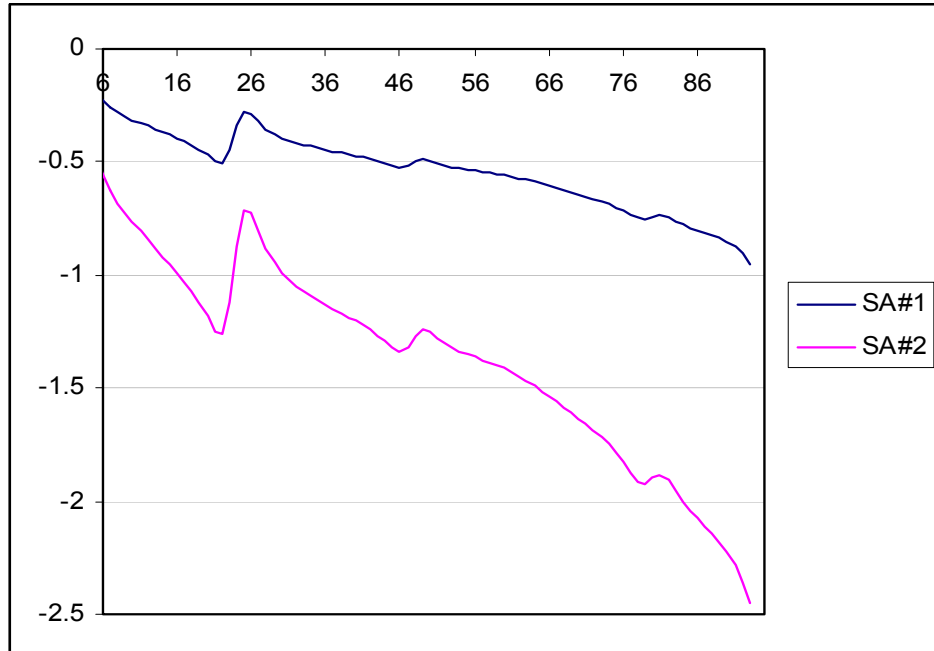
Figure 2-18: Data comparison for PC1 tested using MC3 and two different sensor activations

2.4.3.2   Plywood Specimen No. 2

PS2 was tested using MC3 and only one board to separate the specimen from the magnetic source. The sensor activation considered was ALL sensors ON from group B and ALL OFF from group A. Figure A.29 through Figure A.32, in Appendix A, show test setup and results.

The results plotted in Figure 2-19 show that the disturbance caused by additional rebars alters the magnetic field differently form the disturbance caused by the damage.

2
1.5
1
0.5
0
-0.5

3   8   13   18   23   28   33   38   43   48   53   58

start of the first rebar

start of the second rebar

damage in all 3 rebar

end of 2 short rebar

damage in the middle
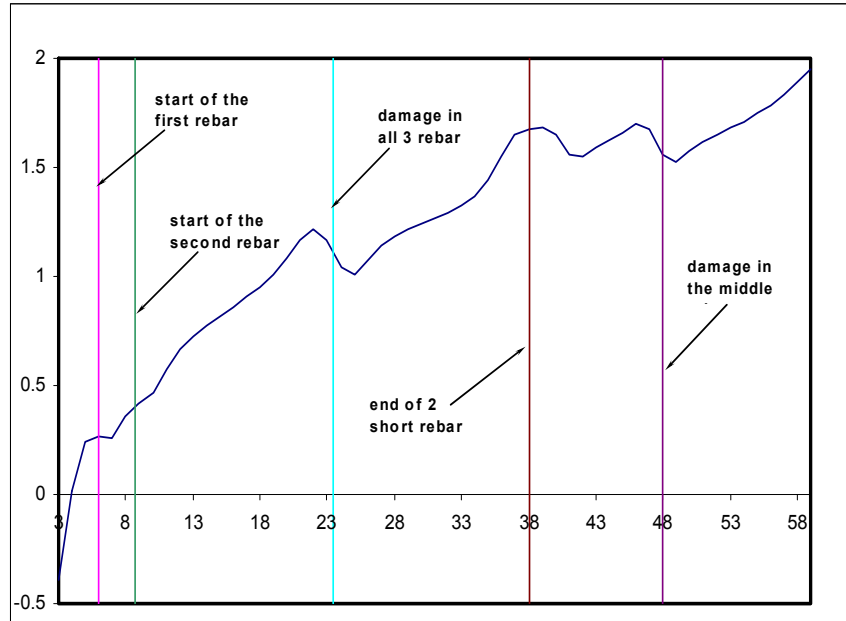
Figure 2-19: Results for PC2 tested using MC3

2.4.3.3   Plywood Specimen No. 3

PS3 was tested using MC3. One board was placed over the specimen separating the magnetic source from the bar. The active sensors considered were sensors 6-10 ON from group B and ALL OFF from group A.

The results plotted in Figure 2-20 show the boundary effect caused here by the gap which separates the two rebars. Because of the discontinuity, a new North and South Pole are created, respectively, at the end of the first rebar and at the beginning of the second rebar.
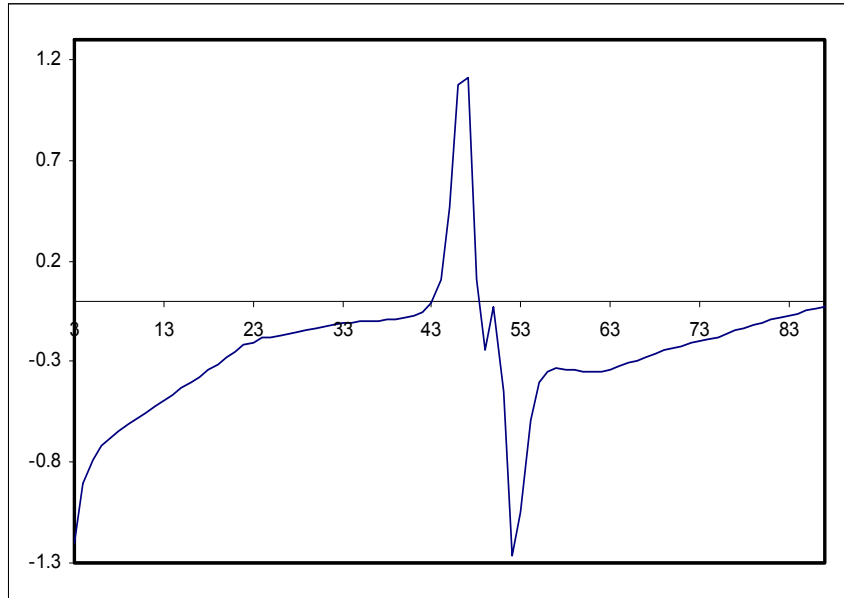
Figure 2-20: Results for PC3 tested using MC3

2.4.3.4   Plywood Specimen No. 4

PS4 was tested using MC3. One board was used to separate the magnetic source from the duct. The sensor activation considered was sensor 6-10 ON from group B and ALL OFF from group A. Figure A.33 and Figure A.34, in Appendix A, show test setup and results.

2.4.4 Magnet Configuration No. 4 & Plywood Specimens

2.4.4.1   Plywood Specimen No. 1

PS1 was tested using MC4, previously shown in Figure 2-6. Two boards were placed over the specimen.   Table 2-2 shows the sensor activations where a certain number of active sensors were considered and the results from each measured point are added and lately plotted in charts. Figure A.35 through Figure A.41, in Appendix A, show setup and results for each test.

Figure 2-21 compares the results of all four tests. It can be noted that the results obtained from the sensors located between the magnet poles had a more distinct signal. The peak-and-valley disturbance can be easily observed at those results.

Table 2-2: Sensor activation considered in PS1 tested using MC4

Sensor Activations	Sensor Group A	Sensor Group B
SA#1	6-10 ON	ALL OFF
SA#2	ALL ON	ALL OFF
SA#3	ALL OFF	6-10 ON
SA#4	ALL OFF	ALL ON
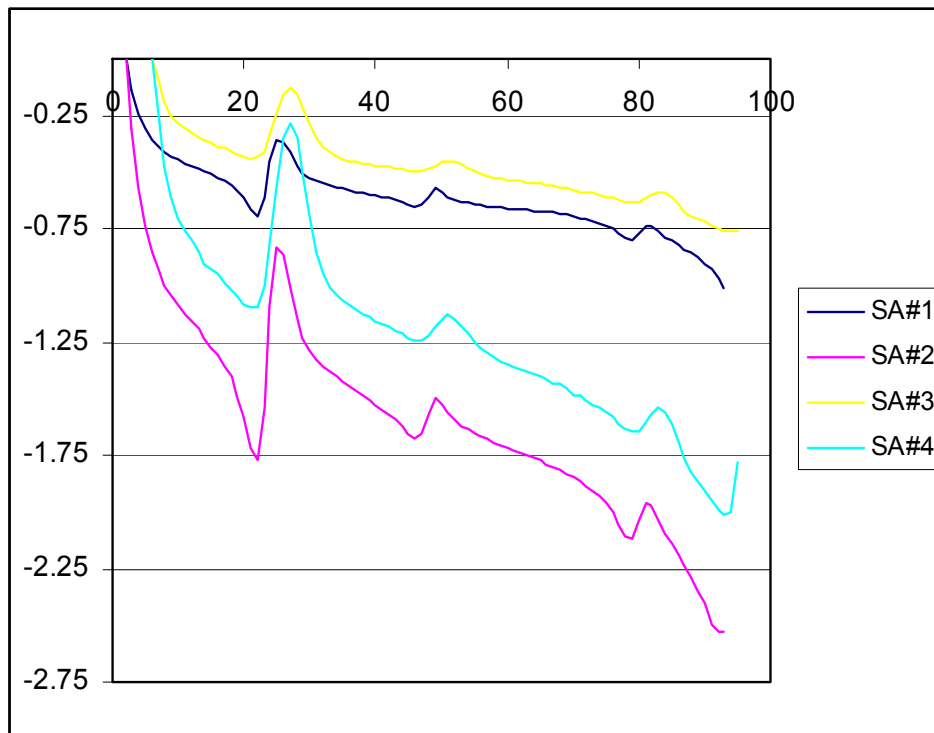
Figure 2-21: Data comparison for PC1 tested using MC4 and four different sensor activations

Figure 2-22 shows the data comparison for PS1 tested using MC1 with seven magnets, MC3 and MC4. It can be seen that the results are identical, even though different magnet configurations were used. MC1 had higher signal disturbance, followed by MC3 and then by MC4.
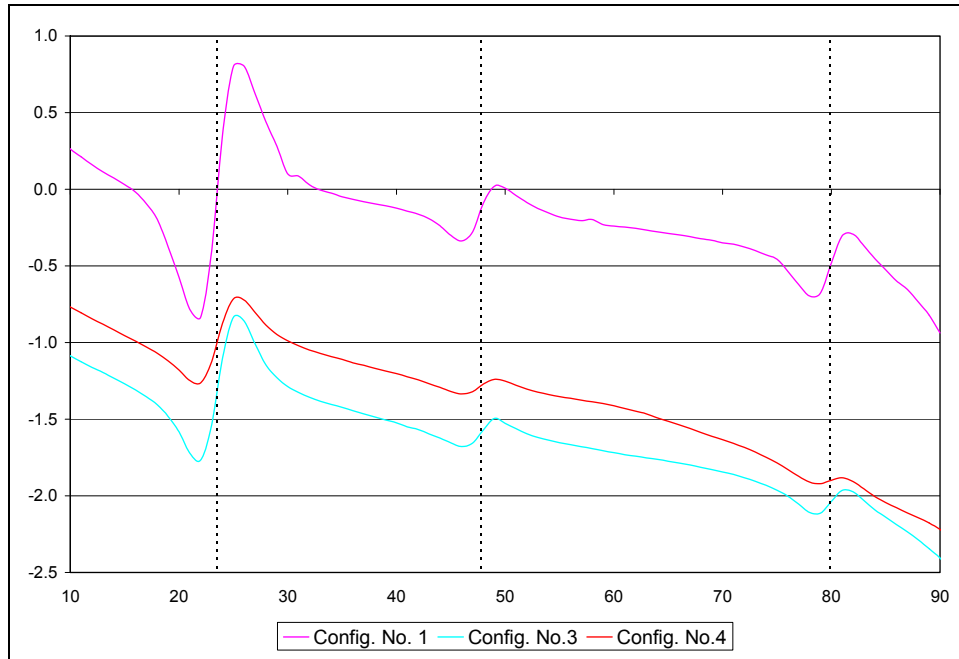
Figure 2-22: Data comparison for PC1 tested using MC1 with 7 magnets, MC3 and MC4

2.4.5 Magnet Configuration No. 5 & Plywood Specimens

2.4.5.1 Plywood Specimen No. 4

PS4 was tested using MC5, previously shown in Figure 2-7. Two boards were placed over the specimen. Figure A.42 through Figure A.47, in Appendix A, show test setup and results of the four tests.

Table 2-3 shows the sensor activations where a specific number of active sensors were considered. Their results are then added and plotted in chart form. Figure 2-23 shows the results of all four tests considered. It can be noted that for a greater number of active sensors, the signal's disturbance is also greater. SA#3 had the highest disturbance, followed by SA#4 and SA#2, and finally by SA#1.

Table 2-3: Sensor activation considered in PS4 tested using MC5

Sensor Activations	Sensor Group A	Sensor Group B
SA#1	6-10 ON	ALL OFF
SA#2	4-12 ON	ALL OFF
SA#3	ALL ON	ALL OFF
SA#4	1-5 & 11-15 ON, 6-10 OFF	ALL OFF
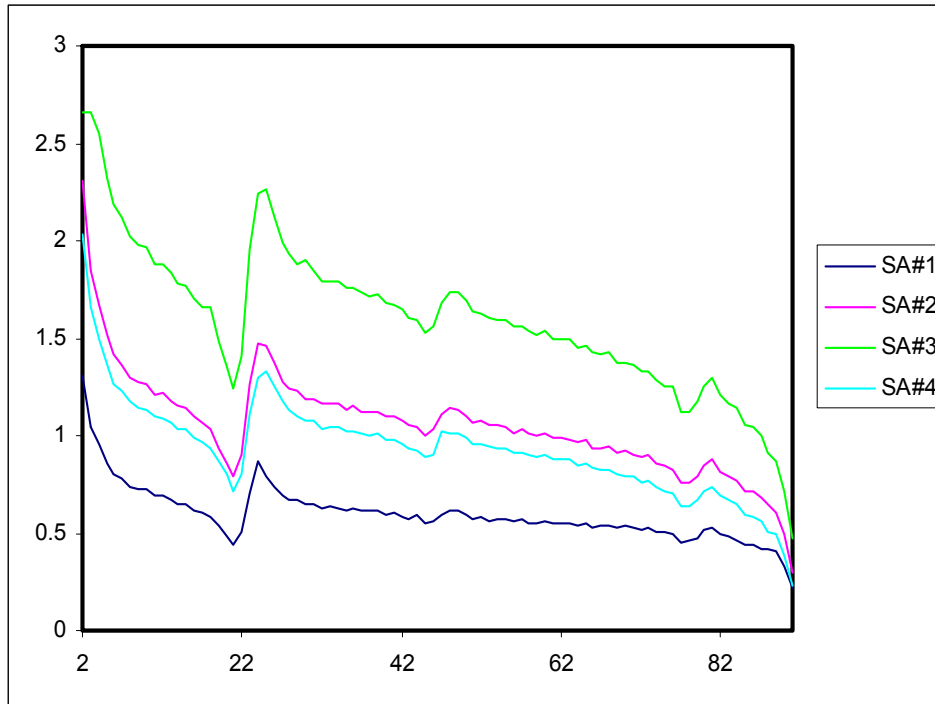
Figure 2-23: Data comparison for PC4 tested using MC5 and four different sensor activations

2.4.5.2   Plywood Specimen No. 5

PS5 was tested using MC5. Two boards were placed over the specimen to separate the sensor from the duct. The active sensors considered were sensors 6-10 ON from group B and ALL OFF from group A. Figure A.48 and Figure A.49, in Appendix A, shows test setup and results.

2.4.5.3   Plywood Specimen No. 6

PS6 was tested using MC5. Two boards were placed over the specimen to separate the sensor from the duct. The active sensors considered were sensors 6-10 ON from group B and ALL OFF from group A. Also, the duct without any bar inside was tested using MC5. Figure A.50 and Figure A.51, in Appendix A, show test setup and results.

Figure 2-24 shows the results from PS5, PS6 and duct only testing using MC5. It can be seen that results which consider only the duct had a very steady response since either no discontinuity or corrosion is present. Also, the results from PS5 (4" gap) and PS6 (3" cut) show that the signal disturbance is directly proportional to the amount of section loss. As a result, higher signal disturbance is expected if the amount of section loss is also greater.
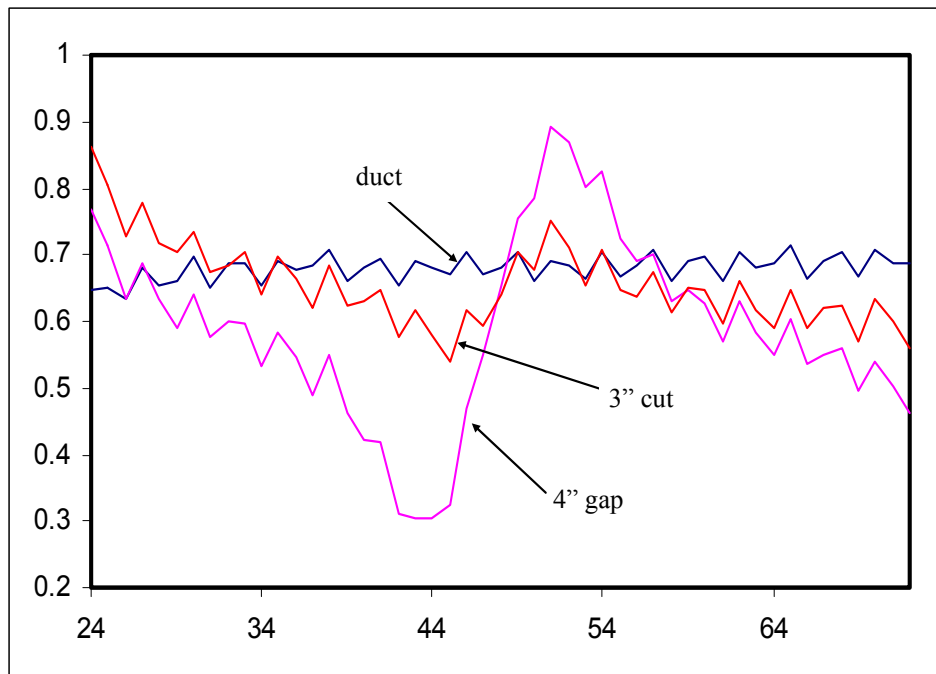
Figure 2-24: Data comparison for PS5, PS6 and duct alone tested using MC5

2.4.5.4   Plywood Specimen No. 7

PS7 was tested using MC5. Two boards were placed over the specimen to separate the duct from the sensors. Four different tests were carried out based on four different strand configurations. The first test considered one continuous and twelve non-continuous, which is equivalent to 76% of section loss. The second test considered four continuous and eight non-continuous, representing a loss of 53%. The third test had a loss of 30%, considering seven continuous and six non-continuous.   The fourth test simulates a loss of seven percent by considering ten continuous and three non-continuous strands.   In addition, the duct without any strands inside was also investigated using MC5. The active sensors considered were sensors 6-10 ON from group B and ALL OFF from group A. Figure A.52 through Figure A.55, in Appendix A, show results for all four tests, separately.

Figure 2-25 compares the results from all five tests which include four different strand configurations and duct alone. Similar conclusions to previous tests are here observed. As previously concluded, the signal's disturbance is directly proportional to the amount of section loss here simulated by discontinuous strands.   The highest disturbance occurred in the test which had the greatest amount of section loss (76%), followed by four continuous and eight non-continuous, and then by seven continuous and six non-continuous representing 30%, and finally by 10 continuous and three non-continuous strands representing seven percent of section loss. There is no visible peak-and-valley disturbance in the test results that simulate a loss of seven percent. This can be explained by the masking effect caused by the duct.
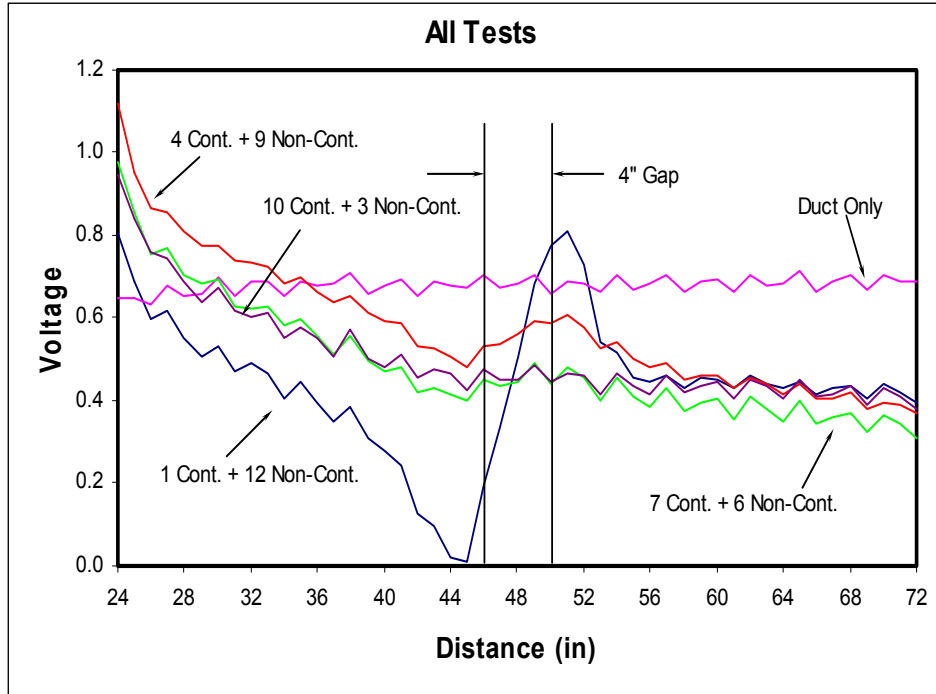
Figure 2-25: Data comparison for PC7 with four strand configurations and duct alone tested using MC5

2.5 Test Procedures and Results – Concrete Specimens

2.5.1 Magnet Configuration No. 1

2.5.1.1 Concrete Specimen No. 1

CS1 was tested using MC1. Figure A.56 and Figure A.57, in Appendix A, show test setup and results.

2.5.1.2 Concrete Specimen No. 2

CS2 was tested using MC1. Figure A.58 and Figure A.59, in Appendix A, show test setup and results.

2.5.1.3 Concrete Specimen No. 3

CS3 was tested using MC1. Figure A.60 and Figure A.61, in Appendix A, show test setup and results.

Figure 2-26 shows results for three concrete specimens tested using MC1 with seven magnets. It can be seen that if the bar is located far away from the sensor (e.g. CS3), the signal's disturbance is decreased.
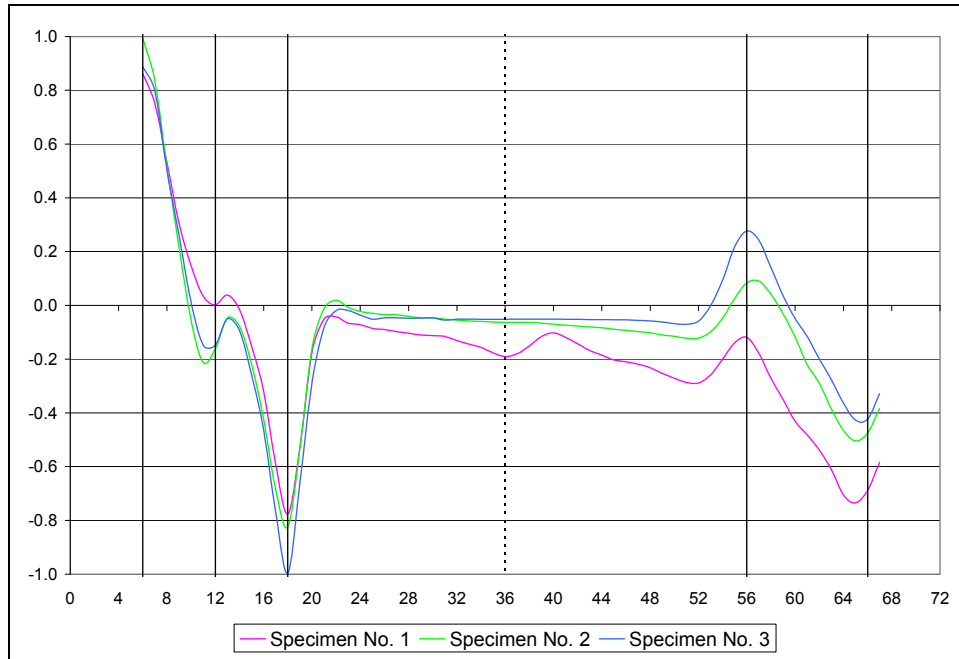
Figure 2-26: Data comparison for CS1, CS2 and CS3 tested using MC1

2.5.2 Magnet Configuration No. 4

2.5.2.1 Concrete Specimen No. 1

CS1 was tested using MC4. The sensor activation considered was sensors 4-12 ON from group B and ALL OFF from group A. Figure A.62 and Figure A.63, in Appendix A, show test setup and results.

2.5.2.2 Concrete Specimen No. 2

CS2 was tested using MC4. The sensor activation considered was sensors 4-12 ON from group B and ALL OFF from group A. Figure A.64 and Figure A.65, in Appendix A, show test setup and results.

2.5.3 Magnet Configuration No. 5

2.5.3.1   Concrete Specimen No. 2

CS2 was tested using MC5. The sensor activation considered was ALL sensors ON from group B and ALL OFF from group A. Figure A.66, in Appendix A, shows the results.

Figure 2-27 shows results for concrete specimen no. 2 tested using MC1 with seven magnets, MC4 and MC5. It can be seen that the signal disturbance obtained using MC5 is more perceptive than that from MC1 and MC4.
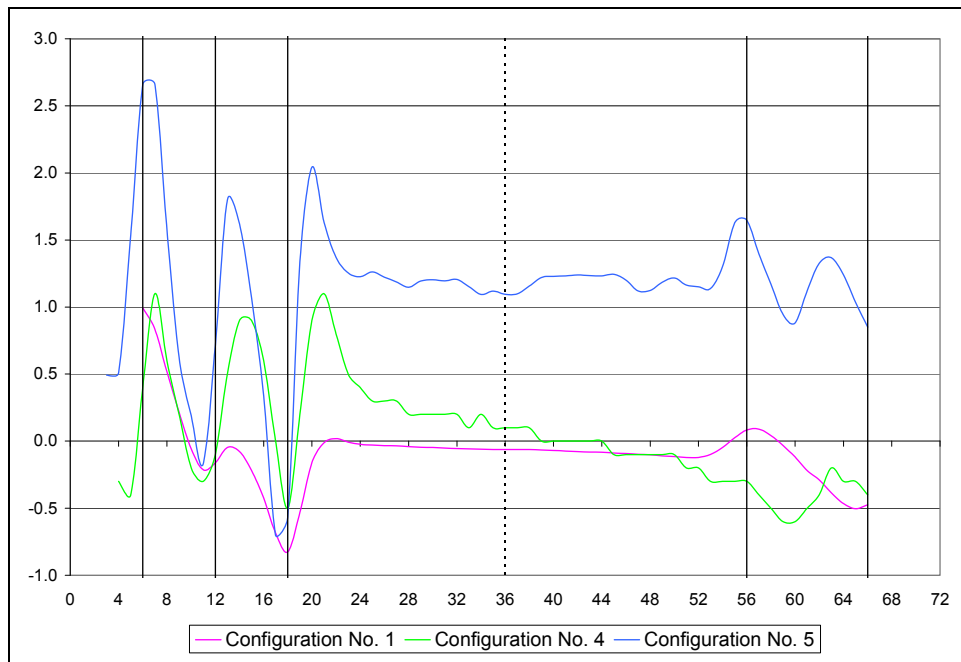
Figure 2-27: Data comparison for CS2 tested using MC1 with seven magnets, MC4 and MC5

2.6   Conclusions

A series of tests has been carried out to optimize the magnet shape to be used in the MFL device.   Five magnet configurations were here evaluated.   For each configuration, different residual magnetic density was used. Also, Hall-effect sensors in different quantities and arrangements were assumed in order to determine the best system to measure the magnetic field.

It can be concluded that the U-shaped magnet provided the best results. Figure 2-7 shows magnetic configuration no. 5 -- the best magnetic configuration -- which consists of seven grade 45 neodymium magnets with a residual flux density of 13300 Gauss each, stacked between six V-shaped magnetic iron. This configuration was also used in further testing conducted in this research. It was observed, in some tests, that the quantity of magnets can influence the measured signal. As a result, use of magnets with the highest residual magnetic density is recommended.

No difference in results was observed in tests which considered concrete or the absence of concrete. Therefore, concrete's magnetic permeability can be neglected. In other words, test results observed in concrete specimens had the same behavior as tests that considered plywood.

Before proceeding with further development and testing, a decision was made to carry out numerical simulations by using a finite element method to study the parameters that may affect magnetic flux in ferromagnetic materials. The next chapter provides a summary of these efforts.

Chapter 3

Finite Element Modeling of Magnet and Damaged Rebar

Before proceeding with further development of the non-destructive device, a decision was made to carry out numerical analysis to better comprehend the parameters that may affect the use of MFL methodology to detect corrosion in embedded steel elements in concrete. Several magnet configurations, different material properties and steel rebar with different corrosion profiles (notch, circumferential and squared damage) are some of the variables here investigated. Commercial finite element software ANSYS® was the program employed to carry out those analyses. This chapter provides a summary of these efforts.

3.1 Introduction

Finite element (FE) models were created to better comprehend the magnetic field behavior when applied to ferromagnetic material. Initially, three preliminary FE models were built to investigate and understand the magnetic field flow though the rebar. The first model also called basic model only considers two magnets and a non-damaged rebar. In the second model, the rebar was replaced by a notched rebar and at the last model from this series, additional magnets were added and the notched rebar was kept in the model. Comparisons between the results from those three models are here presented and discussed. An additional FE model was built to determine the influence of the measured magnetic field versus the number of magnets. Based on the results of those four preliminaries FE models, decision was made to create more realistic models to simulate equivalent results to those obtained during the experiments. Prior to create the model, it was necessary validate the FE model with experimental results so that more reliable conclusions based on the results could be drawn. Lately after validation, the FE model was used to conduct an extensive parametric study to better comprehend the interaction

between the variables considered in the model. The last model presented in this chapter, simulate the best magnetic configuration previously determined in chapter 2. At this point, similar results -- peak-and-valley disturbance in the measured magnetic field -- could be observed in the latest FE model results. Conclusion and recommendations are here presented.

3.2   FE Analysis of Magnetic Field

3.2.1 Basic Model

The basic model consists of two cubic magnets and a cylindrical steel rebar as shown in Figure 3-1. It is known fact that the steel presents the path of least resistance due to high magnetic permeability of steel compared to the surrounding air or concrete. Consequently, the magnetic permeability of concrete can be neglected. As a result, a material with identical magnetic permeability of air was chosen to be modeled between the cylindrical steel rebar and the two cubic magnets.

The dimension of elements and distances between them are illustrated in Figure 3-1. Sintered neodymium-iron-boron (Nd-Fe-B) magnets were used as permanent magnets. The second quadrant demagnetization curves for this material are shown in Figure 3-2. The material properties used for finite element analysis were obtained based on the linear part of the ND 36 curve. The coercive force is derived as follows:

$$H_C = 900 \times 10^3 \, A/m$$

Remnant field is taken as

$$B_r = 1.22T$$

The relative permeability of the magnet is then calculated as follows.

$$\mu_r = \frac{B_r}{\mu_0 H_c} = \frac{1.22}{4\pi \times 10^{-7}(900000)} = 1.07 H/m$$

The magnetic permeability of air and steel assumed in the models were equal to $1.0\text{x}10^{-6}$ and 1.0, respectively.
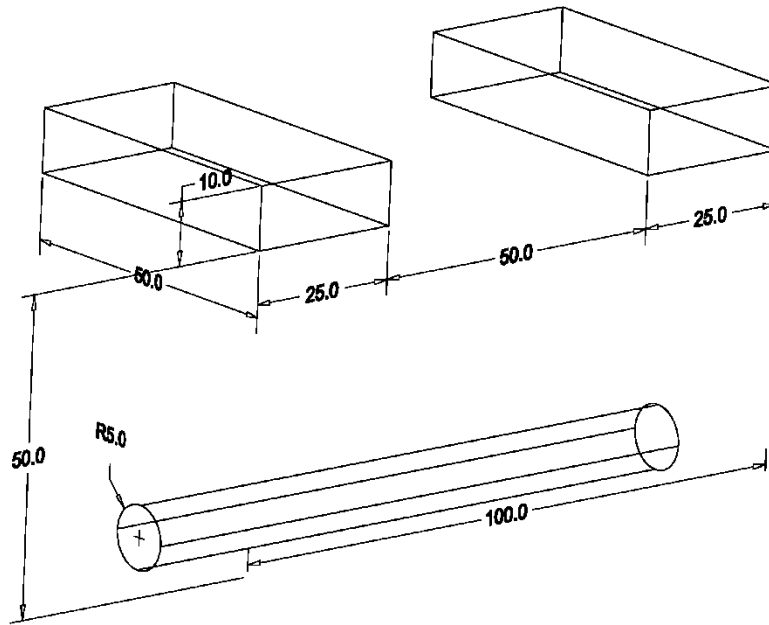
Figure 3-1: Dimensions of models in millimeters
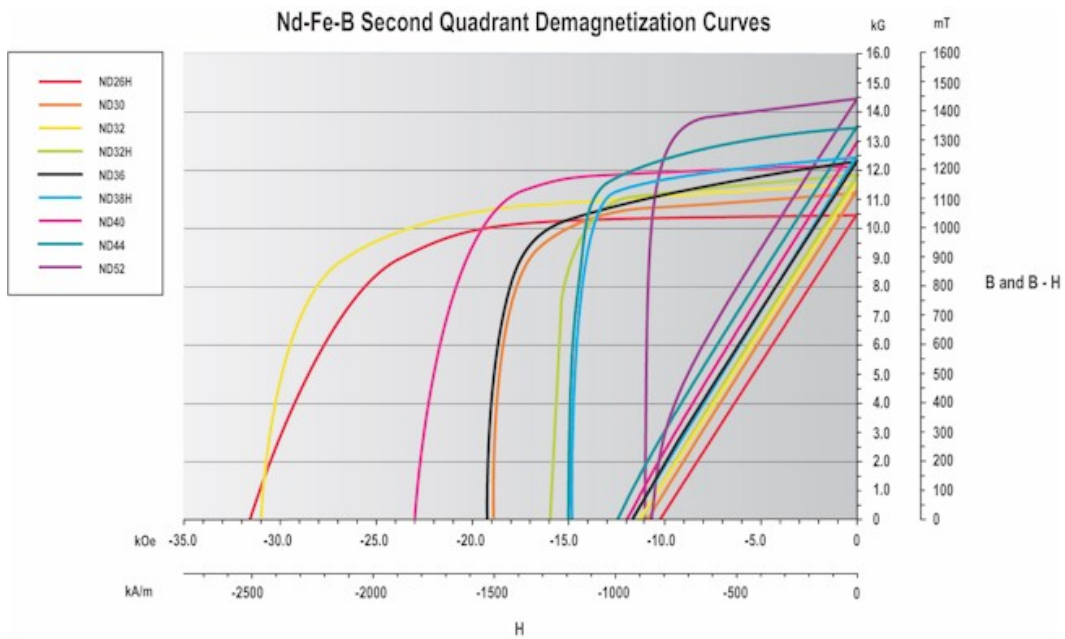
Figure 3-2: B-H curve for permanent magnet

3.2.2 FE Analysis of Non-Damaged Rebar

The model and results are shown in Figure 3-3 through Figure 3-6. The commercial FE software used was ANSYS 5.7. The material properties previously described were considered in the FE model. The MKS units are used throughout this study. Solid98, which is a tetrahedral coupled-field element, was used in the FE analysis. A flux-normal boundary condition equal to zero is applied at the top surface of both magnets (see Figure 3-3) since at the plane of symmetry, the magnet flux lines are orthogonal. The flux-parallel boundary condition holds on all other surfaces. The reduced scalar potential (RSP) strategy was selected, since no current sources are defined in the model. No damage in the rebar was modeled; therefore, no leakage is expected to be observed since all flux will flow along the rebar. Figure 3-3 shows the meshing obtained using the smart meshing algorithm available in ANSYS. As shown, material number 1 represents the air, number 2 represents the steel rebar and numbers 3 and 4 represent permanent magnets.

The result of the analysis indicates that the maximum magnetic flux density (B) is at the middle of the rebar and is equal to 1.9 T, as shown in Figure 3-4.
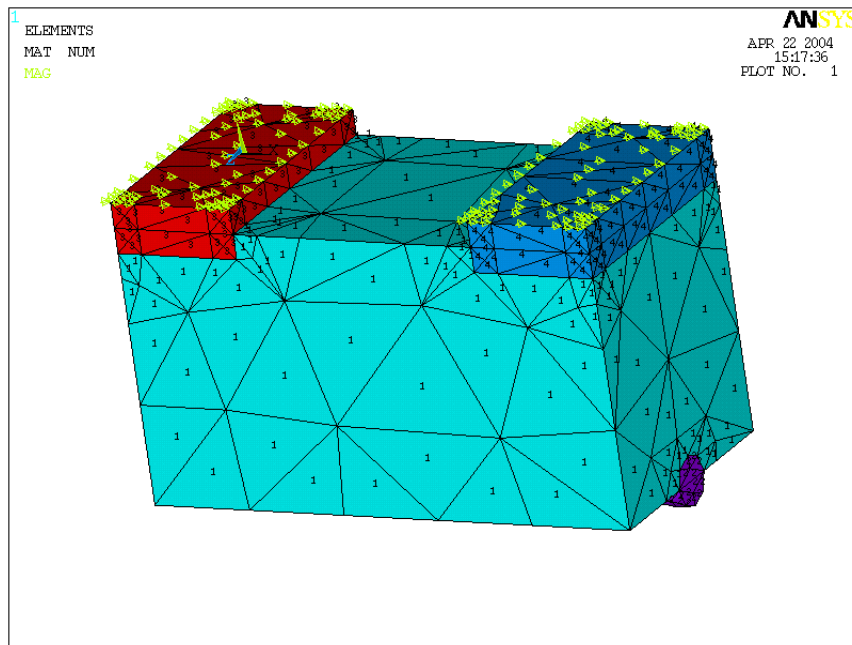
Figure 3-3: FE mesh, boundary conditions and materials for the first analysis
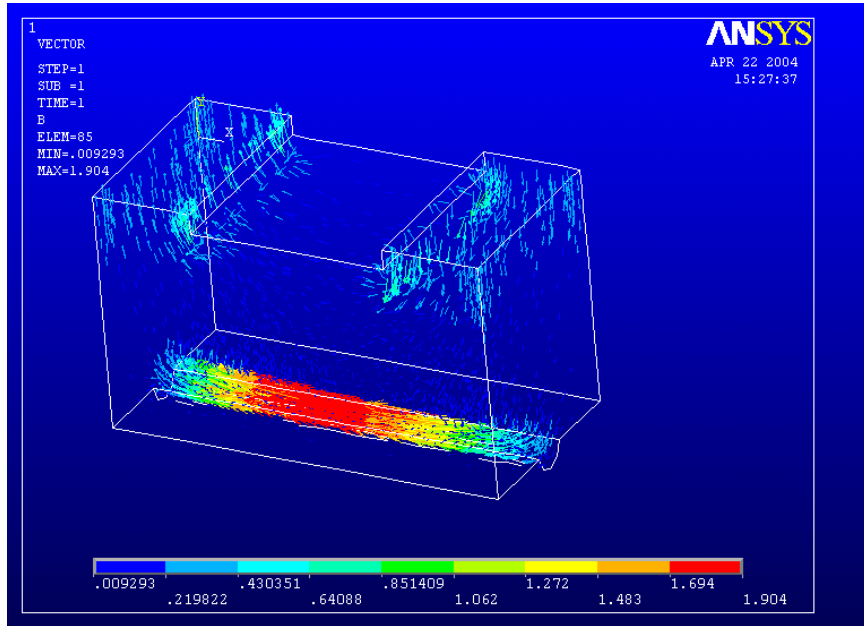
Figure 3-4: Magnetic flux density (B)
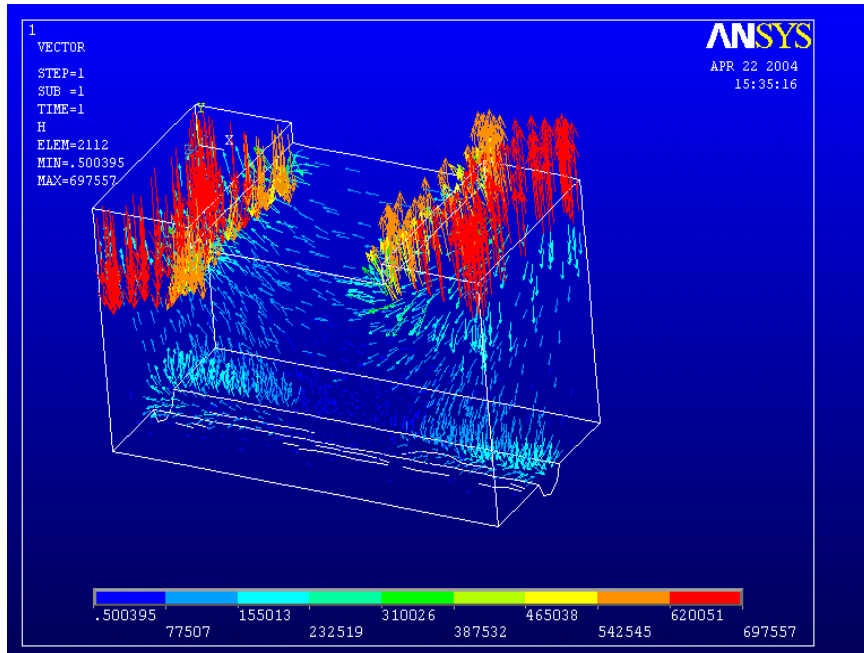
Figure 3-5: Magnetic flux intensity (H)
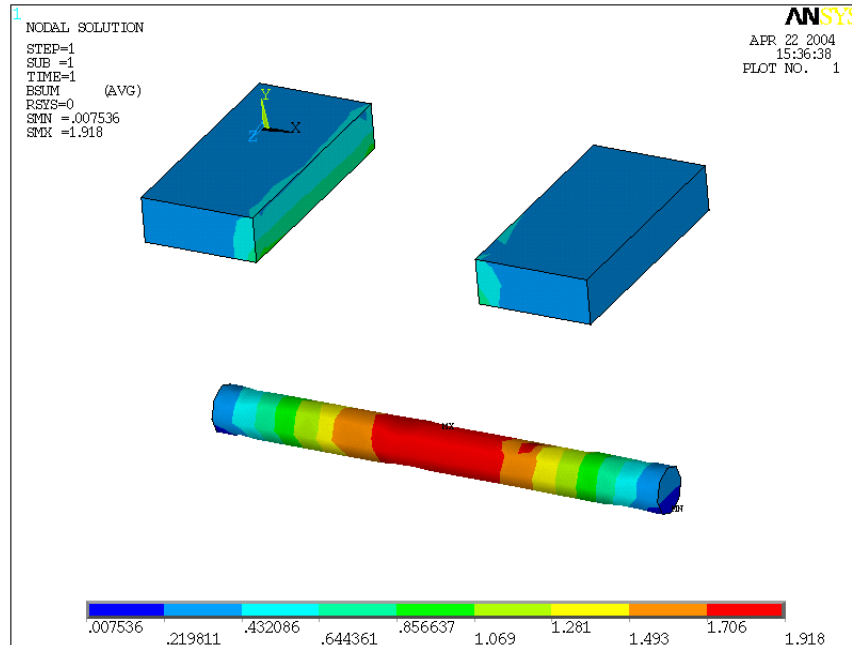
Figure 3-6: Sum of magnetic flux density (B)

3.2.3 FE Analysis of a Notched Rebar

Figure 3-7 shows the second FE model considered. A small notch with 2.5 mm depth and 5 mm width was created in the middle of the steel rebar to simulate a corroded region. The material properties, geometry and boundary conditions were the same as those assumed in the previous model.

As shown in Figure 3-8, the magnetic flux density vector is distorted around the notch. The maximum value of the magnetic field (B) is 3.1 T, which is different from the results obtained in the first model, which was 1.9 T. Figure 3-9 shows the magnetic flux intensity (H) results which follow the same trend observed in Figure 3-5.
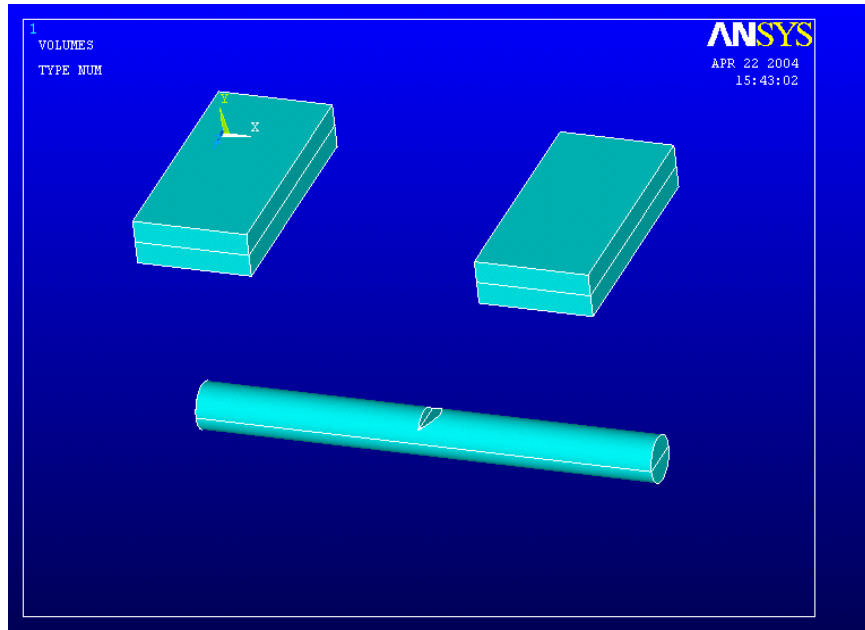
Figure 3-7: FE model that includes a notched rebar considered for the second analysis
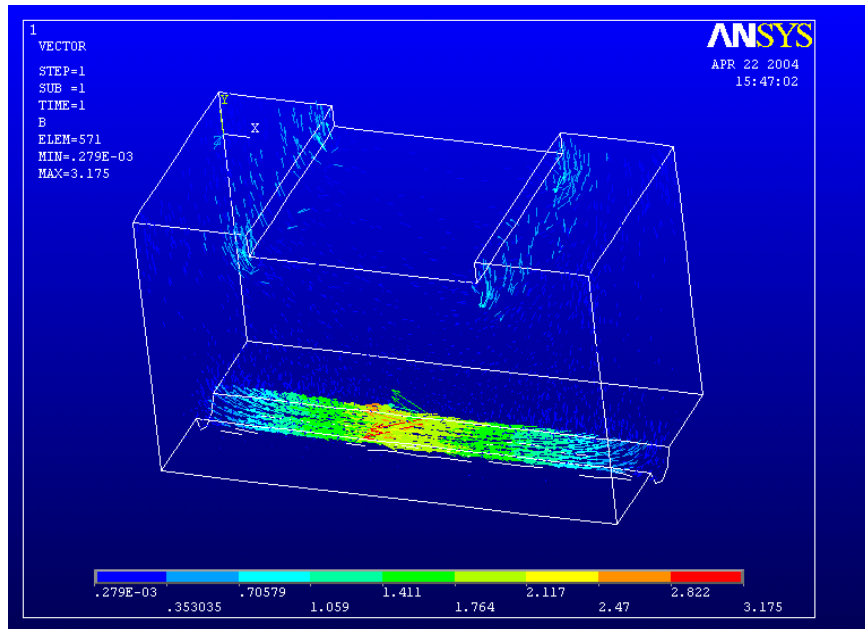
Figure 3-8: Magnetic flux density (B)
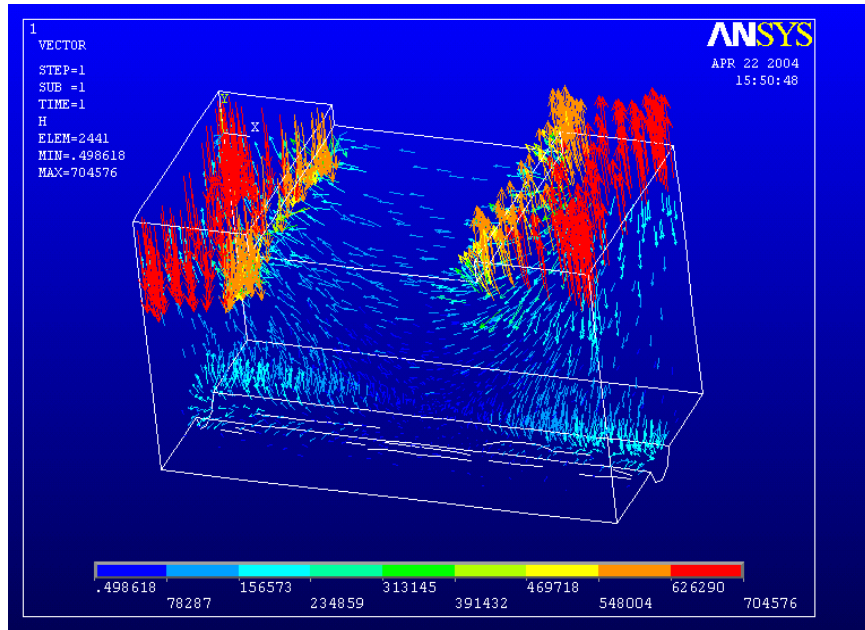
Figure 3-9: Magnetic flux intensity (H)
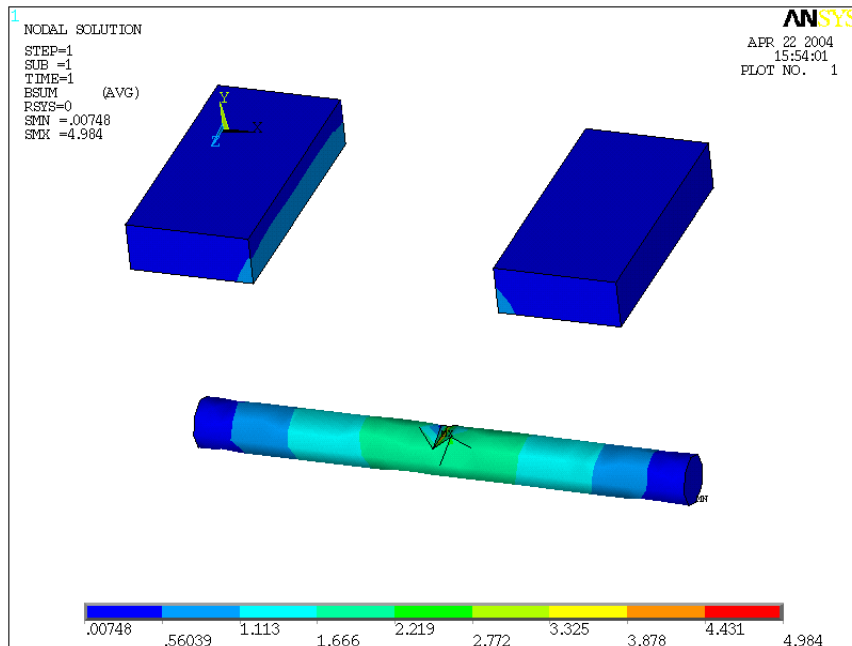
Figure 3-10: Sum of magnetic flux density (B)

3.2.4 FE Analysis of Notched Rebar with Additional Permanent Magnets

Figure 3-11 shows the third FE model here considered. Geometry, material properties and boundary conditions remained the same as previously mentioned with the exception of coercive force, which was increased because additional permanent magnets were added to the model.

The magnetic flux density vector (B) around the notch is a parameter of interest. It can be seen in Figure 3-12 that the flux does not flow thought the rebar as much as did in Figure 3-8. This occurs because of the magnets had a higher coercive force, which forces most of the flux to flow through the air between the two magnets, instead of flowing through the rebar. Consequently, the maximum magnitude of B, around the notch, was equal to 0.2 T. This value is much lower than in previous analysis.
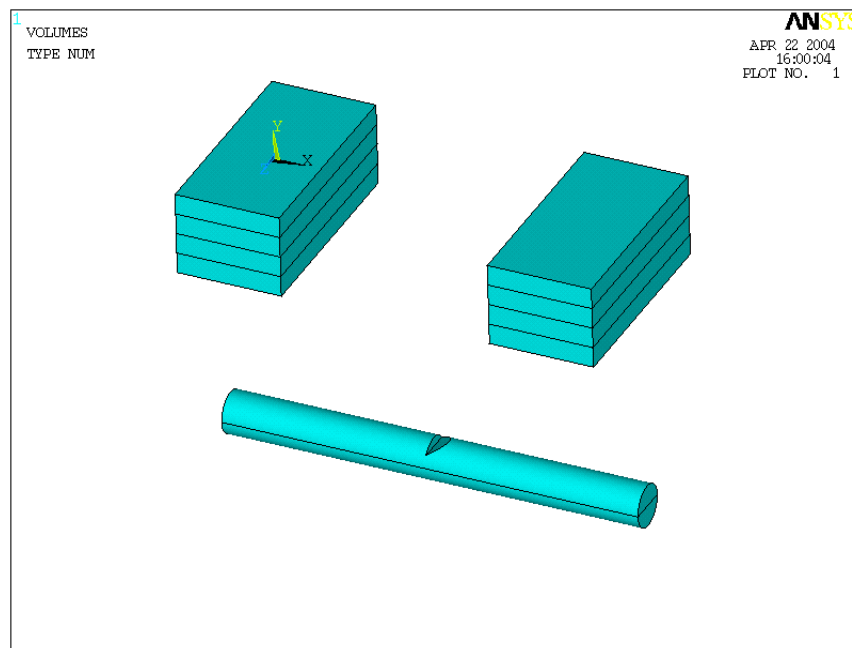
Figure 3-11: FE model considered for third analysis
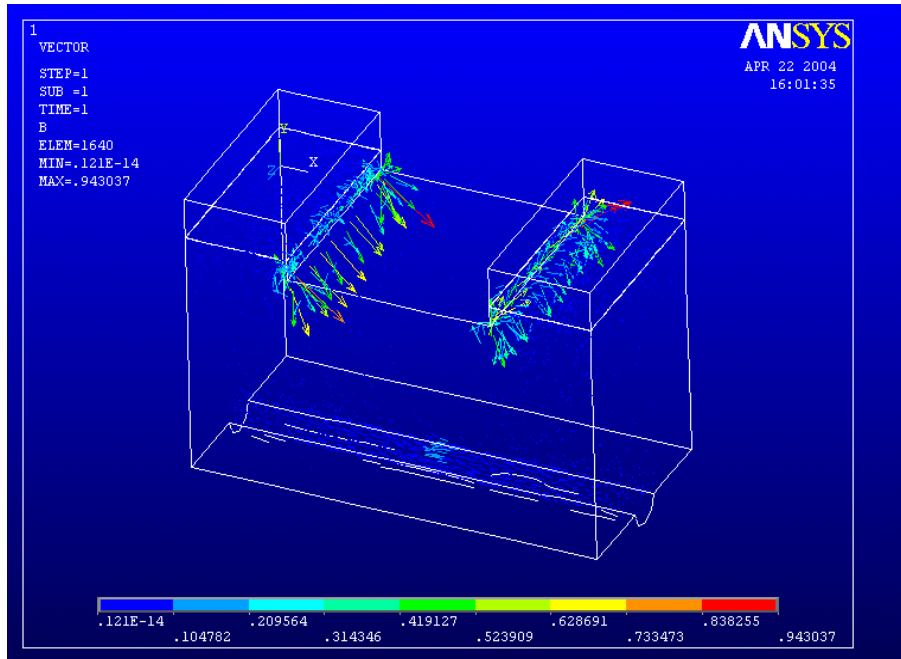
Figure 3-12: Magnetic flux density vectors (B)
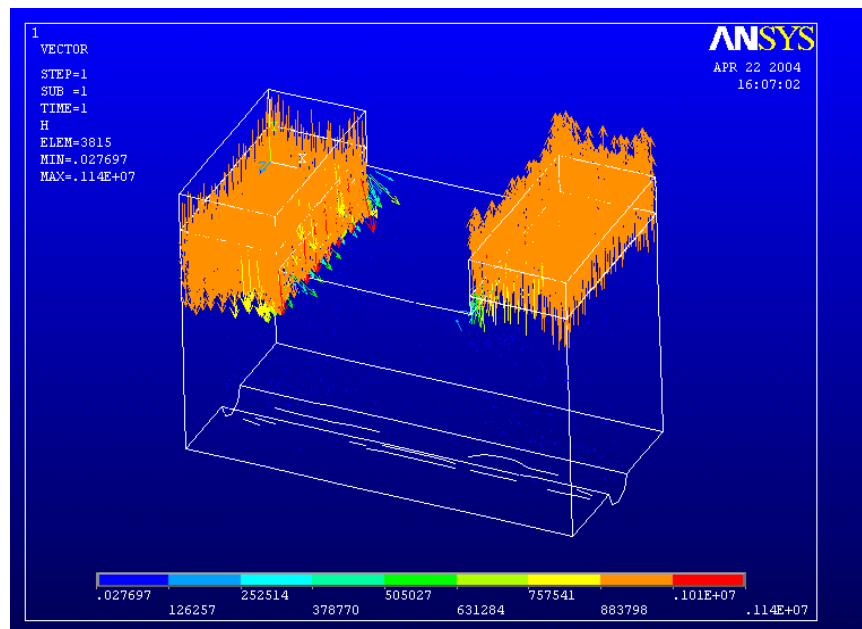
Figure 3-13: Magnetic flux intensity (H)
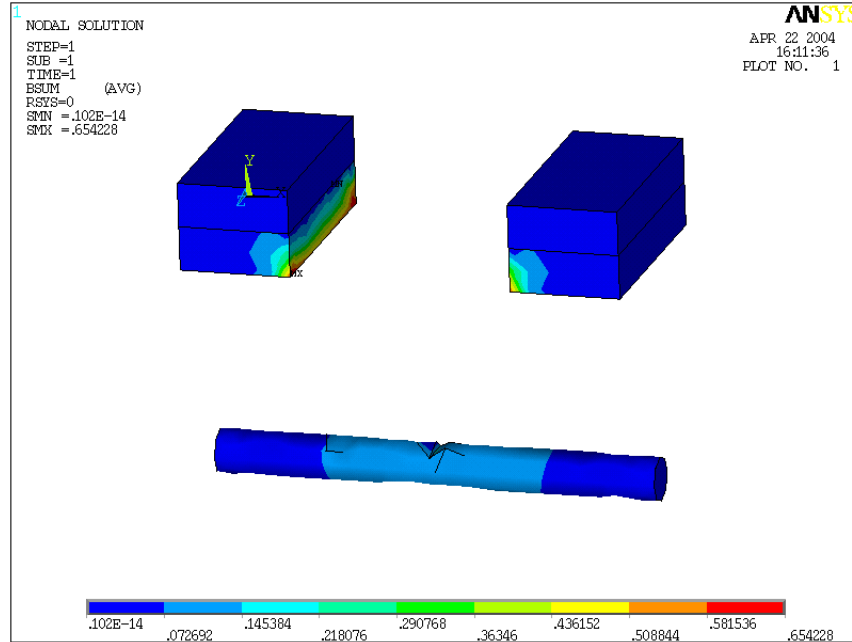
Figure 3-14: Sum of magnetic flux density (B)

The next finite element analysis was carried out to better understand the influence of additional magnets added into the model.

3.3 FE Analysis of the Magnetic Field around a Damaged Rebar

The FE model presented in this section was created to simply analyze the influence of the measured magnetic field if a greater number of magnets are used to measure the magnetic flux.

3.3.1 Model Description

The model here considered includes several cubic magnets and a cylindrical steel rebar. The material around the magnets and rebar is air. Figure 3-15 shows the dimension of elements and distances assumed to build the model.

Sintered neodymium-iron-boron (Nd-Fe-B) magnets were used as permanent magnets and material properties were assumed to be the same as previously described. Identical magnetic permeability of air and steel previously discussed are assumed here.

A material with similar magnetic permeability of air was chosen to surround the magnet and the rebar. This material was modeled by using a cube with a size almost 10 times that of the magnet's dimension. The flux-normal boundary condition was assumed to be zero at the outer surfaces of the air volume far from the magnet and rebar.
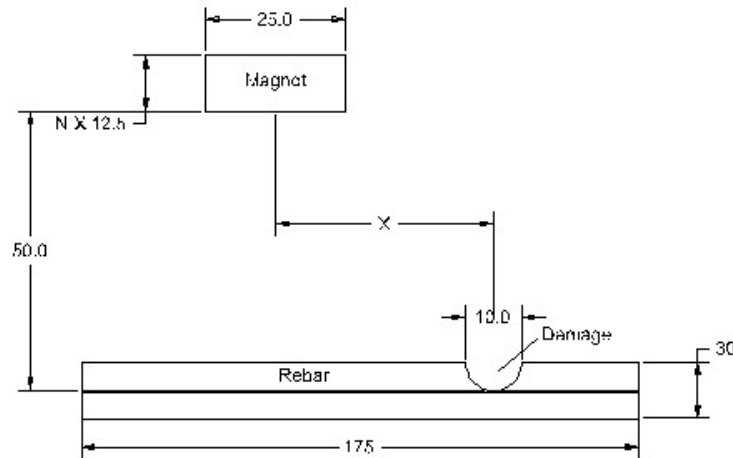
Figure 3-15: Dimensions of the model in mm

3.3.2 Analysis Procedure

The numerical simulations were carried out using ANSYS 5.7. The element type used for this model was the Solid98, which is a tetrahedral coupled-field element. A linear finite element magnetic analysis was carried out. Figure 3-15 shows all the dimensions considered to create this model. It used up to six magnets, with dimensions of 50 x 25 x 12.5 mm, placed one on the top of the other. The horizontal distance between the centers of the damage and the middle of the magnet is defined as "x". The selected variables considered for this simulation were the "x" distance and the number of magnets (N).

3.3.3 Analysis of Results

Figure 3-16 shows the results where the number of magnets varies for a given horizontal distance "x". This comparison was needed to evaluate the relationship between the number of permanent magnets and the maximum induced magnetic field

density. It can be seen in Figure 3-16 that the magnetic field density changes linearly with the number of magnets. The magnetic field was increased from 0.9T using one magnet to 1.1T for six magnets, which represents a change of 18% of the measured magnetic field.
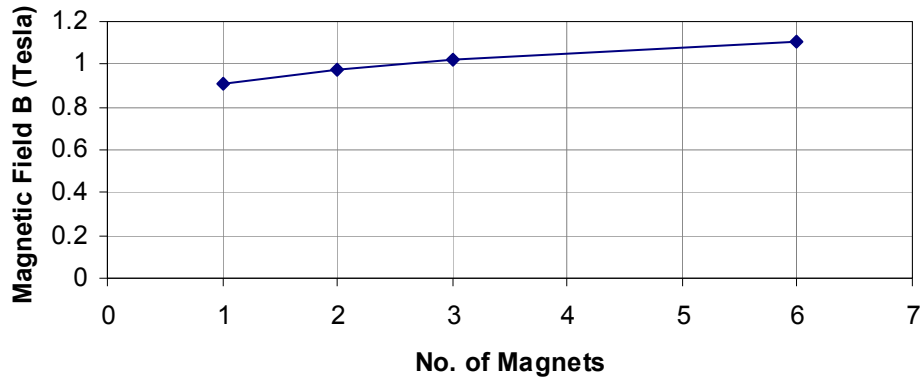
Figure 3-16: Comparison between the number of permanent magnets and maximum magnetic field

Figure 3-17 shows the finite element meshing assumed in the model and Figure 3-18 shows the magnetic flux density vectors (B).
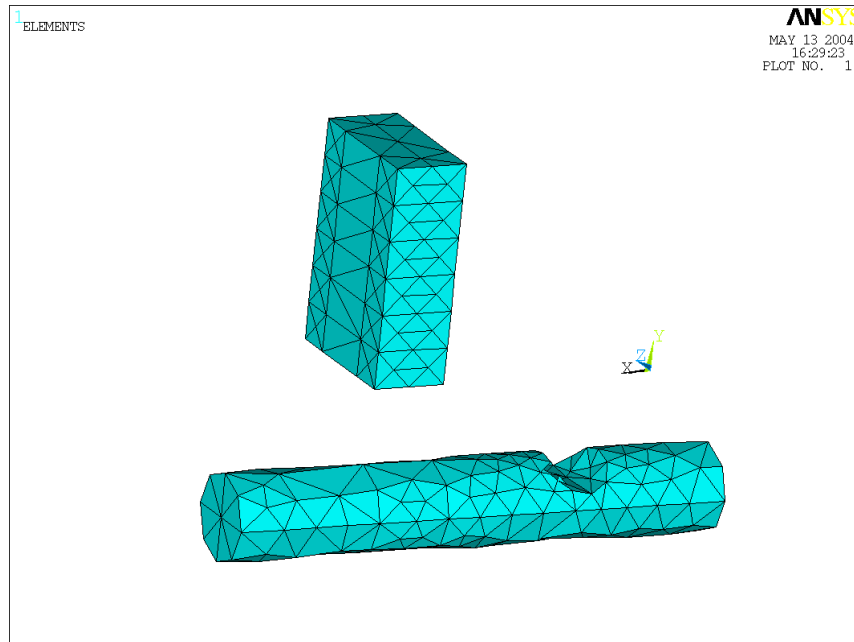
Figure 3-17: Finite element mesh considered
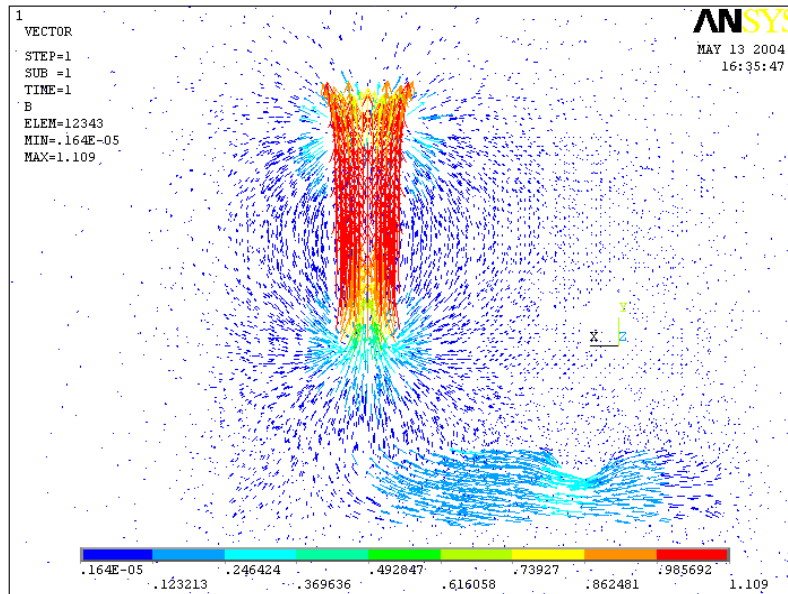
Figure 3-18: FE results of magnetic flux density vectors (B)

It can be noted that the FE results from all four previous numerical simulations are simply analyzed by either comparing or looking the results between the different models. In addition the preliminary finite element models do not consider any specific location to measure the magnetic field; therefore, no accordance with a MFL test was here simulated in the models.   The following models were considered to better comprehend and simulate a real situation during a MFL experiment.

3.4   FE Analysis of a U-Shaped Magnet around a Damaged Rebar

The FE model here presented differently from previous models assumes a specific location -- between two magnet Poles -- to measure the magnetic field in order to simulate a Hall-effect sensor. This model was used to carry out a parametric study to identity how sensitive is each variable independently. Prior to any further analysis, a validation of the FE model was conducted to assure the veracity of results obtained based on numerical simulation.

3.4.1 Model Description

Figure 3-19 illustrates the dimension of components and the distance between them. This FE model considers a steel rebar encased by a galvanized duct -- here called a shield -- which was subjected to a magnetic field provided by a U-shaped magnet. The material surrounding the elements is considered to be air (low magnetic permeability). All dimensions were chosen as variables for further parametric studies. Unless indicated, the dimensions are as described in Figure 3-19. The plots and tables indicate the system units used in the model. The same magnetic properties assumed in previous FE models were considered here.
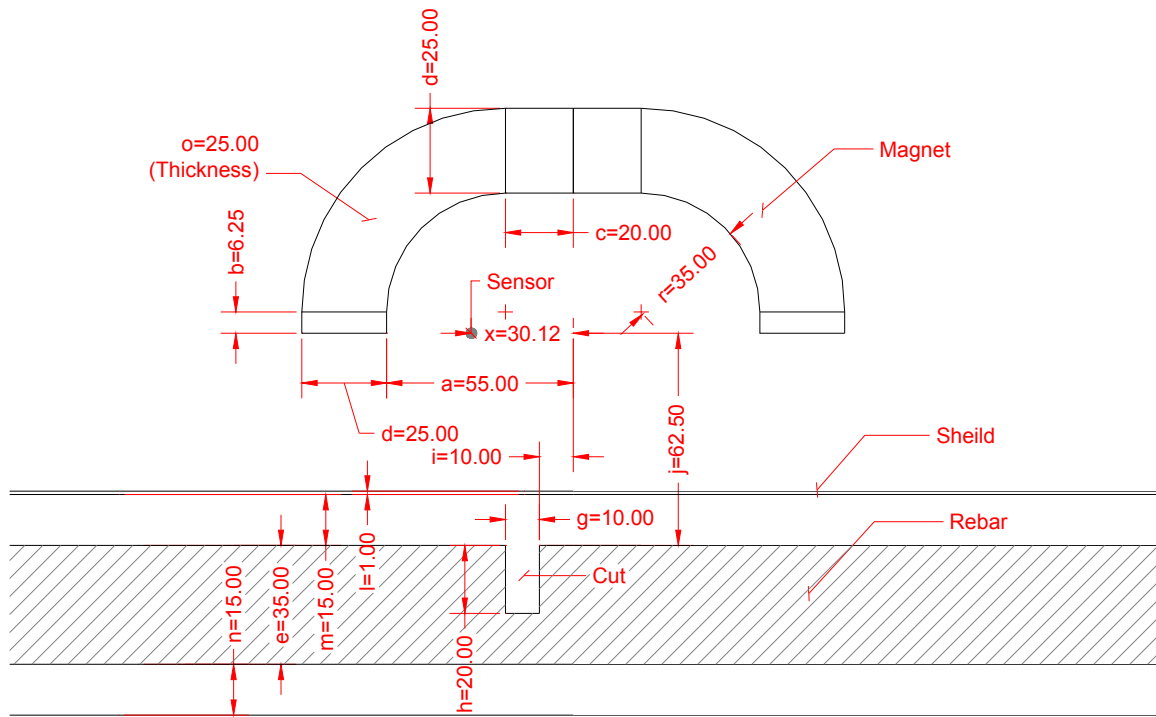
Figure 3-19: Dimensions of the model in mm and a description of parameter variables

3.4.2 Analysis Procedure

Numerical simulations were carried out using ANSYS 5.7. The model shown in Figure 3-20 assumes the material properties and dimensions previously mentioned. SOLID98, a tetrahedral coupled-field element, was used for three-dimensional finite element simulations and PLANE13, a 2-D coupled-solid, was used for two-dimensional

simulations. Because of the double-symmetry of the problem, only one quarter of the model was considered to be analyzed (see Figure 3-21). At the planes of symmetry, the magnet flux lines are orthogonal; thus, a zero flux-normal boundary condition was applied. INFIN47 and INFIN9 were used to simulate far boundary elements in the 2-D and 3-D models, respectively.

The smart meshing algorithm available in ANSYS was used to generate the mesh in the model. Mesh sensitivity analyses were carried out to study the influence of mesh size in results, where different element sizes were used to mesh model components. It can be seen in Figure 3-22 that the accuracy of results does not change if the mesh size is less than or equal to 8 mm. Mesh size smaller than 7 mm could not be used because the ANSYS has a limitation of 32000 degrees of freedom.

Figure 3-20 identifies the location where the magnetic field density in X-direction was measured. The top of the shield at a coordinate of x=0, y=-(j-l-m) and z=0 were the chosen points.

The reduced scalar potential (RSP) strategy was selected as no current sources were defined in the model.
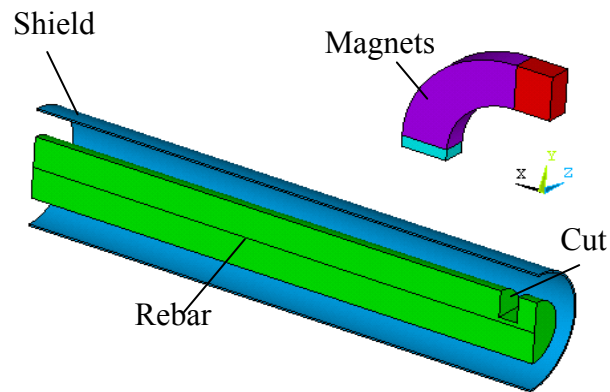
Figure 3-20: One quarter of the FE model
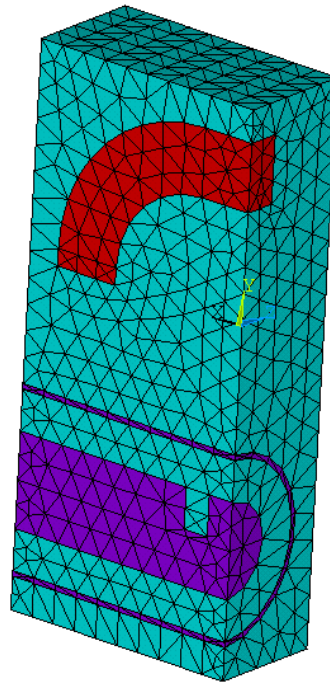
Figure 3-21: Meshing of the FE model using tetrahedron element
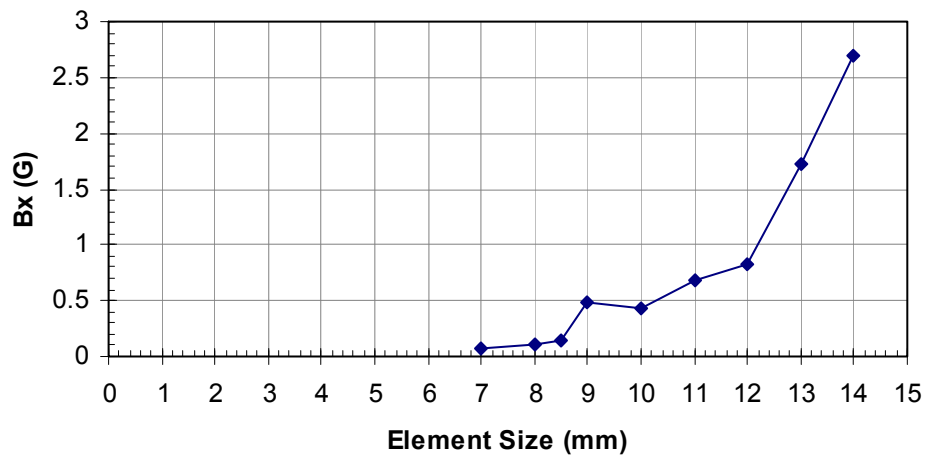
Figure 3-22: Mesh sensitivity analysis results

3.4.3 Experimental Verification

The finite element model was verified by comparing the results obtained from FE analysis and the experimental test carried out in the laboratory.

Figure 3-23 shows the U-shaped magnet and Gauss meter used in the laboratory test. For the FE model verification, the rebar and shield were not considered in both numerical and experimental tests. The following parameters have different values than those previously shown in Figure 3-19.

$a = 50$ mm

$b = 43.75$ mm

$c = 18.75$ mm

$o = 50$ mm

The magnetic flux density was measured by F.W. Bell Gauss meter Model 5080, shown in Figure 3-24. By using iron powder, it was possible to visualize the magnetic flux lines of the U-shaped magnet (see Figure 3-24). Table 3-1 summarizes the results from both numerical and experimental tests. The table contains the reading location, direction of magnetic flux vectors and magnitude of flux. Theoretically, the magnetic flux density in the Y-direction at origin point (x=0, y=0, z=0) should be zero due to the symmetry. However, the laboratory test gives a flux density of 95 G at this point and finite element analysis provides 0.45 G at the same location. As a result, the error tolerance of experimental measurement was considered to be ±95 G and ±0.45 G for the finite element analysis. Differences which are greater than 95 G between the numerical analysis and the experimental test might be due to imperfection in the U-shaped magnet, the material properties assumed in the model and possible ambient magnetic fields.

With that in mind, it can be concluded that the finite element modeling had a good agreement with experimental measurements if the magnetic flux in the Y-direction is the parameter of interest.

Figure 3-23: U-shaped magnet and Gauss meter used in laboratory test

Figure 3-24: Magnetic field visualization using iron powder

Table 3-1: Comparison of experimental results (Test) and finite element analysis (FEA)

Location of measurement				Magnetic Field Density (B)		
X	Y	Z	Direction	Test	FEA	Error
mm	mm	mm	Axis	G	G	%
0	0	0	X	650	770	-
0	0	0	Y	95	0.45	0
62.5	0	0	Y	5160	5920	11
50	12.5	0	X	2600	2600	-
0	-25	0	X	400	634	-
0	-25	0	Y	70	0.18	0
62.5	-25	0	X	800	934	-
62.5	-25	0	Y	100	179	0
0	100	0	X	350	807	-
0	100	0	Y	20	34	0

3.4.4 Parametric Study

Parametric studies were carried out to investigate the influence of each variable independently. Unless otherwise indicated, the dimensions for each study are the same as defined in Figure 3-19. The following parameters have been used:

$b = 12.5$ mm

$c = 6.25$ mm

$e = 20$ mm

$h = 10$ mm

For each parametric study, one parameter is selected for variation while the others are kept constant. The location where the magnetic field density component was read was located at x=0, y=0 and z=0. Except in the analyses where the sensor location changes. The maximum element size considered for the parametric study was 10 mm and automatic meshing was used to mesh the model.

Two approaches were considered: the first one considers the analysis of the rebar without any imperfection and the second considers the analysis of the rebar with cut.

With results from both approaches, the difference of the magnetic field density in Y-direction is taken and later plotted against the values of the variable in matter.

3.4.4.1   The Width of Magnet, "*c*"

The width of magnet "c" was set to vary from 6.25 mm to 50 mm. The dimensions were kept the same as previously described in Figure 3-19, except that the bar diameter and cut depth was equal to 20 mm and 10 mm, respectively. The shield was not considered in this model. The difference between the two magnetic fields versus the width of the magnet is illustrated in Figure 3-25. It can be concluded that magnetic flux is not sensitive to the width of the magnet.
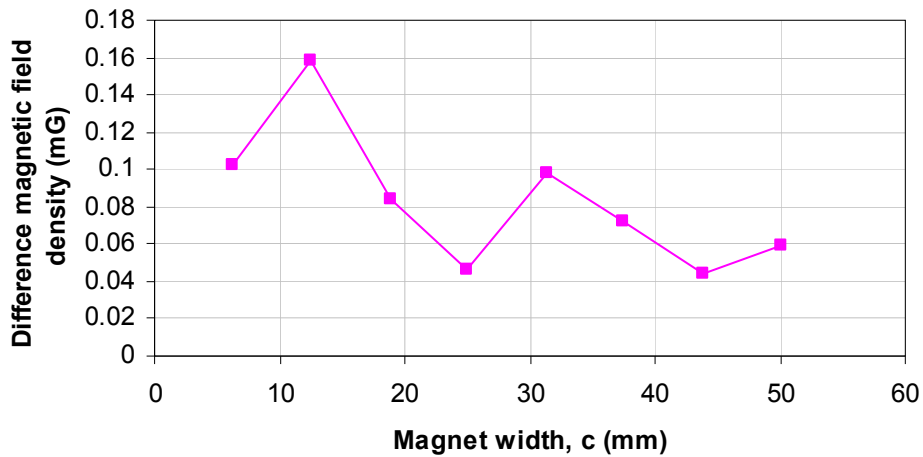
Figure 3-25: Variation of the magnetic field due to change in magnet width

3.4.4.2   The Depth of Magnet, "*b*"

The depth of magnet "b" was set to vary from 12.5 mm to 50 mm. All other variables remained constant except the width of the magnet, which was equal to 12.5 mm. The galvanized duct was not considered. The finite element results are shown in Figure 3-26. The change in sign and magnitude of the magnetic field can be due to an increase of strength of the bottom magnet which adverts the effect of the top magnet.
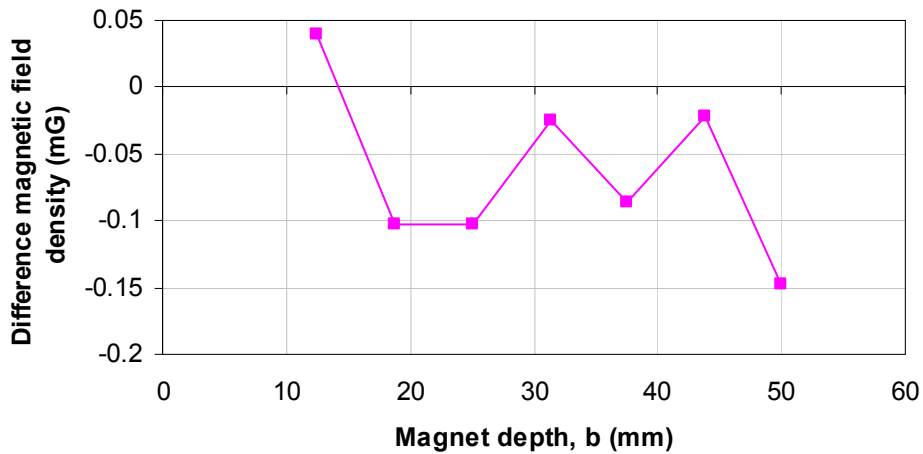
Figure 3-26: Variation of magnetic field due to change in magnet depth

3.4.4.3 Rebar Diameter, "*e*"

The bar diameter "e" was set to vary from 20 mm to 50mm while the cut depth "h" was assumed to be half of rebar diameter (h=e/2); therefore, the damage loss was equal to 50 percent of the cross-section of the bar for all cases. The other parameters were fixed as described in previous sections. The duct was not considered. The variation of the magnetic field versus bar diameter is shown in Figure 3-27. It can be noted that since the percentage of section loss is constant, the magnetic flux does not change drastically with change in rebar diameter.
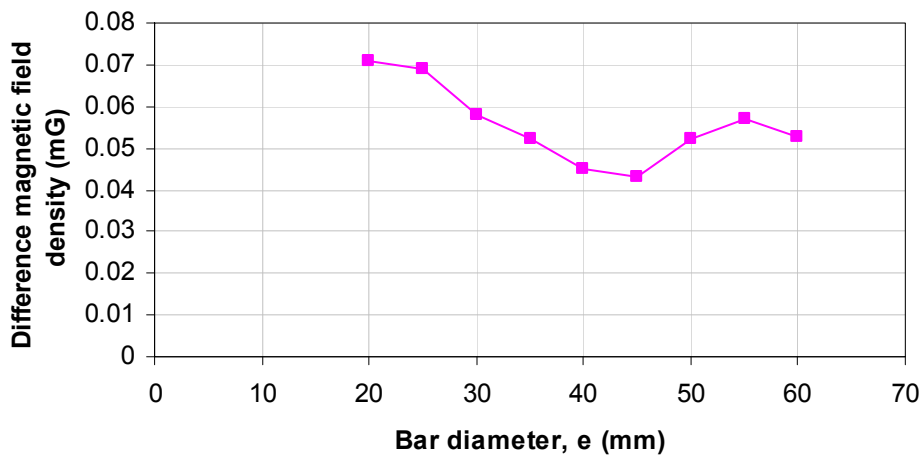
Figure 3-27: Variation of magnetic field due to change in bar diameter

3.4.4.4 Cut Depth, "*h*"

To measure the effect of percentage of section loss on magnetic field leakage, the cut depth "h" was set to vary from 2 mm to 19 mm while the damage width "g" was kept constant and equal to 10 mm. No shield was considered. It can be seen in Figure 3-28 that the magnetic field is highly sensitive to the damage depth. For a greater depth, a higher magnetic flux is expected.
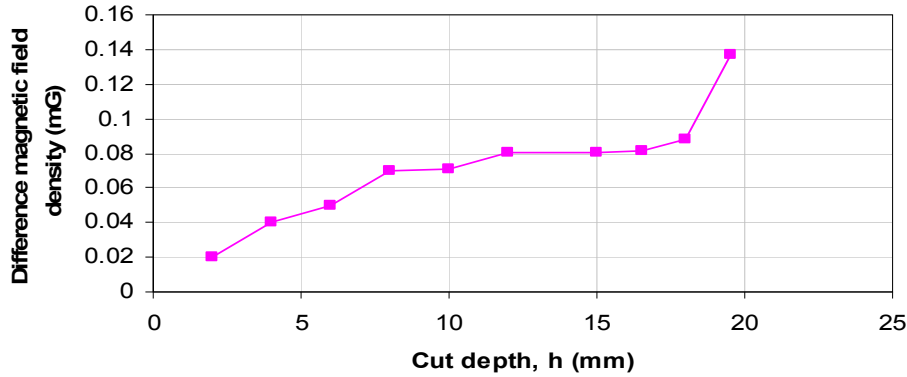
Figure 3-28: Variation of magnetic field due to change in cut depth

3.4.4.5 Sensor Location, "*x*"

The location of sensor "x" was set to vary from 0 mm (the initial position) to 90 mm. Figure 3-29 shows the best location to read the magnetic flux. The galvanized duct was not considered. It can be seen that the maximum absolute value is located between the damage width "g" and the width of magnet "d".
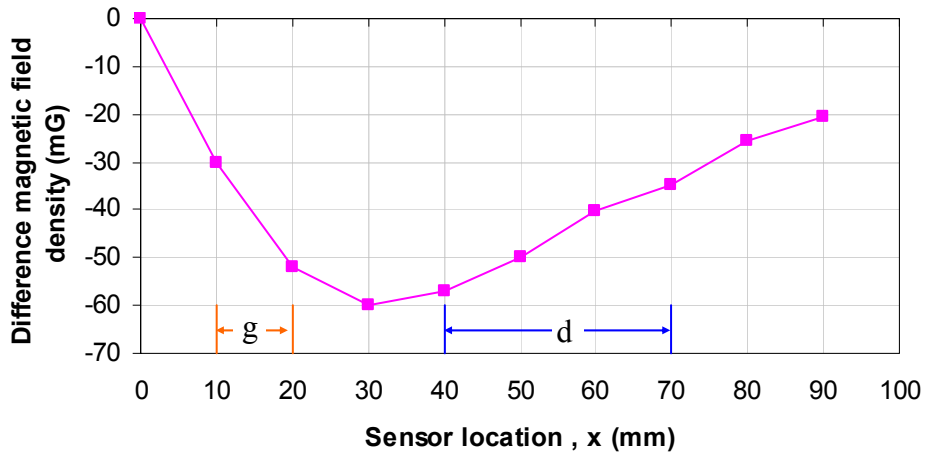
Figure 3-29: Variation of magnetic field due to change in location of measurement

3.4.4.6   Damage Location, "*i*"

The damage location "i" was set to vary from 0 mm (the initial position) to 80 mm. The duct was not considered in the model. The variation of magnetic field versus the cut location is shown in Figure 3-30. It can be seen that the maximum value occurs at the location closest to the internal edge of the permanent magnet, represented by the two vertical broken lines.
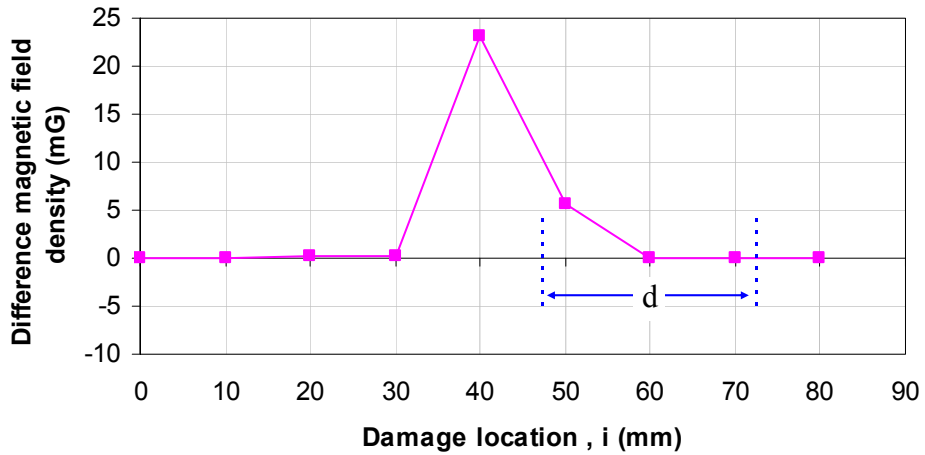
Figure 3-30: Variation of magnetic field due to change in damage location

60

3.4.4.7 Masking Effect, "*l*"

The masking effect "l" was here investigated in order to simulate a situation where prestressing strands were located inside a steel duct.

Two analyses were carried out, where one includes the duct and the other does not. Due to meshing restriction, the thickness of the shield was taken as 2 mm. For the first case, the measured variation of magnetic flux density at the location of the sensor (x=0, y=0, z=0), with or without damage, was 0.07 mG. In the second case, which considers the shield, almost no flux difference was observed. Figure 3-31 shows that almost all flux flows through the shield. Therefore, damage in the rebar could not be detected since steel inside the duct did not reach the saturation point and no magnetic flux could leak through the damage.
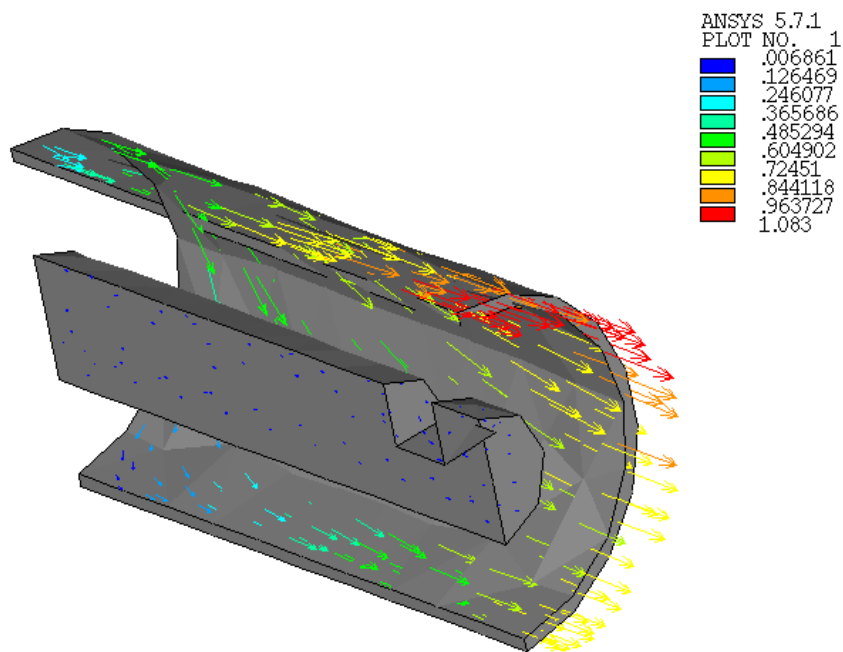
Figure 3-31: Magnetic flux density vectors through rebar and shield

The best magnetic configuration, which was obtained during experiments carried out previously and described in Chapter 2, is considered in the next section. Results and conclusions obtained after recent finite element simulations are discussed next.

3.5   2D FE Model of U-Shaped Magnet

The magnetic configuration no.5 is here modeled to better comprehend the behavior of the magnetic flux when in the presence of a damaged rebar. Similar trends obtained in Chapter 2 could be here identified, such as peak-and-valley disturbance in the measured magnetic field and magnetic flux flowing through the steel.

3.5.1 Model Description

A 2D FE model of a U-shaped magnet -- identical to magnet configuration no. 5 -- and a corroded rebar were modeled using ANSYS 10.0. The model simulates the magnetic flux during the passage of the magnet over a corroded area. The FE magnetic model, which consists of seven pieces of neodymium magnets and six pieces of iron magnets, was created. The material properties assumed were the same as previously mentioned.

A longitudinal rebar with 2 in. diameter is modeled in 2D space. The rebar is initially located 2 in. from the bottom of the magnet. A cut 3 in. long and 1.5 in. deep is created in the rebar to simulate a loss of cross section.

Figure 3-32 shows the magnetic flux around the U-shaped magnet in the absence of rebars.
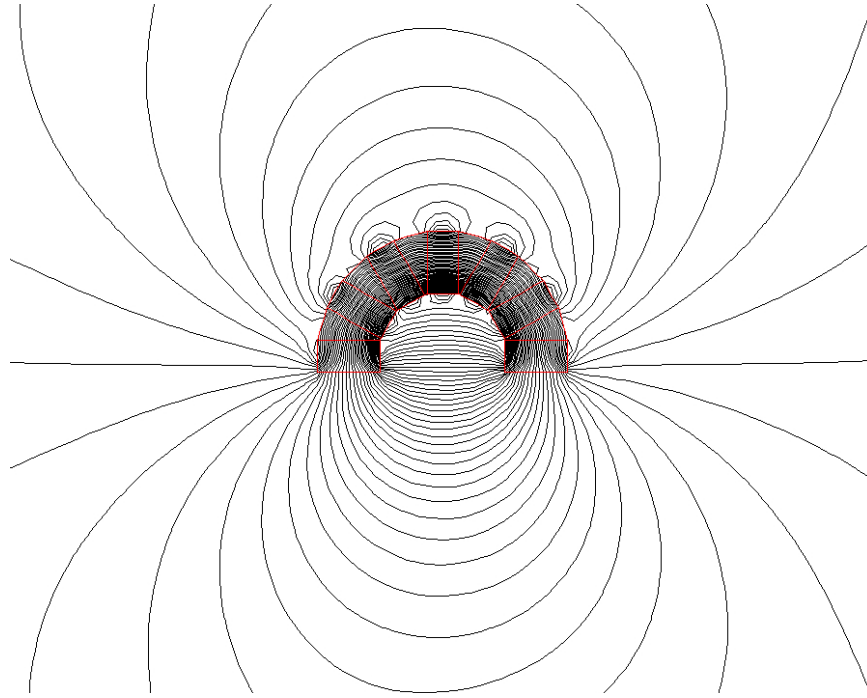
Figure 3-32: The flux of the magnet surrounded by air

3.5.2 Analysis of Results

Figure 3-33 shows the magnetic flux around the rebar without any corrosion. Figure 3-34 through Figure 3-38 show the magnetic flux lines flowing through the rebar while the magnet assumes different positions.

It can be noted that the magnetic flux lines flow through the rebar rather than the surrounding material (air). The flux lines are highly concentrated at the notch region, which implies a saturation of magnetic flux. This forces some of the flux to leak through the cut.
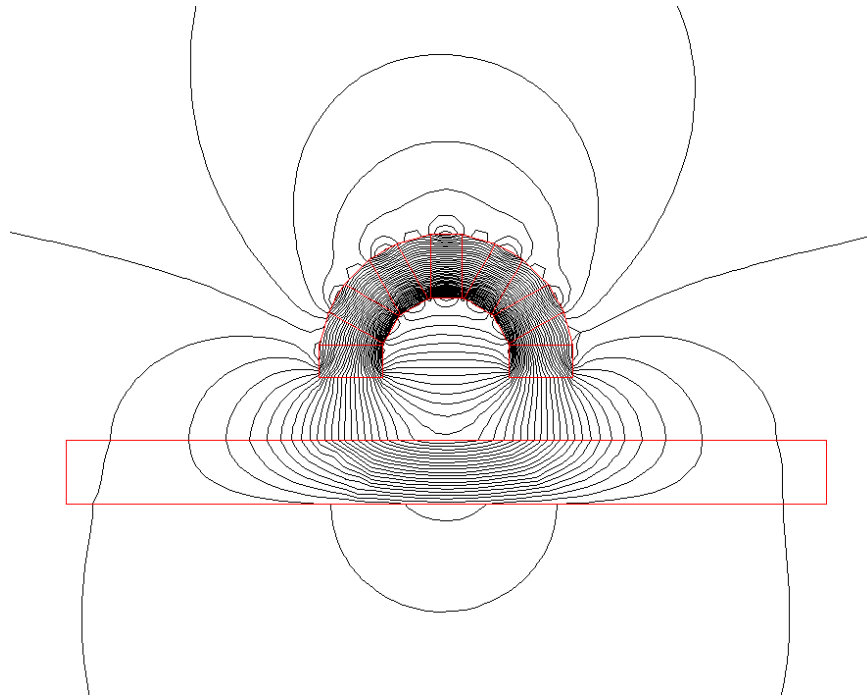
Figure 3-33: The magnetic flux around a non-corroded rebar
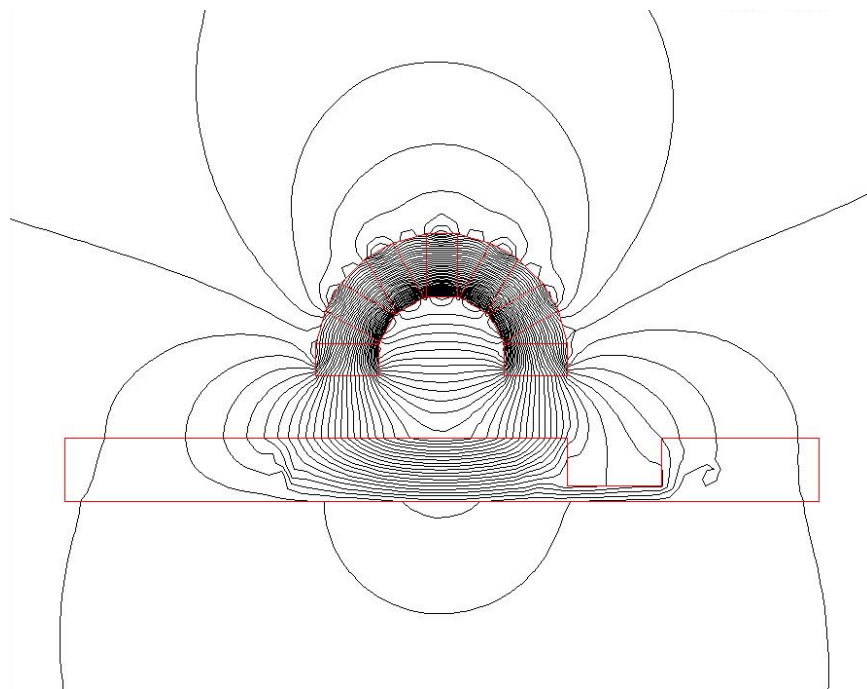
Figure 3-34: The magnetic flux around a corroded rebar at position A
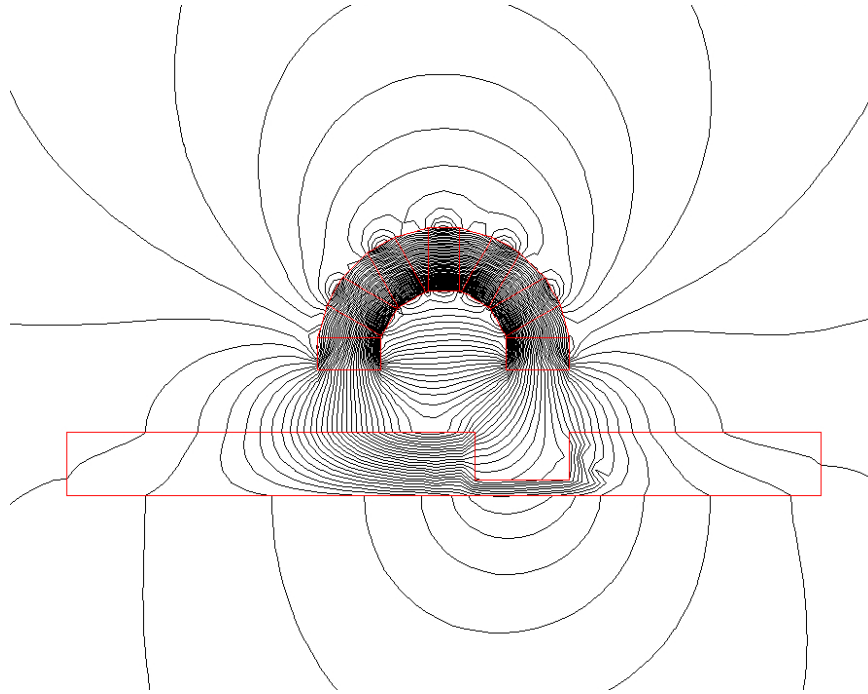
Figure 3-35: The magnetic flux around a corroded rebar at position B
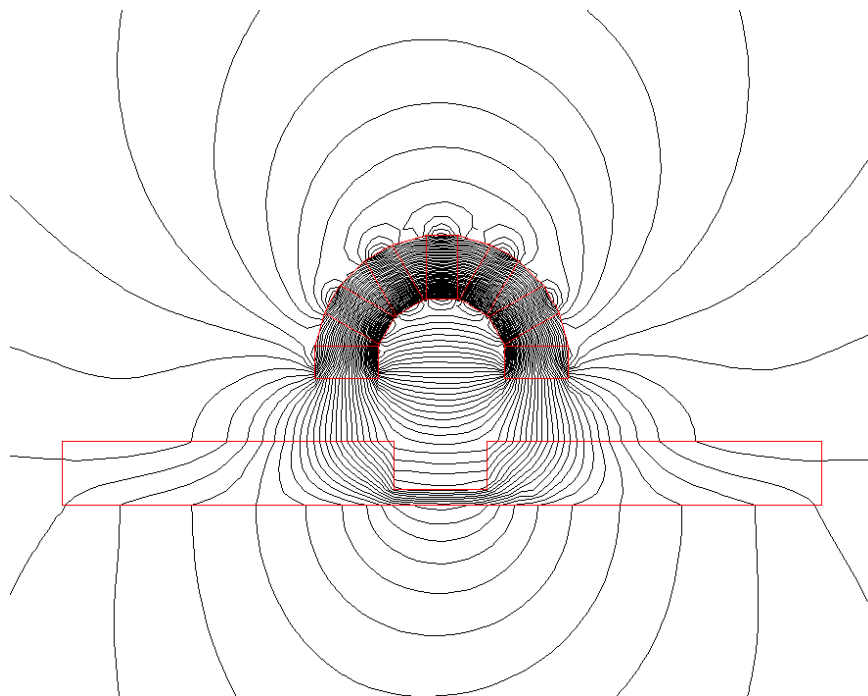
Figure 3-36: The magnetic flux around a corroded rebar at position C
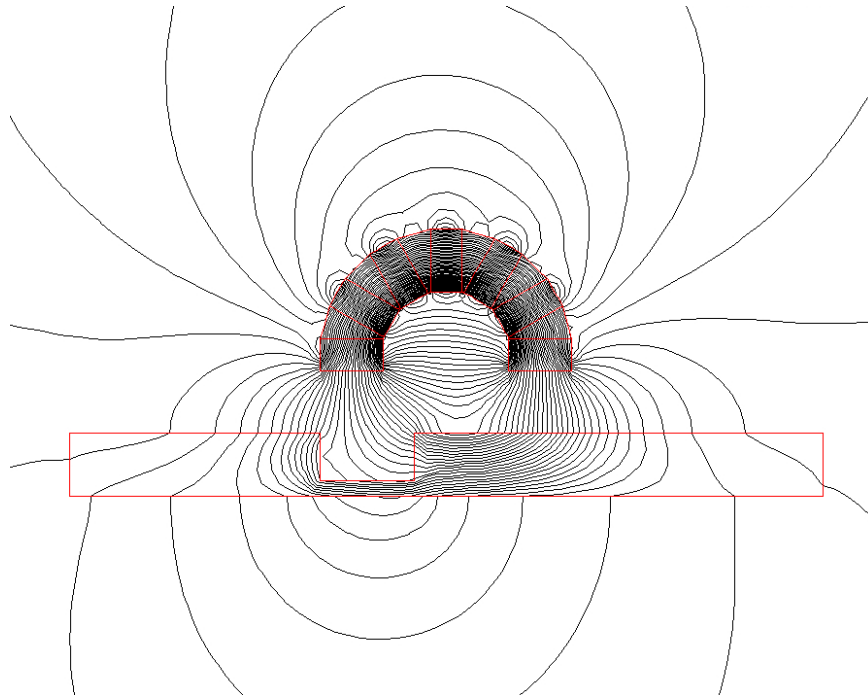
Figure 3-37: The magnetic flux around a corroded rebar at position D
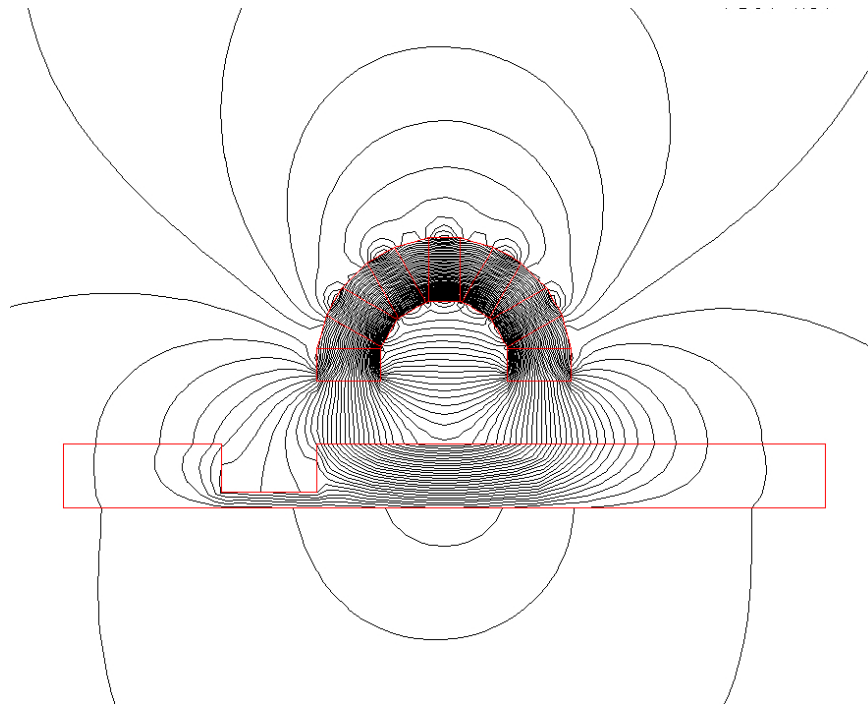
Figure 3-38: The magnetic flux around a corroded rebar at position E

Figure 3-39 and Figure 3-40 show the change at vertical and horizontal components of magnetic flux. The magnetic flux was calculated using the FE model for all five positions previously shown in Figure 3-34 through Figure 3-38. The point where the flux was obtained is located at mid-point between the two poles of the U-shaped magnet.
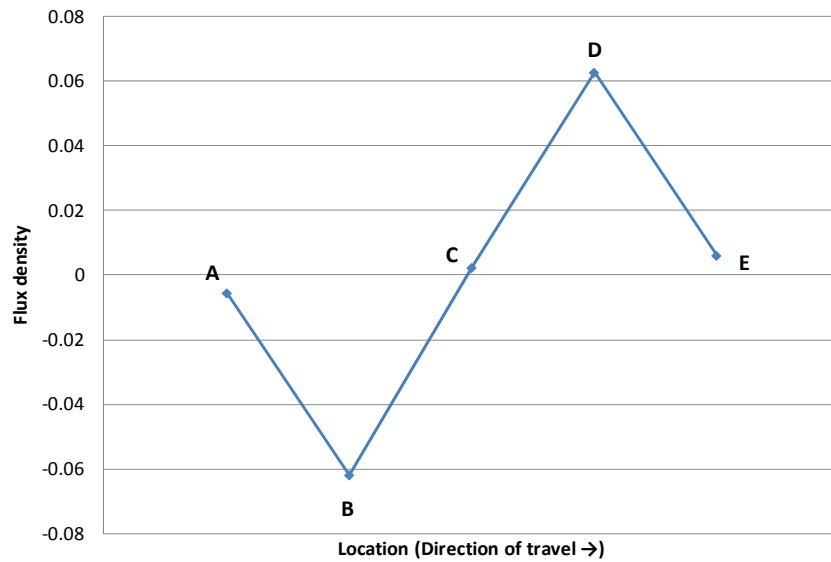
Figure 3-39: Vertical component of magnetic flux
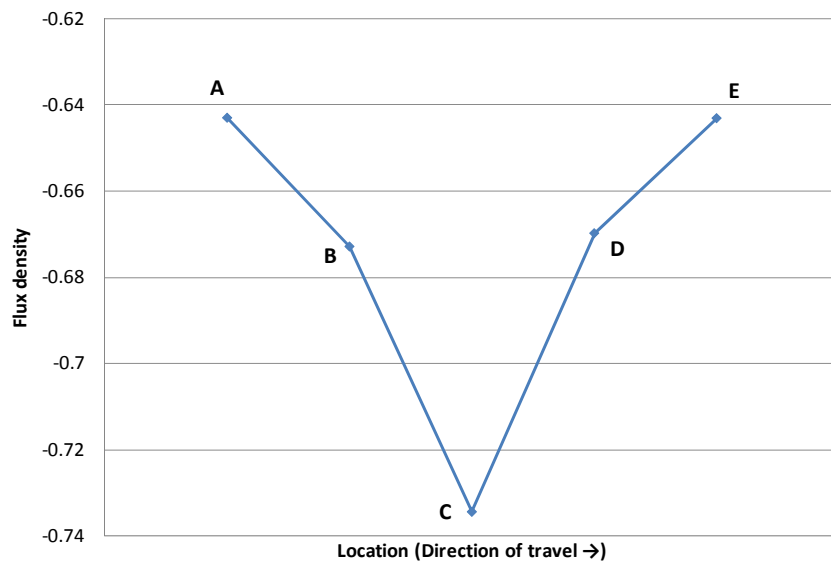
Figure 3-40: Horizontal component of magnetic flux

Figure 3-41 shows the results obtained using the FE model for a great number of magnet positions. Note the peak-and-valley behavior observed in previous MFL test results, such as shown in Figure 2-14 (Chapter 2). A great accordance between the numerical simulations and the experimental results are here presented.
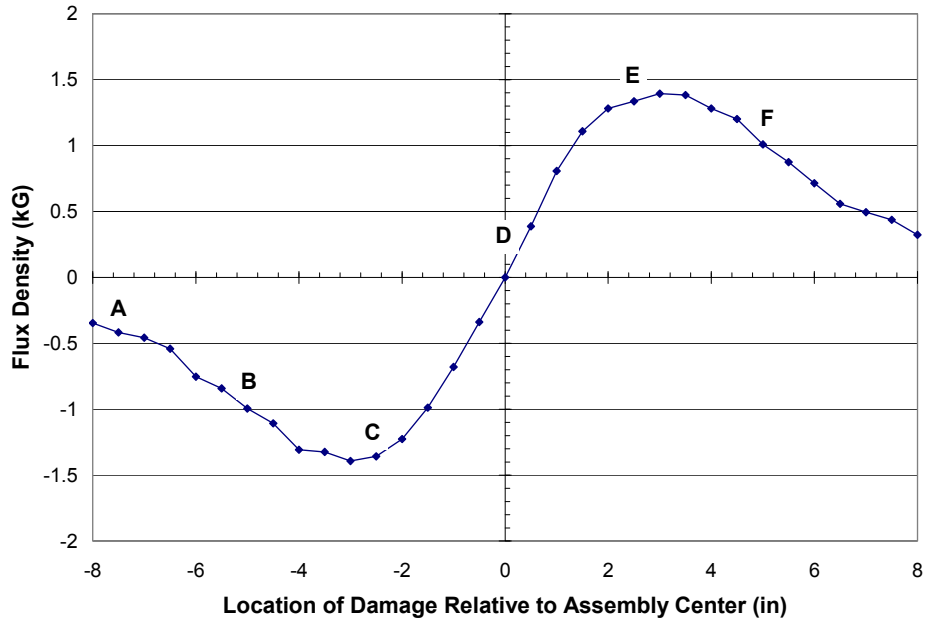
Figure 3-41: Numerical results

Figure 3-42 shows the FEM results in 3D space. Y-axis represents the vertical magnetic flux (B_y). X-axis simply represents any point far away from the rebar, which is located at Z-axis. The rebar is limited by two white dots shown below.
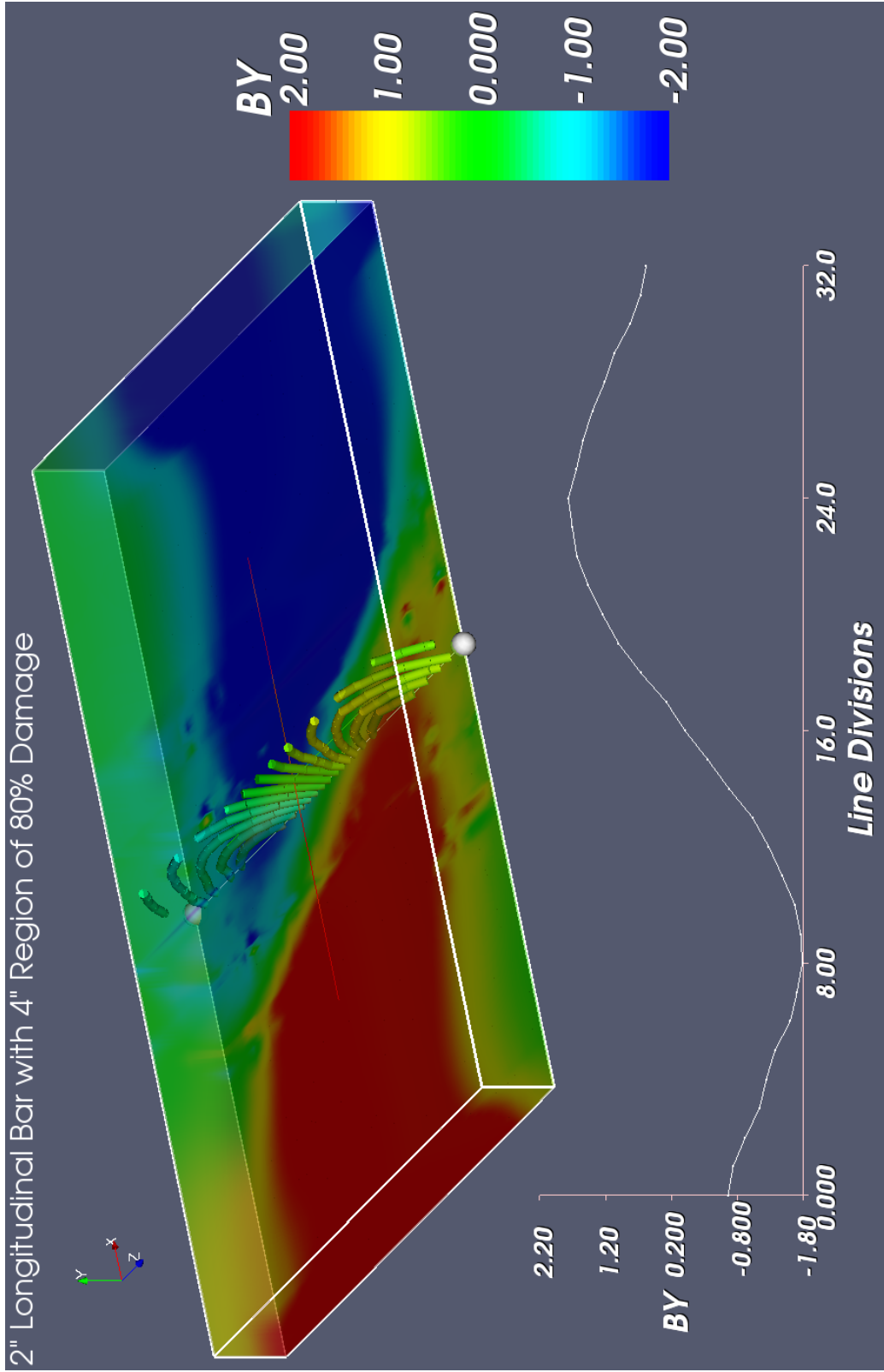
Figure 3-42: Magnetic field variation in the presence of corroded rebar

3.6 Conclusion

The finite element method was capable of reproducing similar results to those obtained in laboratory testing. The FE models were verified with the experimental results.

Parametric studies have shown that measured magnetic flux can be drastically influenced by four distinct parameters, such as meshing sizing, cut depth, locations of the sensor and damage location.

The masking effect caused by the galvanized duct previously observed in testing conducted in Chapter 2 was also observed in the finite element simulations.

Literature and preliminary laboratory testing have pointed out that the residual method is more sensitive and is usually used to detect low corrosion levels in ferromagnetic materials. Therefore, it is desirable to perform additional finite element analyses focused on the residual method.

With the knowledge gained and knowing the main parameters that may affect magnetic flux, a newer version of the MFL device was developed, which is the subject matter of the following chapter.

Chapter 4

MFL Tests Using Three Sensors

4.1 Introduction

Based on the knowledge gained, a second version of the non-destructive device was developed. This second version was more user friendly for field application purposes. Three Hall-effect sensors were used to measure the magnetic field during experiments. An aluminum cart was designed to carry the magnet and electronic parts. A magnet made with rectangular blocks of neodymium magnets was used. This chapter provides a detailed description of the device as well as a summary of all tests performed.

4.2 Test Setup

Aluminum in comparison with steel has a very low magnetic permeability, which usually can be neglected. With that in mind, an aluminum cart was used to carry all electronic parts and the magnet. Three Hall-effect sensors were used to measure the electrical potential in the perpendicular direction. The distance between the sensors and the duct were considered constant. The residual MFL method was used for all tests.

Figure 4-1 shows the aluminum cart. The front wheel has a trigger sensor which is controlled by data acquisition software. Three Hall-effect sensors were located between the wheels. During the cart movement, the trigger sensor activates the Hall-effect sensor, wherein the data acquisition software records the position and electric potential at the location. Figure 4-2 shows magnet configuration no. 5, which was used to magnetize the strands. Figure 4-3 shows the location of sensors with respect to the magnet.

Figure 4-1: MFL device assembled over aluminum cart

Figure 4-2: U-Shaped magnet used
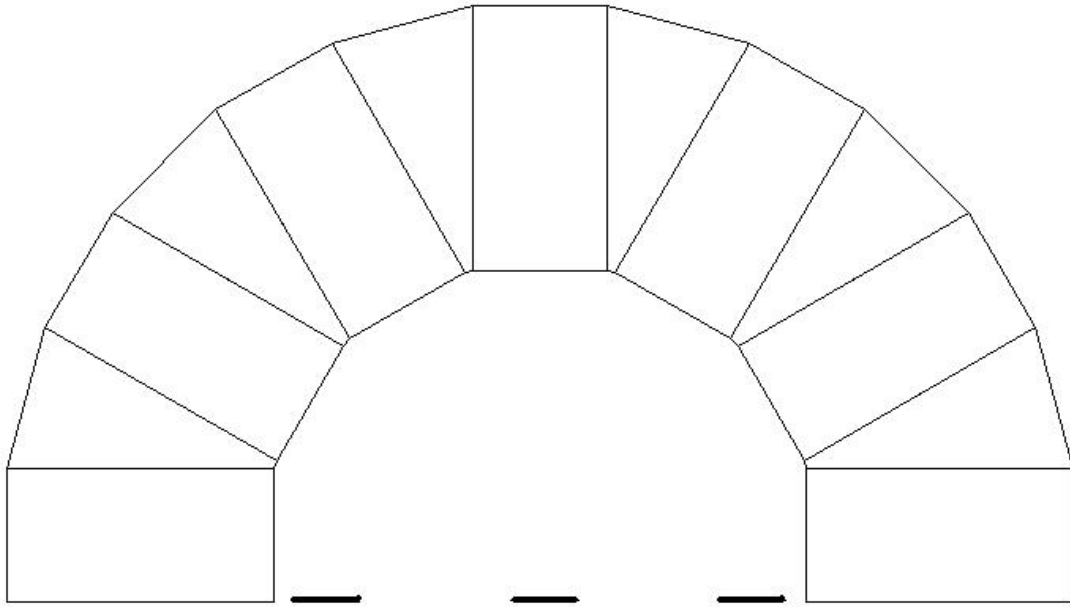
Figure 4-3: Location of sensors

Figure 4-4 shows the wooden frame that was built to hold all elements involved in the test. Plywood sheets were used to create a flat surface on the top of concrete bricks, so the cart could travel during testing.

Figure 4-4: Test setup before running

All tests were carried out considering 19 prestressing strands, which were placed into the corrugated steel duct. Corrosion was simulated by leaving a gap along the strands. Figure 4-5 and Figure 4-6 show the tests which consider transversal bars.

Figure 4-5: Test setup considering four transverse bars

Figure 4-6: Test setup considering one transverse bar

Four different test setups were considered to study the effect of transverse rebars on the magnetic field. For each study, either continuous or discontinuous strands were used. The tests conducted are described below:

1. No transverse rebar
2. One transverse rebar located at the middle
3. Four transverse rebars with 12 in. spacing
4. Four transverse rebars with 24 in. spacing

Table 4-1 shows each test configuration. A name was assigned to identify each test configuration. All plots are presented in the next section. The red, green and blue curves represent the results from front, middle and rear sensors, respectively. The title of each chart matches the name assigned in Table 4-1.

Table 4-1: Test configuration

Name	Continuous Strands	Non-Continuous Strands	Transverse Rebar
D19_0	19	-	-
D19_0_T1	19	-	1
D19_0_T4	19	-	4@12"
D19_0_T4_24	19	-	4@24"
D0_19	-	19	-
D0_19_T1	-	19	1
D0_19_T4	-	19	4@12"
D0_19_T4_24	-	19	4@24"

4.3   Analysis of Results

The results show that the experiments could predict the location of the transverse rebars with accuracy. Table 4-2 shows the predicted and measured distance between the transverse rebars.

Table 4-2: Comparison between real and predicted locations of transverse rebars

Predicted Distance (in.)	Measured Distance (in.)	Difference (in.)
D19_0_T4		
11.37	12	0.63
12.6	12	0.6
12	12	0
D19_T4_24		
23.97	24	0.03
23.95	24	0.05
23.35	24	0.65
D0_19_T4		
12.6	12	0.6
11.36	12	0.64
12.62	12	0.62
D0_19_T4_24		
24.6	24	0.6
23.96	24	0.04
23.97	24	0.03

Some trends can be noticed in all tests that consider continuous strands. The measured electrical potential assumes the greater absolute value at the beginning and end of each test. This response is due to the leakage of magnetic flux at the ends of strands, described previously as the boundary effect. Since the strands are continuous, the magnetic flux does not leak, which explains why the electrical potential in the middle is practically steady. The presence of transverse rebars creates small and local peak-and–valley disturbance in the field; however, it does not change the slope of the curve.

D19_0
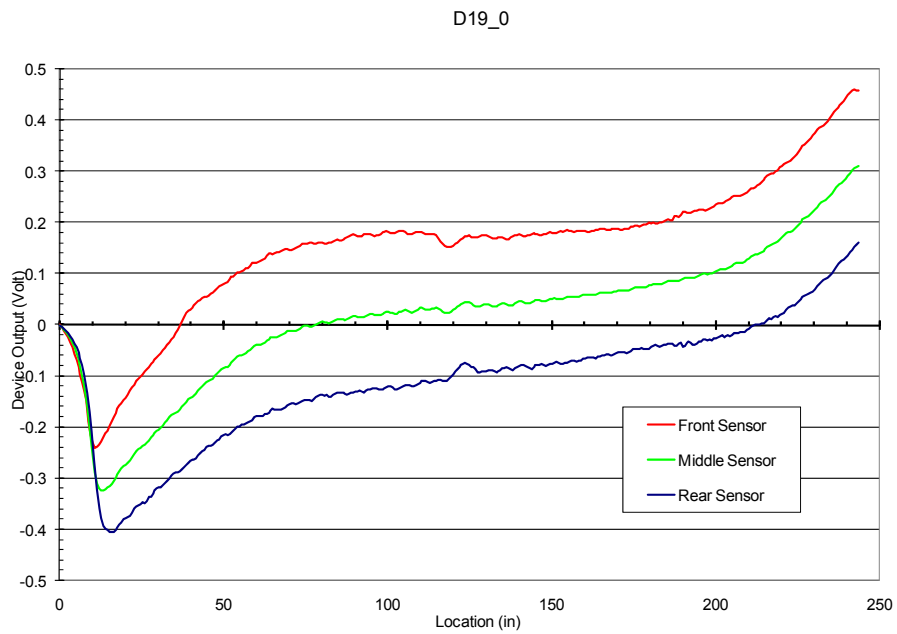
Figure 4-7: Test results for 19 continuous strands with no transverse rebar

D19_0_T1
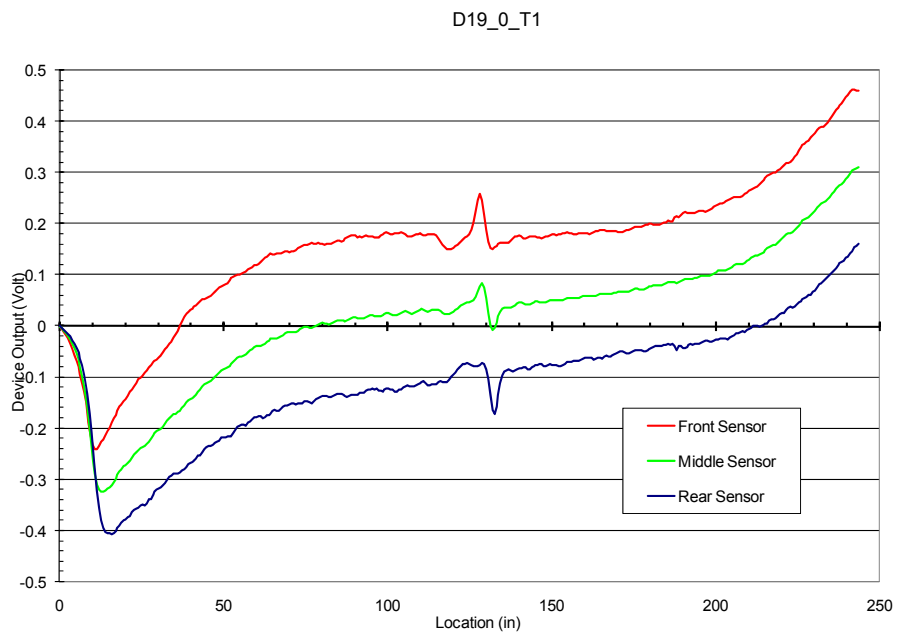
Figure 4-8: Test results for 19 continuous strands with one transverse rebar

D19_0_T4
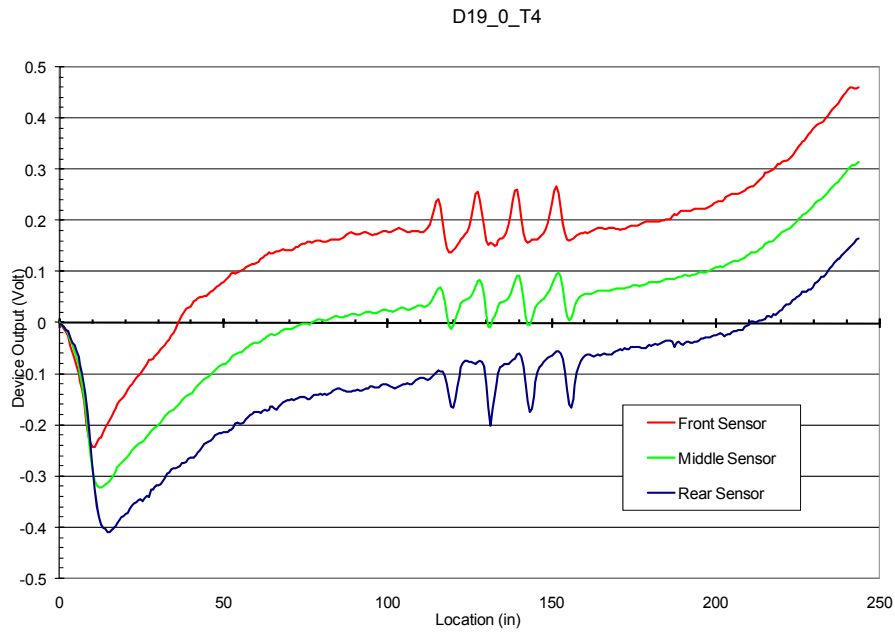
Figure 4-9: Test results for 19 continuous strands with four transverse rebars (12" spacing)

D19_0_T4_24
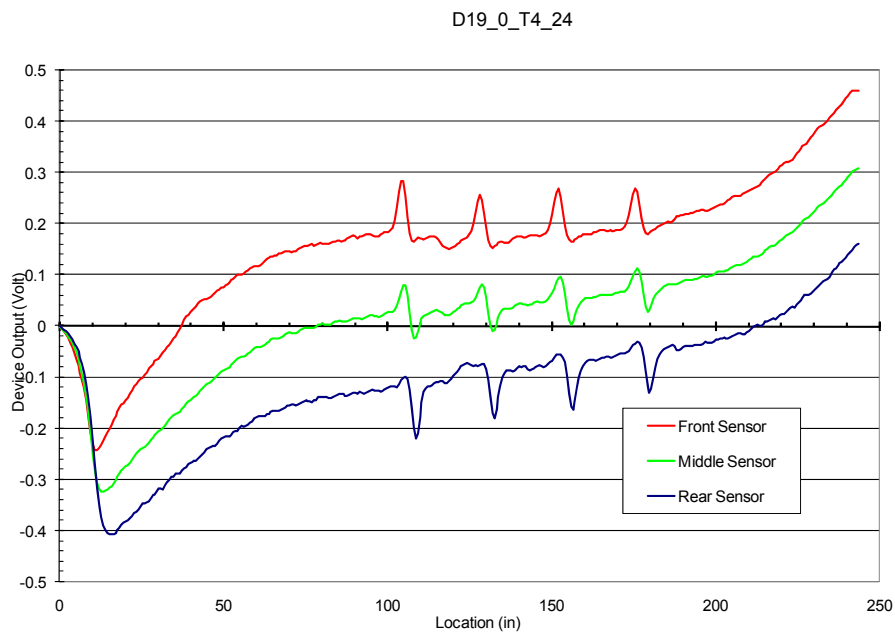
Figure 4-10: Test result for 19 continuous strands with four transverse rebars (24" spacing)

Discontinuity in the middle of the test creates a new boundary which forces the magnetic flux to leak. The measured electrical potential is disturbed due to this leakage,

creating a peak-and-valley disturbance at the location of the gap. Differently from the transverse rebars, the disturbance created by the gap changes the slope of the curve.

The peak and valley mid-point can be used to predict the location of the gap. In other words, the corrosion here simulated by the gap can be clearly located by finding the mid-point of the measured magnetic field. Table 4-3 compares the results from the real and predicted mid-point position of the gap. A very good agreement between the real and predicted position can be seen.

Table 4-3: Longitudinal position of the mid-point of the gap

Test Configuration	Predicted Position (in.)	Measured Position (in.)
D0_19	132.1	131.25
D0_19_T1	132.45	131.25
D0_19_T4	131.8	131.25
D0_19_T4_24	131.8	131.25
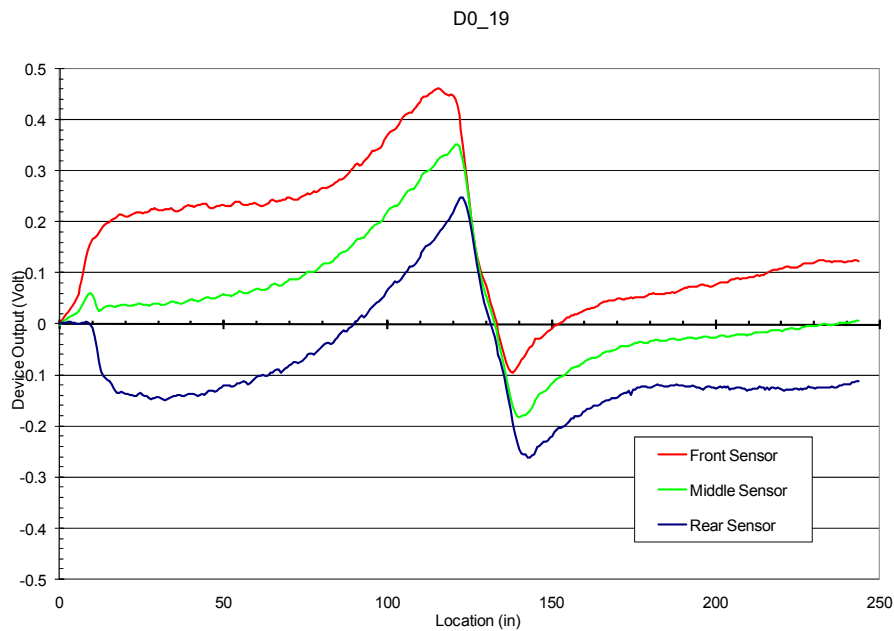
Figure 4-11: Test result for 19 non-continuous strands with no transverse rebar
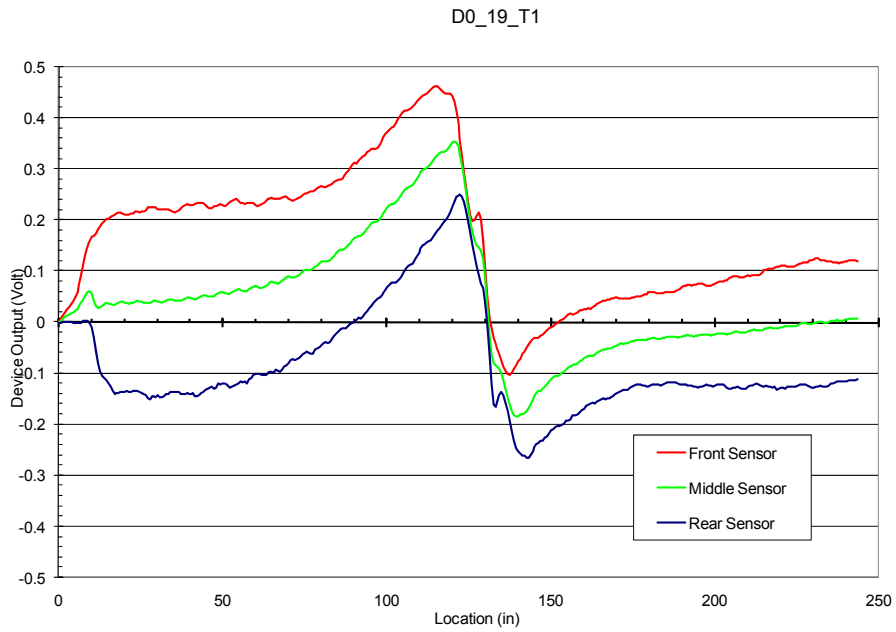
Figure 4-12: Test result for 19 non-continuous strands with one transverse rebar
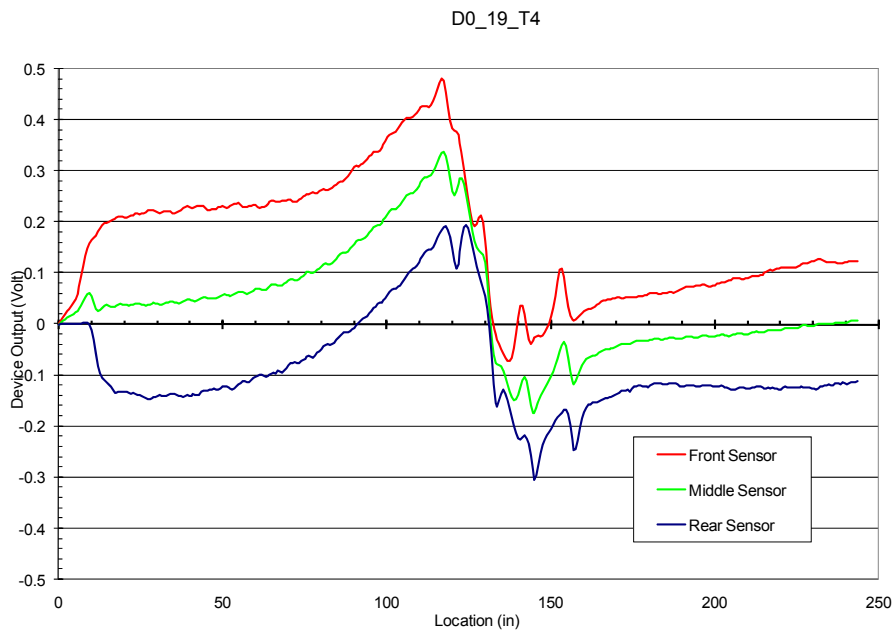
Figure 4-13: Test result for 19 non-continuous strands with four transverse rebars (12" spacing)

80

D0_19_T4_24
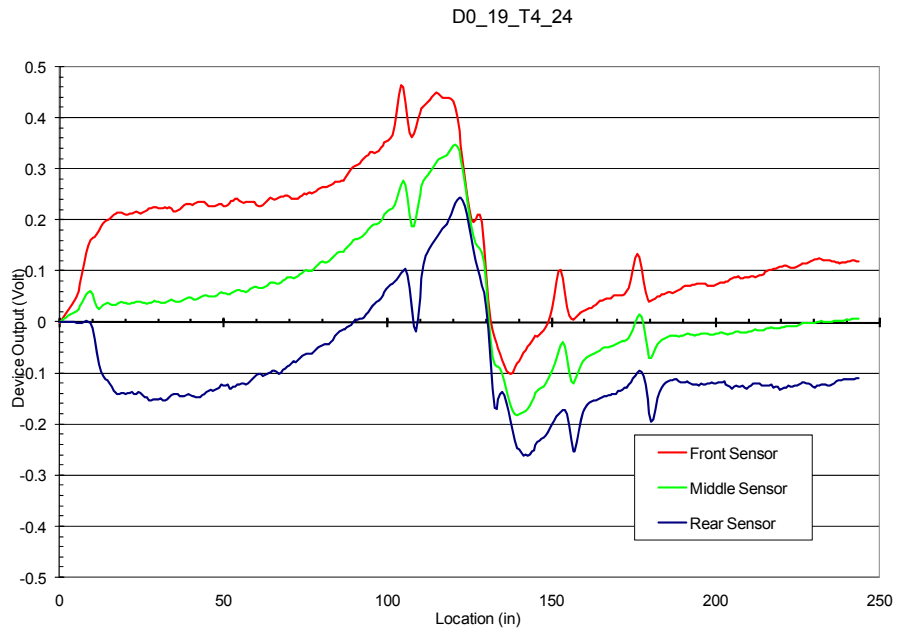
Figure 4-14: Test result for 19 non-continuous strands with four transverse rebars (24" spacing)

Figure 4-15 shows a 3D view of the test with a gap embedded at the middle of the test span.
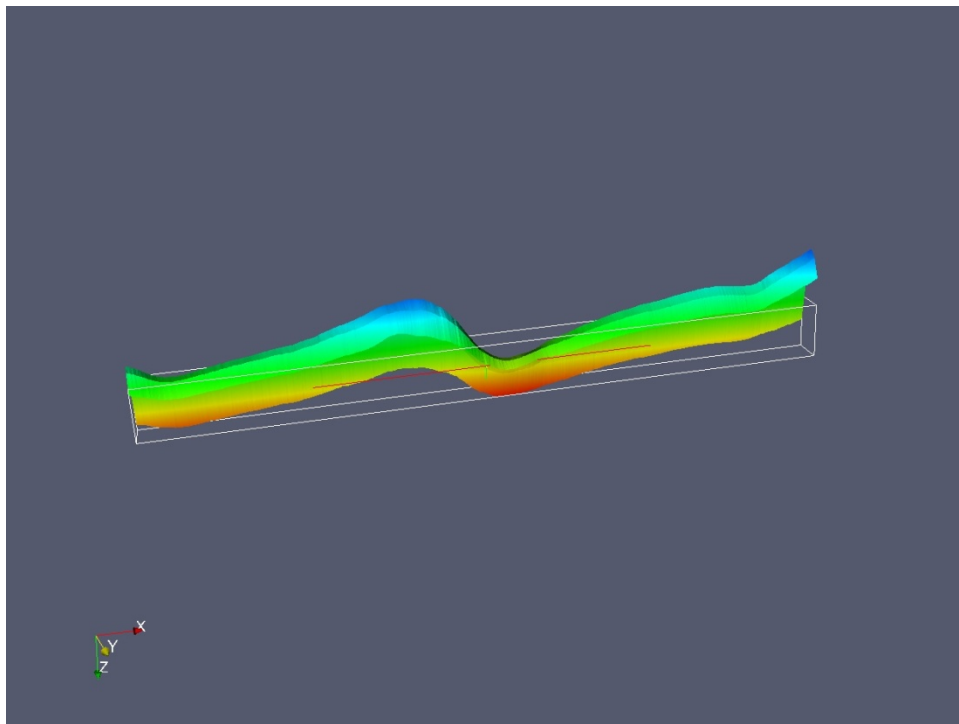
Figure 4-15: 3D plot of the test shows the gap at the middle

4.4 Conclusion

The MFL device here developed was capable in aiding the location of the gap and transverse rebar with a high accuracy for all test configurations.

The measured magnetic field is expected to have a steady behavior if no gap (corrosion) is present on the strands. Two distinct disturbances can be noted. The first one, considered here as local, is caused by the transverse rebars. The measured field suffers only minor changes, which were here considered as small and local peak-and-valley disturbances. On the other hand, the disturbance caused by the absence of strands -- created by the gap -- greatly affects the measured field, which drastically changes the slope of the measured magnetic field. This alteration, called the boundary effect, was previously observed and once again here detected. Concrete structures usually have constant rebar spacing; this can help to differentiate the peak-and-valley disturbance created by a gap (corrosion) from the peak-and-valley disturbance created by the transverse rebar. The ends of the strands create either a peak or a valley. It should be noted that corrosion at this stage of the project was simulated by using fully non-continuous strands, which means all cross section has been lost.

The shortcomings of the second version of the non-destructive device are as follows:

- There is no possibility of changing the height of the sensor with respect to the surface being scanned.
- The magnetic flux cannot be measured transversally since all the sensors are lineup.
- There are a limited number of sensors, which reduces the robustness of the device.
- The dimensions of the device are relatively bigger, which reduces device mobility for field application.

As the result of these conclusions, it was decided to modify the device, which is the subject matter of the following chapter.

Chapter 5

MFL Tests Using 15 Sensors

5.1   Introduction

This section presents the description of the non-destructive device, which uses the principles of magnetic flux leakage to detect corrosion in ferromagnetic material embedded in concrete. The currently developed device was used to carry out laboratory experiment over a wooden slab. The slab was built to simulate the innumerous situations such as only duct, only transverse and/or longitudinal rebar, only strands with full, partial and no damage that an engineer could face during a field inspection. A total number of 14 different lanes of experiments were considered. The active method was considered to conduct the experiments. The results and conclusions are here presented and further discussed.

5.2   Description of MFL Device

The current MFL device is designed to operate in both laboratory and field environments and also in both active and residual methods to detect corrosion on ferromagnetic material embedded in concrete. A group of 15 Hall-effect sensors are connected to the electronic board to measure the magnetic field. The sensors are located exactly in the middle between the North and South Poles of the magnetic yoke, if the active method is considered. This location was previously mentioned to be the best location to measure the field. The magnetic configuration no.5 -- considered the best magnetic -- is the magnetic of choice. The overall size and weight was reduced so that the device can be easily carried without any extra effort. It is now possible to vary the height of the sensors with respect to the surface prior to a test, which was not possible in previous devices. Also, the cart now rolls over two aluminum tracks, which facilitates the guidance of the device during experiments. With a simply wheels rearrangement, it is possible to conduct tests on a vertical surface.

Figure 5-1 shows the final version of the MFL device. The equipment has seven primary components as described below:

a) ***Housing:*** The housing is constructed with aluminum. In addition to being light weight, the aluminum does not affect the magnetic field if the assumed speed is kept low (Figure 5-1 a, b, c and e).

b) ***Guide Rails:*** Guide rails transport the housing (Figure 5-1 a and e).

c) ***Position Indicator:*** The position indicator, which is a proximity sensor, incorporates the trigger mechanism (Figure 5-1 c).

d) ***Magnetic Yoke:*** The magnetic yoke previously developed is used as the magnetic source and consists of rectangular blocks of neodymium magnets alternating with six V-shaped spacers, which are highly permeable, high saturation, magnet iron (Figure 5-1 e).

e) ***Array of Hall-Effect Sensors:*** An array of 15 Hall-effect sensors to measure the magnitude of the magnetic flux is used (Figure 5-1 b).

f) ***Sensor Electronics and Signal Conditioning Board:*** This board drives the Hall-effect sensors and converts the signal into voltages that can be recorded by the data acquisition system (Figure 5-1 d).

g) ***Data Acquisition System:*** A data acquisition system is used to collect and store measured data (Figure 5-1 f).
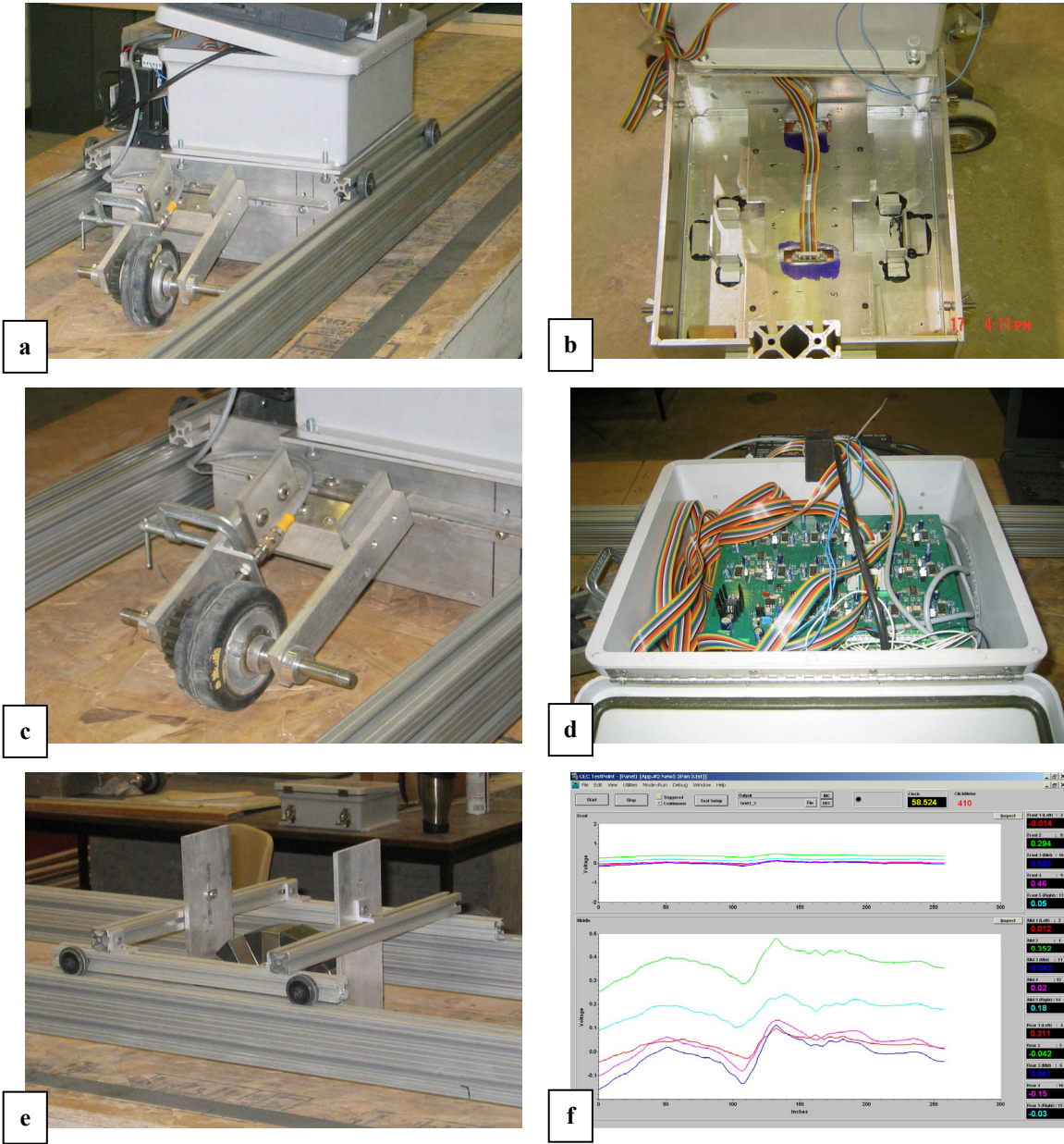
Figure 5-1: All the parts of the MFL device

5.3   Test Setup

From previous tests, it has been noted that there is no difference between results obtained using either plywood or concrete specimens. With that in mind, the decision was made to build a wooden frame covered with plywood sheets to create a horizontal surface. The frame kept all elements -- such as ducts, transverse rebars, longitudinal rebars and strands -- in place during the tests. A total of seven ducts were considered. The corroded region at strands was simulated by leaving a gap in the strands. This gap was created by using non-continuous strands.

Table 5-1 shows all the test setup configurations. In the table, the column "Full" represents the number of continuous strands, and columns "Beg" and "End" represent the number of non-continuous strands. For each test, a name was assigned in order to facilitate identification and organize results. Also, two different sensor positions were considered. The low (L) position had only one inch separating the plywood from the sensors and the high (H) position had a three inch distance separating the sensor from the plywood surface.

Most tests were carried out on lane #1 and lane #2. Lane #1 was considered a baseline since no other duct, transverse rebar or longitudinal rebar were present in the vicinity of lane #1. Lane #2 was similar to lane #1, but the longitudinal and transverse rebars were then considered. The top and bottom mats were assembled using reinforcing steel #4 and assuming longitudinal and transversal spacing equal to 10 inches. Some additional rebars were added between lanes #5 through #14 to study the effect of the splice rebars.

Table 5-1: Test setup configuration

Lane	Test	File	Full	Beg	End	Notes
1	A	P1A	-	-	-	Baseline
1	B	P1B	19	-	-	Full no damage
1	C	P1C	9	10	-	End effect (run-off)
1	D	P1D	9	-	10	End effect (run-on)
1	E	P1E	9	10	10	Partial damage
1	F	P1F	-	19	19	Total damage
1	G	P1G	9	-	-	1/2 full no damage
2	A	P2A	-	-	-	Baseline
2	B	P2B	19	-	-	Full no damage
2	C	P2C	9	10	-	End effect (run-off)
2	D	P2D	9	-	10	End effect (run-on)
2	E	P2E	9	10	10	Partial damage
2	F	P2F	-	19	19	Total damage
2	G	P2G	9	-	-	1/2 full no damage
3	A	P3A	-	-	-	Baseline transverse only
4	A	P4A	-	-	-	Baseline over longitudinal and transverse
5	A	P5A	19	-	-	Full no damage + longitudinal
5	B	P5B	-	19	19	Full no damage + longitudinal

Figure 5-2 identifies the location of 15 sensors with respect to the magnet position.

Direction of Travel
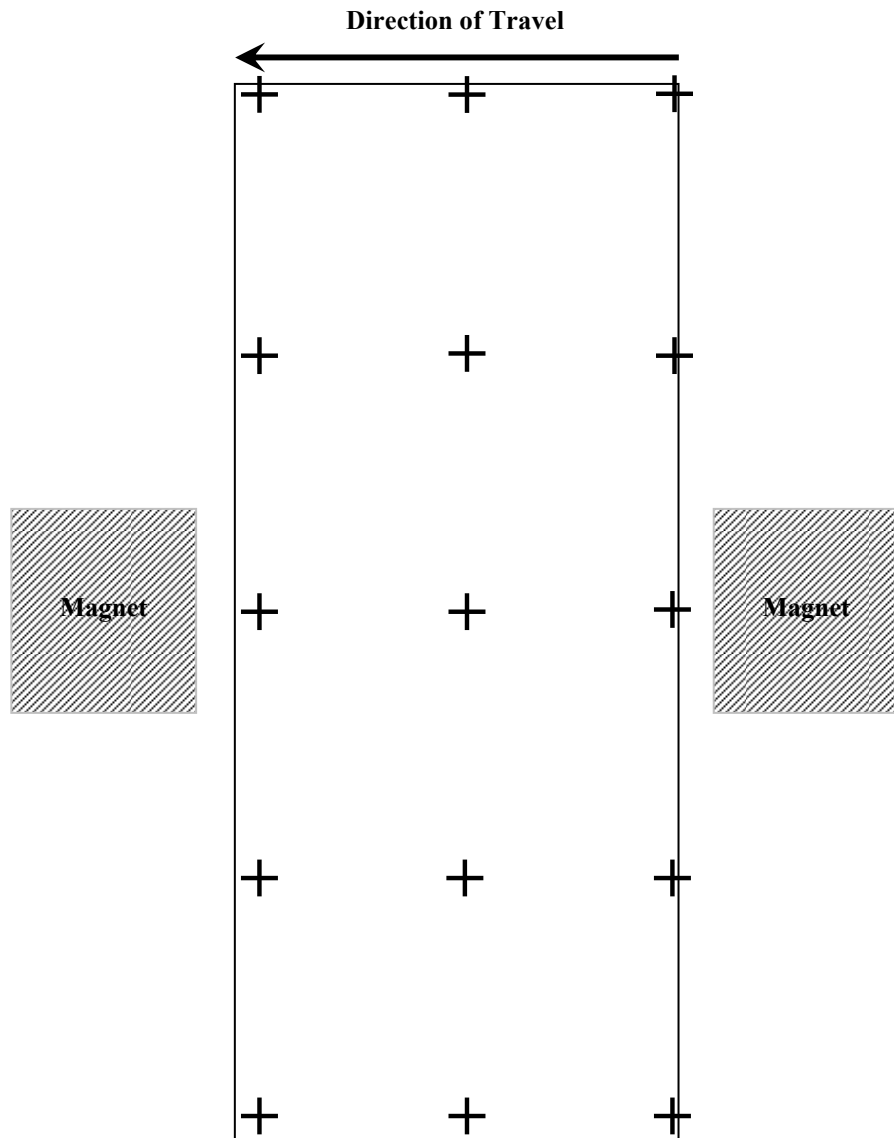
Figure 5-2: Location of sensors

Figure 5-3 shows an overview picture of the wooden frame built in the laboratory. Figure 5-4 shows different snapshots taken from different locations of the frame where details can be seen more closely.

Figure 5-3: Overview of wooden slab

Figure 5-4: Close-up of ducts, strands and reinforcement

5.4 Analysis of Results

Figure 5-5 to Figure 5-18 show the results of the tests carried out. Even though different situations from previous chapters are here considered, similar conclusions can be drawn. Globally, the plots present peak-and-valley disturbance, usually caused by strand ends that allow leakage of magnetic flux. This effect is known as the boundary effect and always can be identified at the beginning and end of each experiment. A secondary peak-and-valley may appear if the strands are discontinuous or corroded. The presence of the flaws alters the normal trend of the measured flux. Locally, minor peak-and–valley disturbances repeated through the whole test length can be observed due to the presence of transverse reinforcements and/or corrugated surface of the duct.

Figure 5-5 and Figure 5-6 show the results from the full duct for low and high positions, respectively. It can be seen that the occurrence of a major peak and valley at the beginning and end of the test are due to the ends of the strands. The minor peaks and valleys, in this case, are due to the corrugated surface of the duct, since no transverse bars are considered in this experiment. The minor peaks and valleys at the low position plot are more well-defined than in the high position case since the distance from the sensor to the duct is smaller.

Figure 5-5: Magnetic flux variation in lane #1 – Test B (low magnet position)

P1B-H
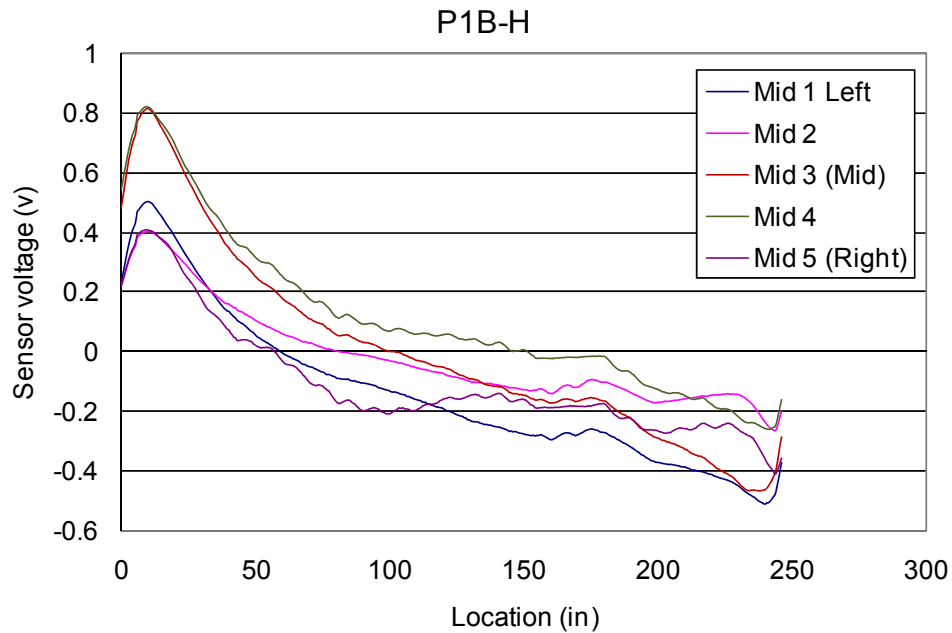
Figure 5-6: Magnetic flux variation in lane #1 – Test B (high magnet position)

If the residual MFL method is considered, the presence of a residual magnetic field can be noted. To avoid this phenomenon, it is recommended that multiple passages of the magnet be carried out so that the steel reaches the magnetic saturation point.

Figure 5-7 through Figure 5-10 show the aforementioned phenomenon when only the duct was tested. It can be seen that in the middle, where the gap was previously located, an unusual response in measured magnetic field is shown in the plots.

This phenomenon does not appear if the active MFL method is considered, since the magnet is present during the entire duration of the experiment.

Figure 5-7: Magnetic flux variation in lane #1 – Test E (low magnet position)

Figure 5-8: Magnetic flux variation in lane #1 – Test E (high magnet position)
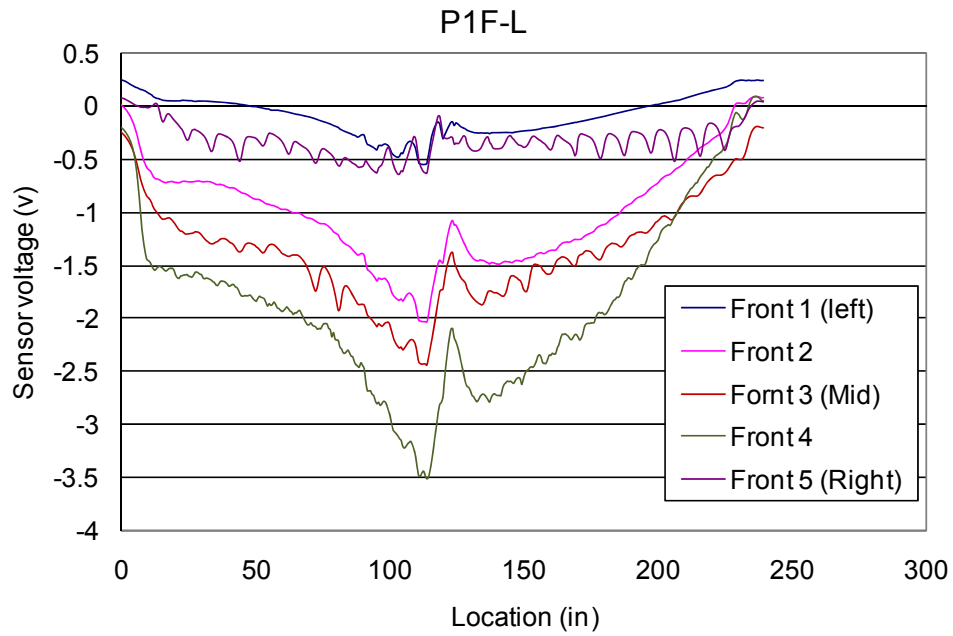
Figure 5-9: Magnetic flux variation in lane #1 – Test F (low magnet position)
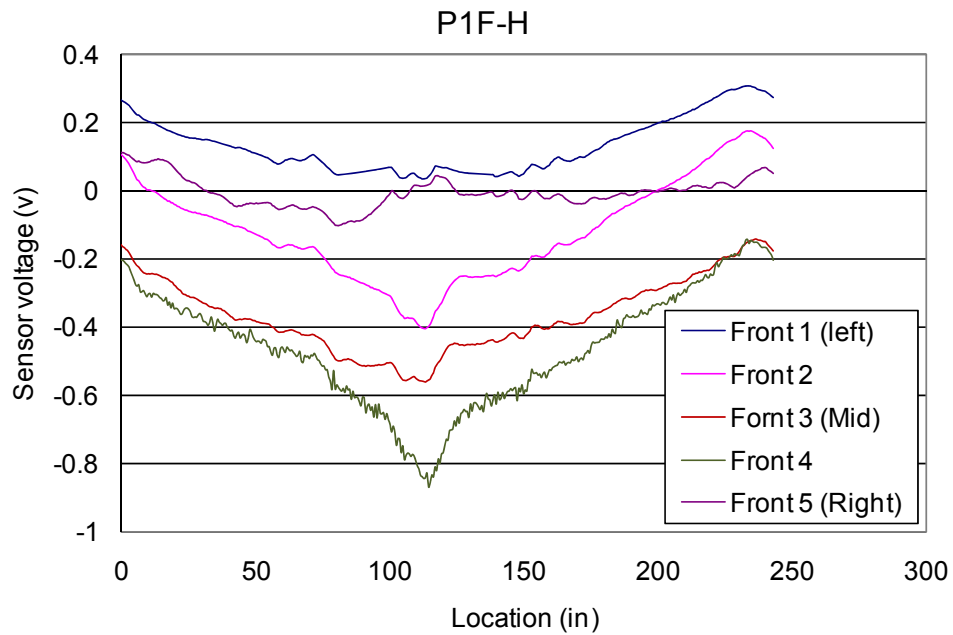
Figure 5-10: Magnetic flux variation in lane #1 – Test F (high magnet position)

Figure 5-11 through Figure 5-14 show test results obtained in lane #2. The only difference between lane #2 and lane #1 is the presence of transverse rebars in lane #2.

It can be seen in Figure 5-11 and Figure 5-12 that the presence of transverse rebars affects magnetic flux by creating equal and repeated peaks and valleys along the curve. The distance between each two peaks or two valleys is the same as the distance between each two transverse rebars. In the case in which the magnet is close to the steel (low position), higher magnetic field disturbance is expected.
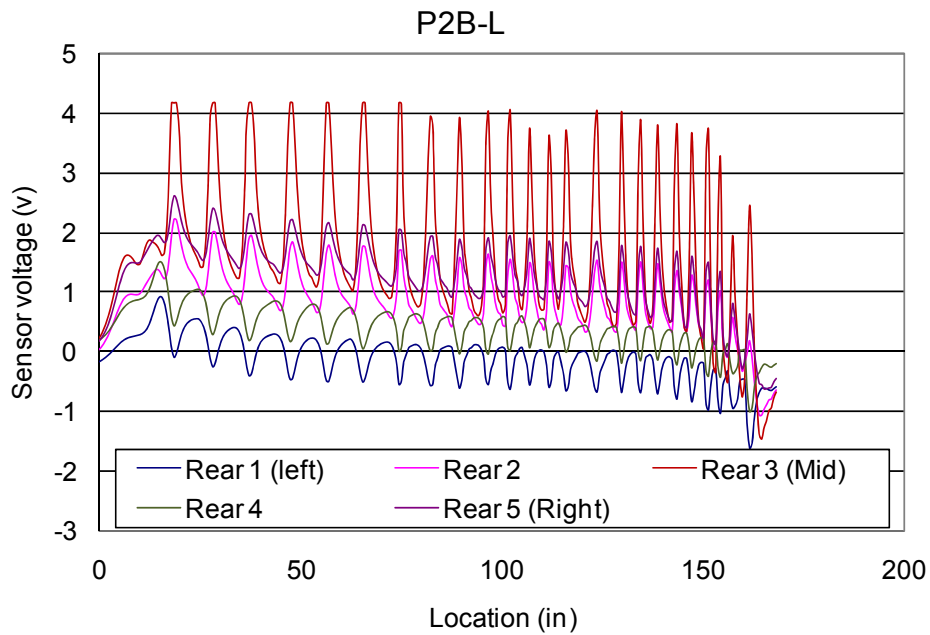
Figure 5-11: Magnetic flux variation in lane #2 – Test B (low magnet position)
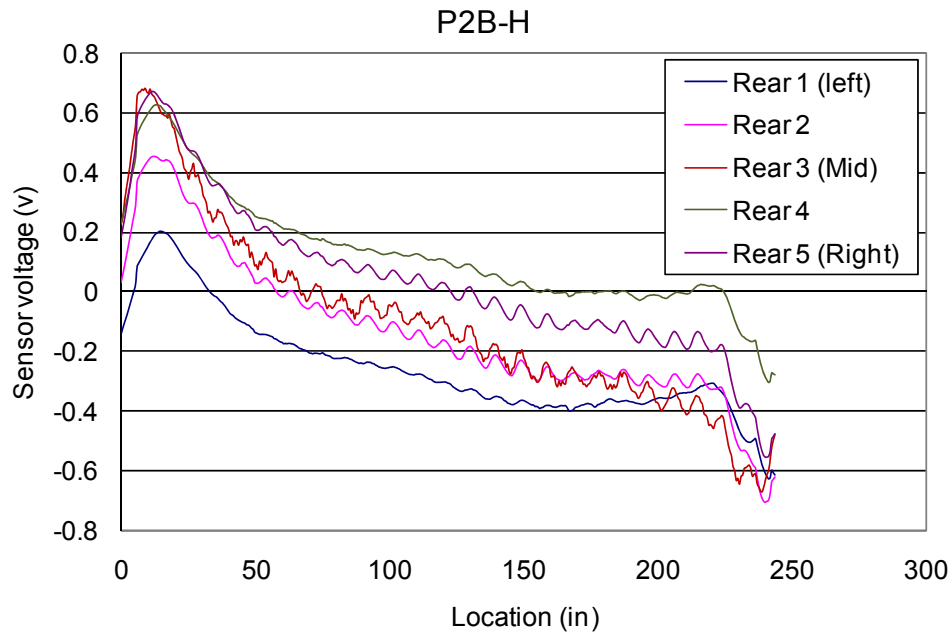
Figure 5-12: Magnetic flux variation in lane #2 – Test B (high magnet position)

Figure 5-13 and Figure 5-14 show the same trends that were observed in previous tests. However, it can be seen that the electrical potential suffers a reduction at 100 inches and then an increase at around 120 inches. This behavior is due to the presence of the gap.
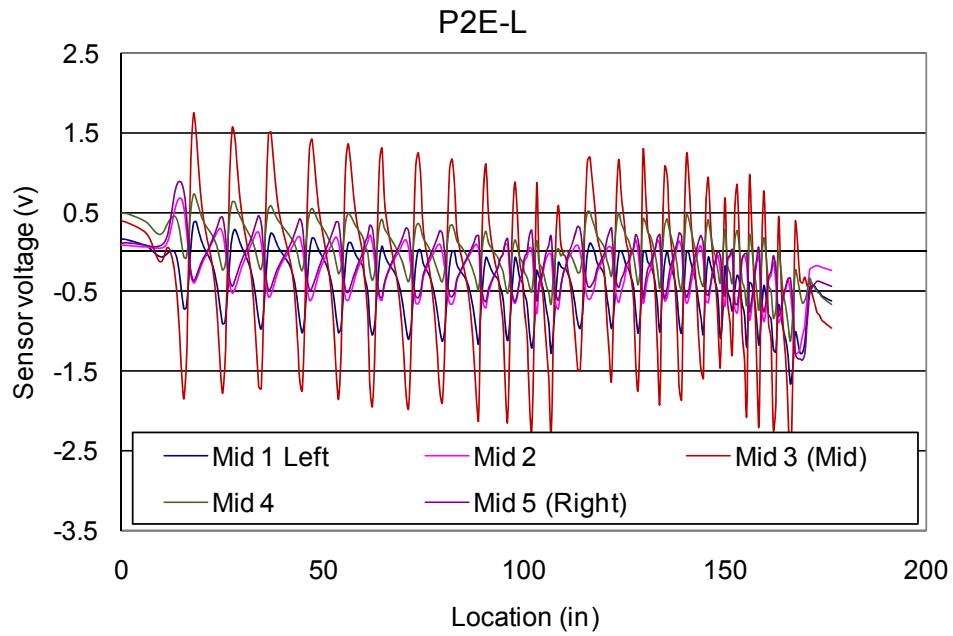
Figure 5-13: Magnetic flux variation in lane #2 – Test E (low magnet position)

Figure 5-14: Magnetic flux variation in lane #2 – Test E (high magnet position)

Figure 5-15 and Figure 5-16 show the results obtained on lane #3, which only considers transverse rebars. The same trend observed in previous tests is noticed here. Equally and repeatedly, peaks and valleys along the curve are observed. The distance between each two peaks or two valleys corresponds with the distance between each two transverse rebars. Once again, the magnitude measured considering the low position has higher disturbance than the sensor at high position.
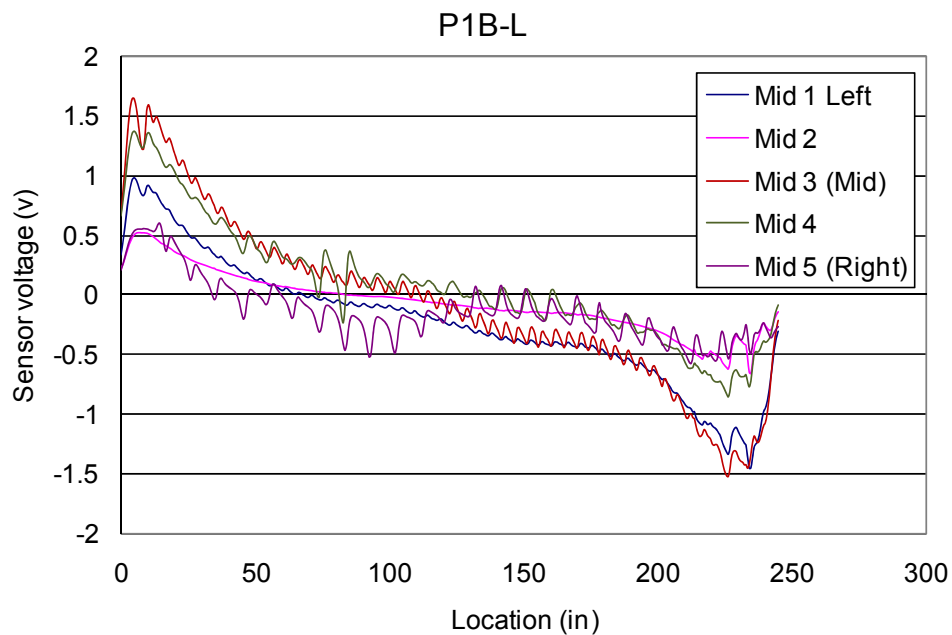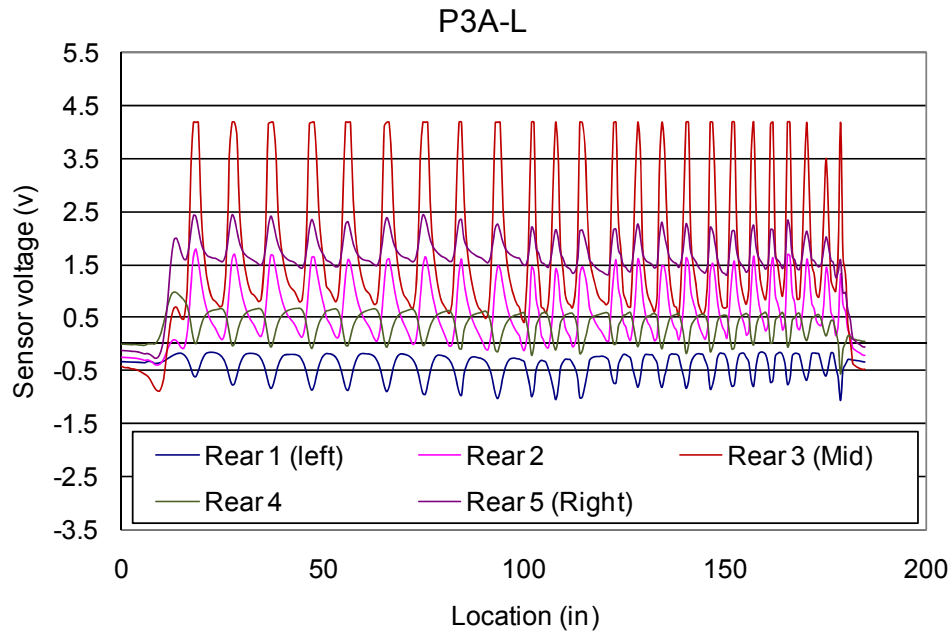

Figure 5-15: Magnetic flux variation in lane #3 – Test A (low magnet position)
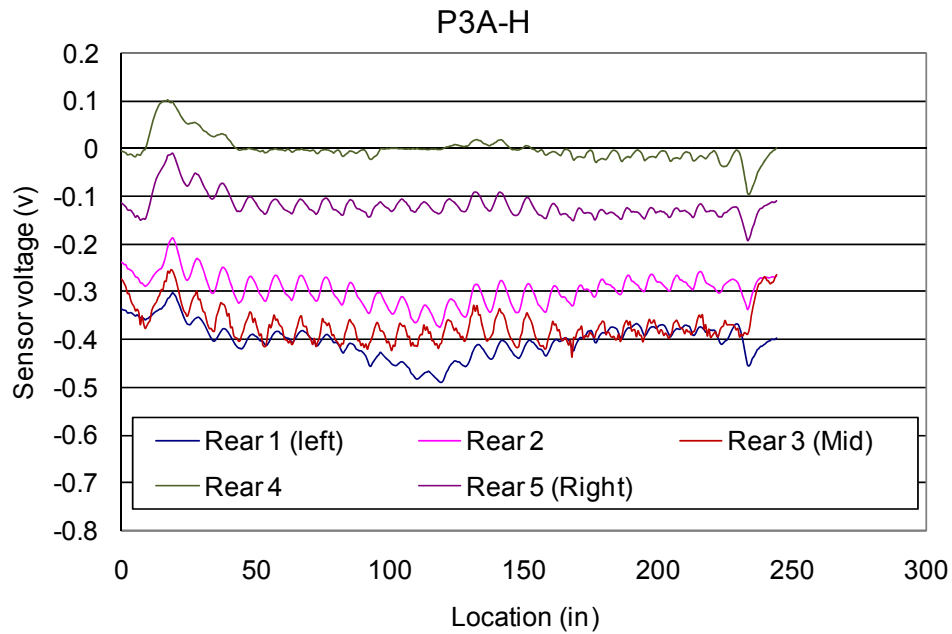
Figure 5-16: Magnetic flux variation in lane #3 – Test A (high magnet position)

Figure 5-17 and Figure 5-18 show the results of the test in lane #4. It can be noted that the behavior of the curves is the same as in lane #3. The presence of longitudinal bar did not affect the normal trend of the signal. No major changes in the signal could be found. The only uncertainty that longitudinal reinforcement would add to the experiment results is whether or not corrosion is located at the longitudinal bar or at the strands, since longitudinal reinforcements are usually parallel to the strands and also closer to the surface.
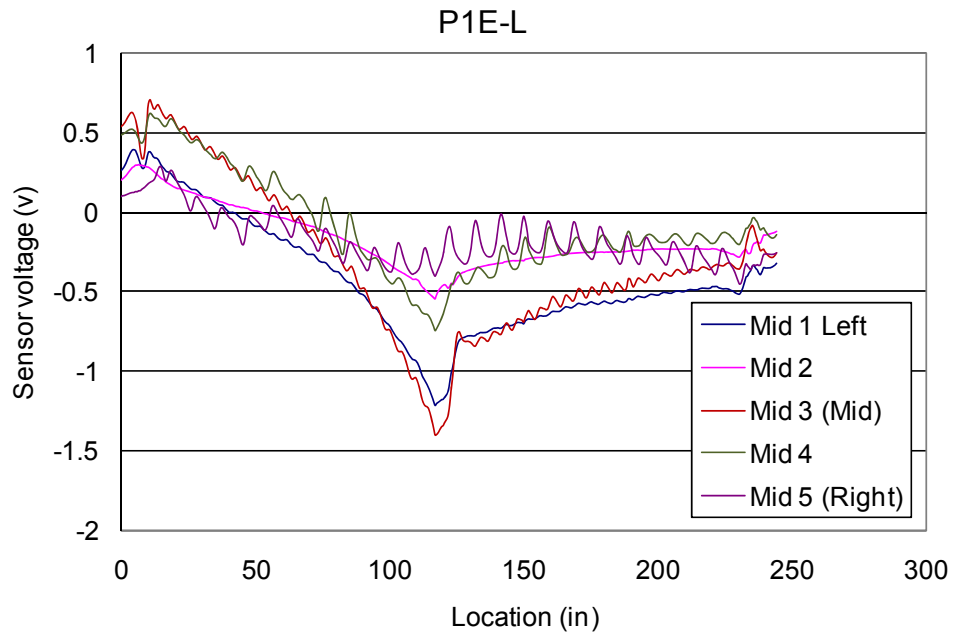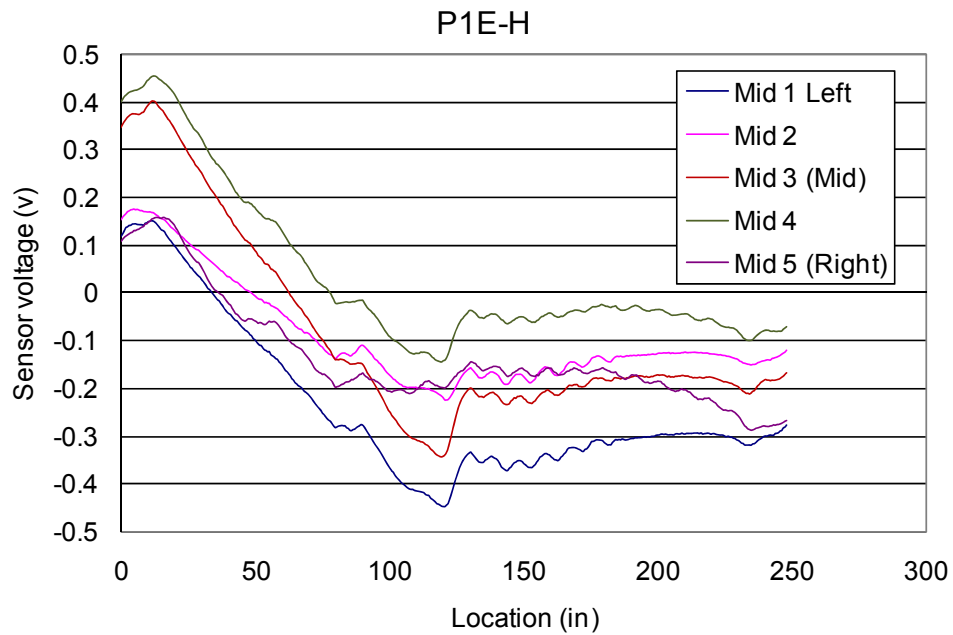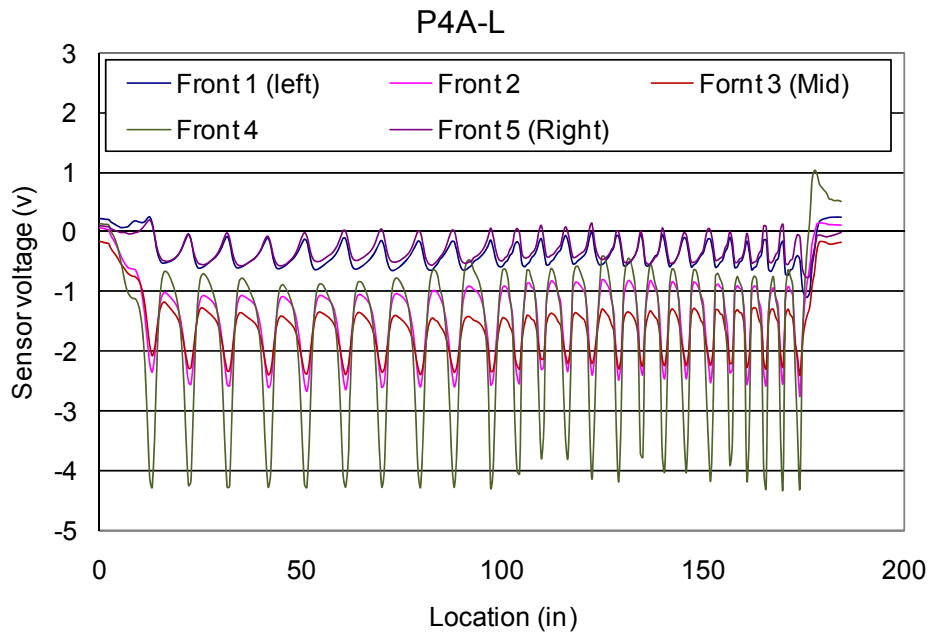
Figure 5-17: Magnetic flux variation in lane #4 – Test A (low magnet position)
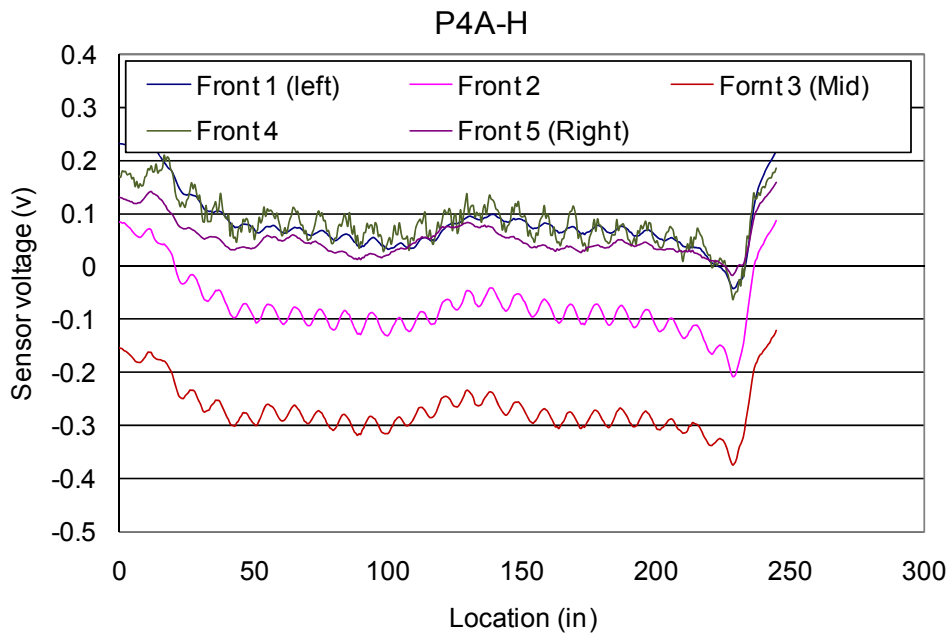
Figure 5-18: Magnetic flux variation in lane #4 – Test A (high magnet position)
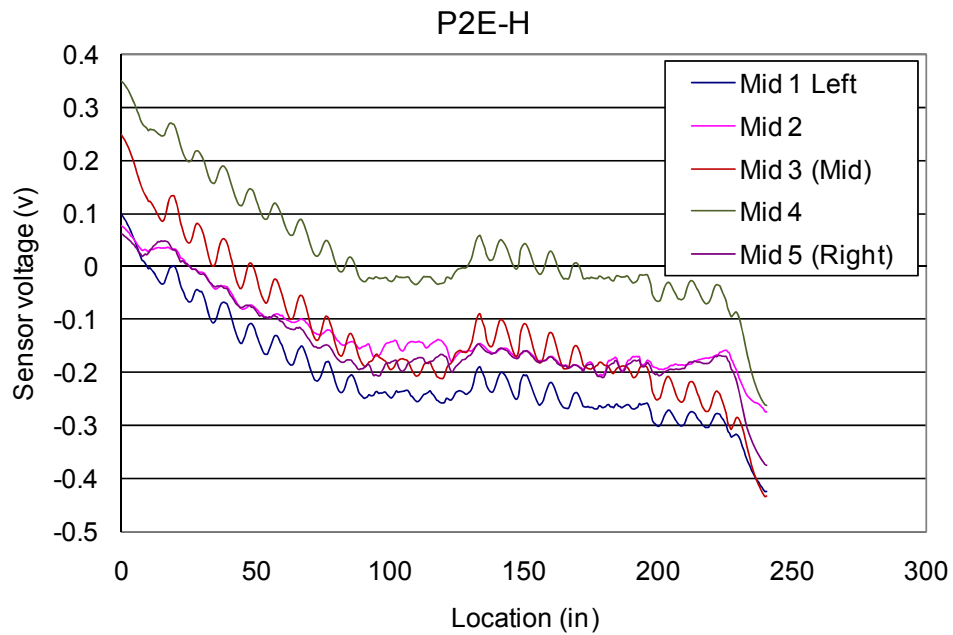
Figure 5-19 and Figure 5-20 show the results organized into a 3D surface plot. The major and minor peaks and valleys on those plots can be seen.
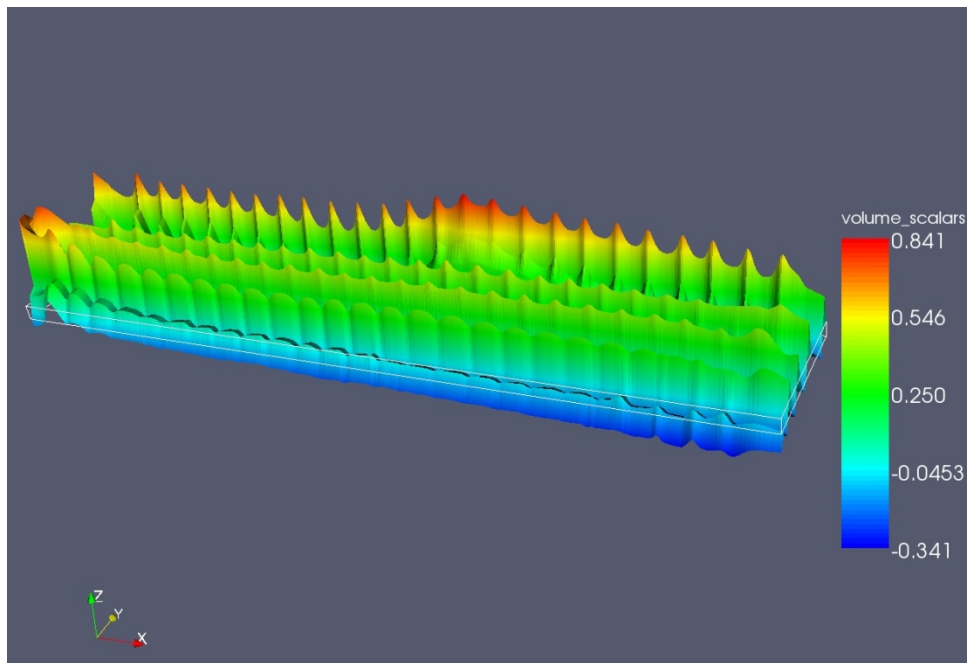
Figure 5-19: 3D view of the deck with a gap at only one of the ducts
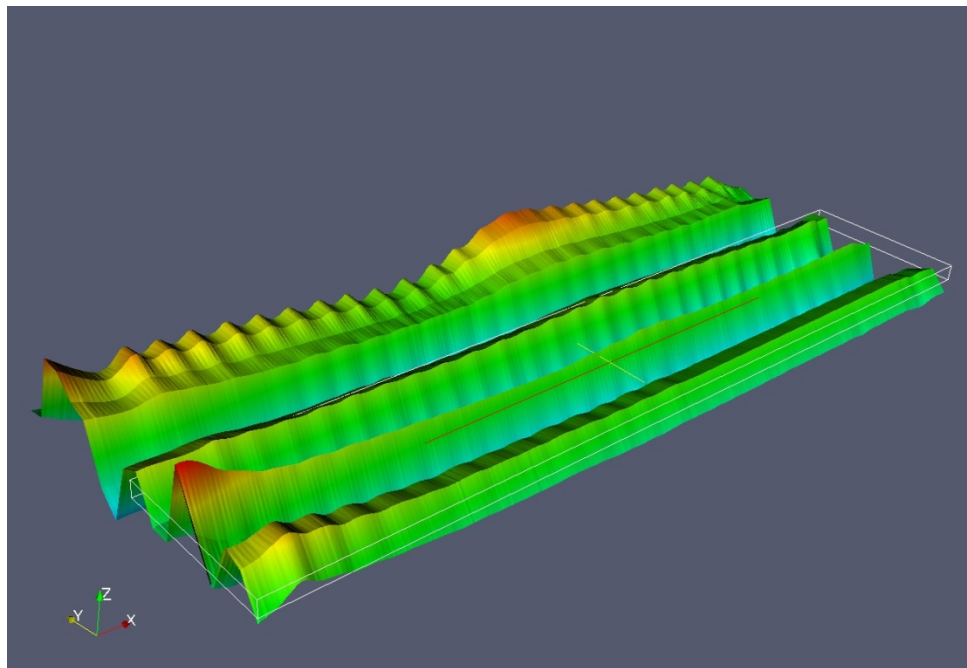
Figure 5-20: 3D view of the wood slab with a gap at only one of the ducts

5.5   Conclusion

It can be concluded that peak-and-valley disturbance can be created by gap and/or by the ends of the strands. Transverse rebars affect the magnetic field locally by creating repeated peak-and-valley disturbances.   However, those disturbances are considered minor and do not affect the global behavior of the measured magnetic field. Minor peak-and-valley disturbance can also be due to the bents present on the corrugated duct. Longitudinal reinforcement does not affect the measured magnetic field.

Corrosion, here simulated by leaving a gap, can be localized by finding the middle point between the main peak and valley.

The phenomenon of residual magnetic can be observed if the experiment is carried out assuming the residual MFL method. This test method is conducted without the presence of the magnet; consequently, the residual magnetic already present in the duct, strands and/or the longitudinal bar will influence the results. To avoid undesirable and unexpected results, it is recommended that multiple passages of the magnet be performed, so that the ferromagnetic elements reach the saturation point, eliminating undesirable results.

All the tests carried out and presented in Chapters 2, 4 and 5 simulate corroded strands by physically cutting the strand or rebars. The question remaining was whether the break in the strand adequately simulates corrosion.

Consequently, it was decided to use corroded strands and to carry out some additional tests to verify the validity of the conclusions reported in previous chapters.

Chapter 6

MFL Tests Using Corroded Strand

6.1 Introduction

Tests using corroded strands were performed to evaluate the validity of using discontinuous strands to simulate corrosion. This chapter summarizes and discusses the results obtained using corroded strands.

6.2 Test Setup

Figure 6-1 shows the MFL device and Figure 6-2 shows the board which contains the 15 Hall-effect sensors. Two different setups were considered with six different test configurations. The first test setup considers discontinuous strand to simulate the corrosion. Additional (non-corroded) strands were later added to change the percentage of section loss, which varied from 0% (no loss) up to 50% of section loss. Setup number two considers corroded strands which were obtained by using the electrolysis method.

The test setup and results obtained by applying electrolysis to accelerate the corrosion are further explained here. The results from tests carried out are also discussed. All tests presented here are based on the residual MFL method.
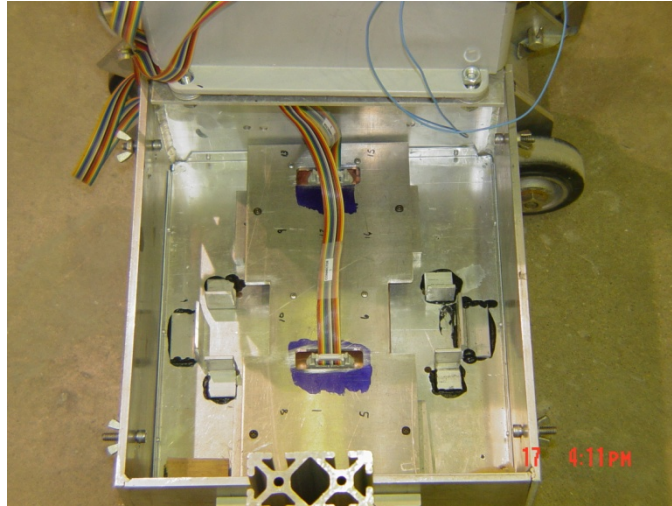
Figure 6-1: MFL device equipped with 15 Hall-effect sensors
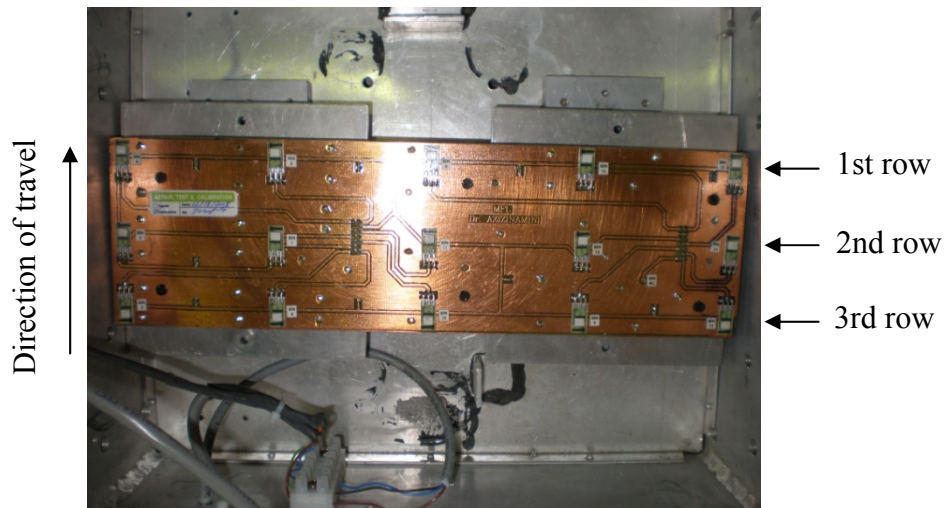
Figure 6-2: Board with 15 Hall- effect sensors

Error! Reference source not found. show the different testing conditions here considered. These testing configurations were assumed to better understand the influence of the number of strands and also to compare the results between corroded and discontinuous strands. The distance from the top of the wood plate to the bottom of the Hall-effect sensor board was three inches.

Figure 6-3 through Figure 6-5 show drawings of the test specimen considered in this chapter.
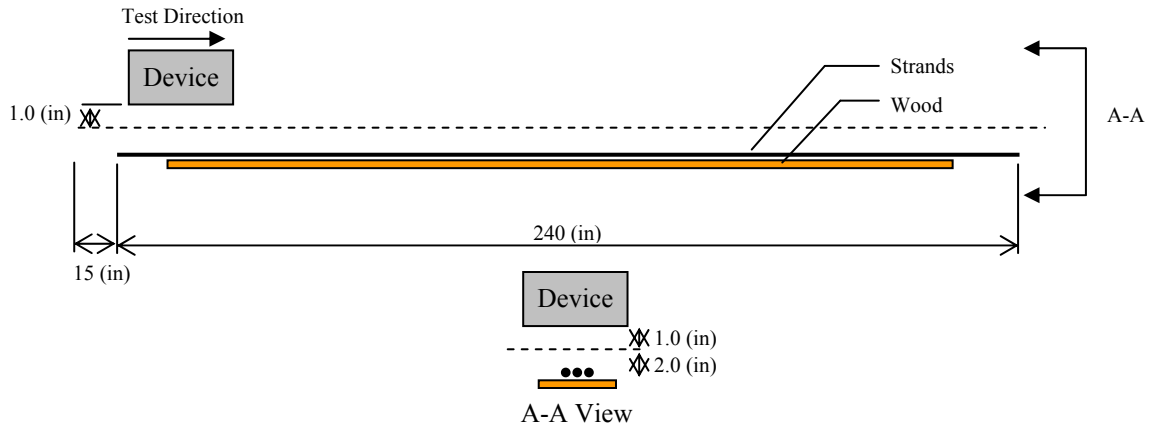
Figure 6-3: Continuous strand experiment setup (baseline)
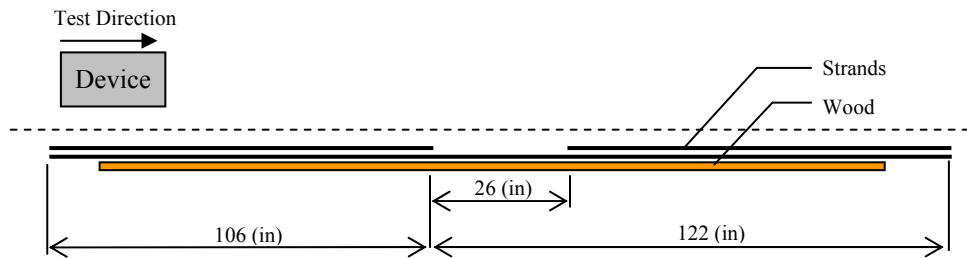
Figure 6-4: Discontinuous strands experiment setup
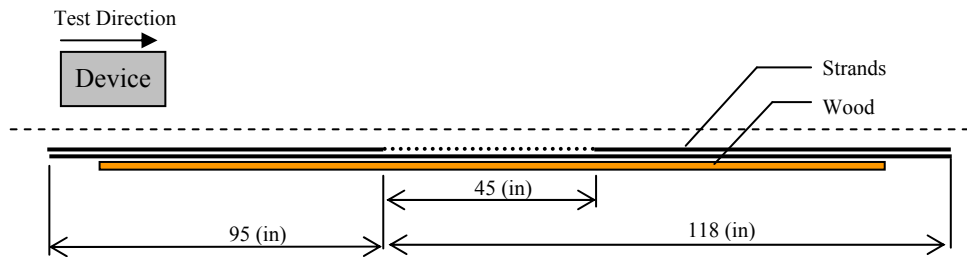
Figure 6-5: Corroded strands experiment setup

In order to assure the accuracy of field-inspection-based conclusions, the test configurations mentioned in Table 6-1 were conducted, analyzed and discussed regarding the presence of corrosion on the strands.

Table 6-1: Different test conditions

Setup	Test	File	Arrangement (A-A View)	Strands Continuous / Non-Corroded	Discontinuous	Corroded	Notes
1	A	P1A	●	1	-	-	Baseline
1	B	P1B	●●	1	1	-	50% section loss
1	C	P1C	●●	2	1	-	33% section loss
1	D	P1D	●●●●	3	1	-	25% section loss
1	E	P1E	●●●●●	4	1	-	20% section loss
1	F	P1F	●●●●●●	5	1	-	17% section loss
2	A	P2A	●	1	-	-	Baseline
2	B	P2B	●●	1	-	1	25% section loss
2	C	P2C	●●●	2	-	1	16% section loss
2	D	P2D	●●●●	3	-	1	12% section loss
2	E	P2E	●●●●●	4	-	1	10% section loss
2	F	P2F	●●●●●●	5	-	1	8% section loss
2	EE	P2EE	●●●●●	4	-	1	10% section loss
2	FF	P2FF	●●●●●●	5	-	1	8% section loss

Legend: ● represents non-corroded strand   ● represents either discontinuous or corroded strands

Note: EE and FF were additional tests, where the strands were rearranged.

6.3 Analysis of Results

Setup 1/Test A was considered as a baseline since no corrosion or discontinuity in the strand was present. Therefore, all the following analyses are based on this experiment result.

Figure 6-6 shows the plot of electrical potential (V) versus the distance (in.) from all 15 sensors. They were grouped into three groups of five sensors. Different tones of colors were assigned so it would be easier to identify either the group or sensors on the plots. The orange lines represent the first row of five sensors, green lines represent the second row of five sensors and finally, the blue lines represent the last five sensors. Each row has five sensors which are called left (L), mid-left (ML), middle (M), mid-right (MR) and right (R).
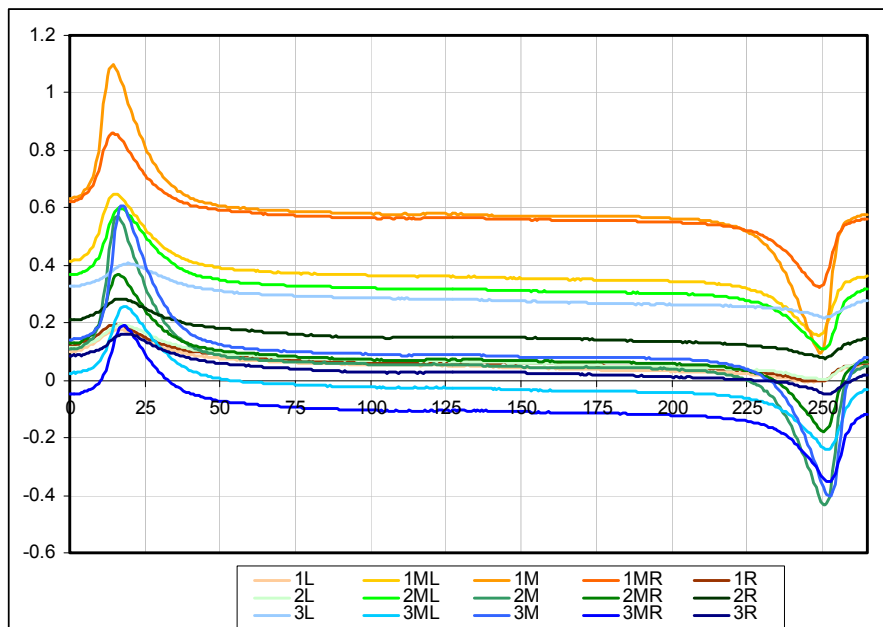
Figure 6-6: 15 sensors, results from Setup 1/Test A

The first step is to study the graphs to understand the 15 sensor responses. Two different approaches were considered: (1) the data from sensors longitudinal and (2) transversal to the direction of running.

6.3.1 Longitudinal Sensor Analysis

Based on the response from the sensors parallel to the running direction, it was possible to determine the distance which separates each sensor. However, due to the test configuration, no other information could be extracted.

From Figure 6-6, one can see that each sensor has a different potential. However, if a specific row of sensors are considered, it can be noted that the magnitude remains constant.

Figure 6-7 shows the plot of electrical potential (V) versus distance (in.) from all three middle sensors (1M, 2M, 3M). For better analysis, the results were linearly translated so the electrical potential at the starting point for the three sensors was equal to zero.
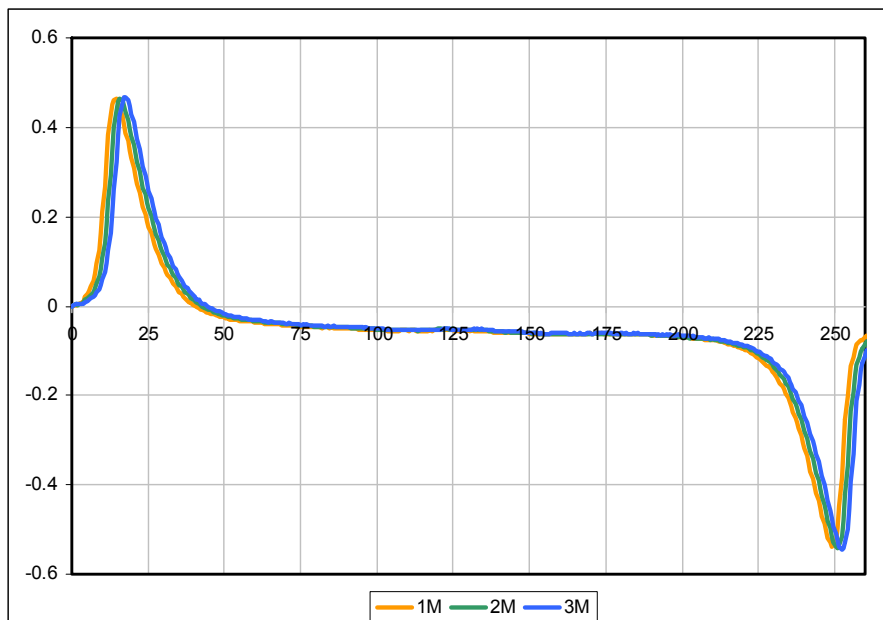
Figure 6-7: Three longitudinal sensor results from Setup 1/Test A after the linear translation

From Figure 6-7, it can be concluded that the only difference from the plot is a slight lag from each sensor's response. This lag is merely the distance which separates each sensor.

Figure 6-8 shows in detail the peak located between 13 and 19 inches. Auxiliary lines were drawn to better determine the distance from each sensor. In Figure 6-8, the distance between sensors is equal to 1.6 inches.
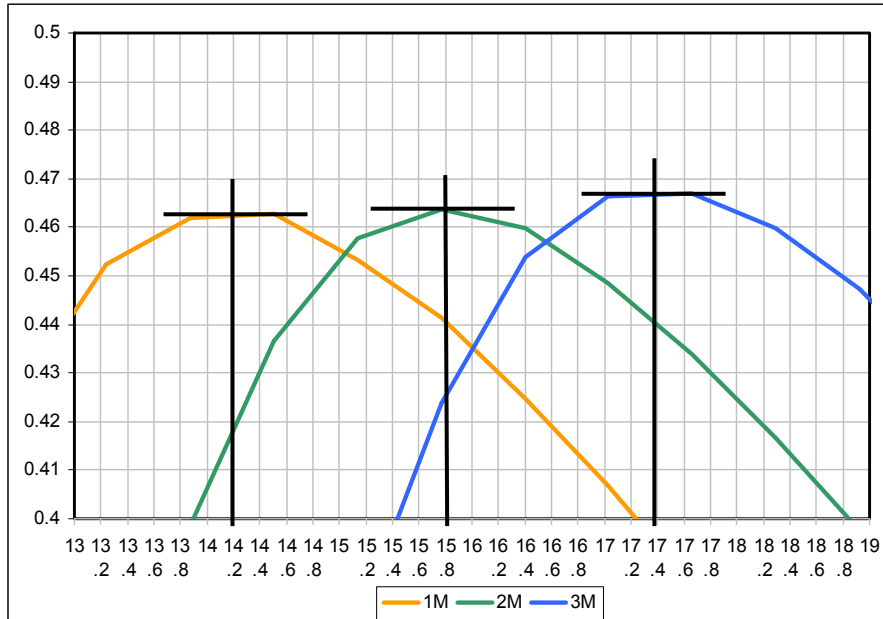
Figure 6-8: Peak located between 13 and 19 inches at Test A/Setup 1

Figure 6-9 shows in detail the measurement taken between sensors. It can be seen that the distance between sensors is 1 5/8 inches (1.625 inches), which matches precisely with the experimental results.
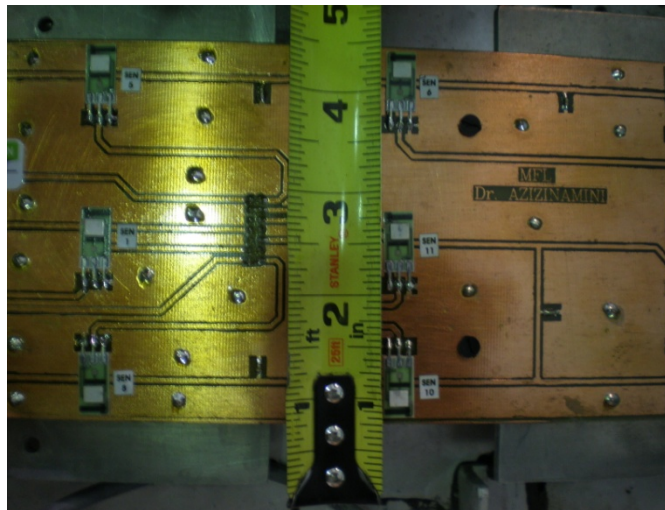
Figure 6-9: Measurement of longitudinal distance between sensors

6.3.2 Transverse Sensor Analysis

Based on responses from the sensors transversally arranged to the experiment running direction, it is possible to measure the electrical potential transversally to the strands. Such information is very valuable in determining the precise location of transversal rebars, for example.

Plots such as 3D surface and contour plots can be drawn from those data. Those plots are very useful and make it much easier to study and understand the results obtained by the experiments.

The spacing between sensors measured transversally is equal to three inches. Figure 6-10 shows the measurement.
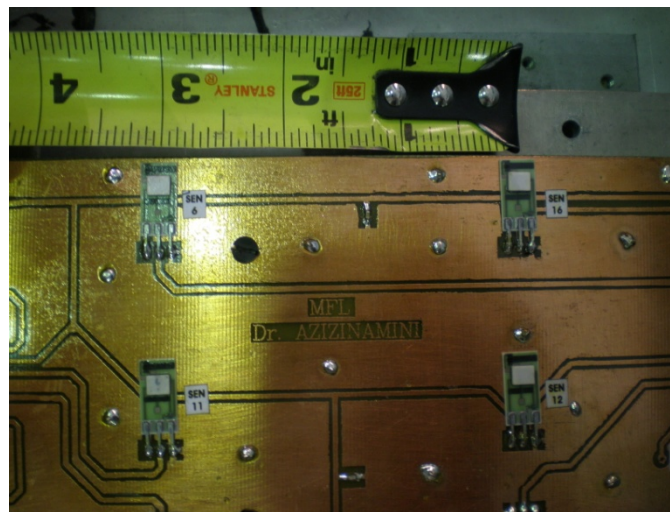
Figure 6-10: Measurement of transverse distance between sensors

Figure 6-11 shows the plot of electrical potential (V) versus the distance (in.) from all five sensors (2L, 2ML, 2M, 2MR, 2R) located in the second row. Since the electrical potentials are different for each sensor, results were then organized so that the electrical potential at the starting point for all five sensors assumes the value zero. From Figure 6-9, it is easily noted that sensor 2M had the highest potential, followed by sensors 2ML and 2MR and further by sensors 2L and 2R. Such result was already expected, since sensor 2M is the closest to the strands and is also located right on top of the strand.
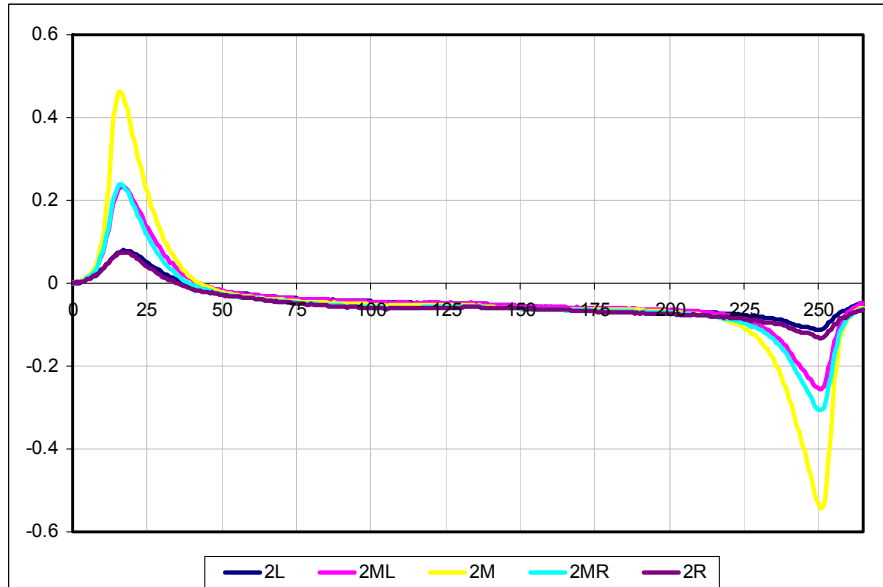
Figure 6-11: Five transverse sensors, results from Setup 1/ Test A after linear translation

As noticed, the electrical potential is very steady between 50 to 225 inches, since no flaws are present on this test. On the other hand, the potential changes when approximate to strand ends because of magnetic flux that leaks at the boundaries.

6.4   Electrolysis Experiment

The literature shows that electrolysis is the most efficient and fastest method to move electrons from one metal to the other. Such migration causes corrosion. With this in mind, electrolysis was used to obtain short term corrosion in the laboratory.

6.4.1 Overview

Electrolysis involves the passage of an electric current through an ionic substance that is either molten or dissolved in a solvent, resulting in chemical reactions at the electrodes.

In a cell, the anode is positive and the cathode is negative. To be useful for electrolysis, the electrodes need to be able to conduct electricity. An ionic compound (e.g. NaCl) reacts with the solvent to produce ions (such as an acid). The compound is dissolved in an appropriate solvent (e.g. H_2O) resulting in a liquid full of free ions. An

electrical potential is applied between a pair of electrodes immersed in the liquid, where each electrode attracts ions that are of the opposite charge. Therefore, positively-charged ions (called cations) move towards the electron-emitting (negative) cathode, whereas negatively-charged ions (termed anions) move toward the positive anode. The energy required to separate the ions and to gather them at the respective electrodes, is provided by an electrical power supply.

6.4.2 Methodology

Figure 6-12 shows the wood box with an exhaust system. The box's dimensions are 45 in. long x 27 in. wide x 12 in. of height. An exhaust system was installed to remove the gases formed by the chemical reaction.

Twelve strands (anodes) where connected to each other using a splicer and were then connected to the positive pole of the power supply. At the bottom of the box were placed several rebars (cathodes) which were connected to the negative pole. To keep the corroded material in place, all strands were enclosed with fine plastic net.

Water was added into the box until submerging the strands and then 50 lb. of salt was added to create an ionic solution that was electrically highly conductible.

Figure 6-12: Timber box used for the electrolysis experiment

Calculation of molar concentration: 50 lb or 22679.5 grams of NaCl dissolved in 45x27x12 = 14580 in^3 or 235.09 L of water (since 58 grams of NaCl is 1 mole).

The molarity of the solution is (22679.5/58 mol)/(235.09 L) = 1.66 molar.

Figure 6-13 shows the Sorensen® DCS8-125E power supply which was used in the experiment. This power supply is capable of providing 0-8 volts and 0-125 amperes of direct current.

Figure 6-13: Sorensen® DCS8-125E power supply

A current of 120 amperes was applied to 12 strands for six hours per day. After four days of experimentation, the section loss was close to 50% and the experiment was then concluded. Before restarting and after each day of experimentation, a visual inspection of strands was conducted to determine the progress of corrosion and to decide whether the experiment should be ended or continued.

Figure 6-14 shows the condition, after drainage of remaining liquid, of one strand taken as a sample and of the box and rebar at its bottom after four days of experimentation. It can be seen that a highly corrosive environment was created.

Figure 6-14: Final result after four days of electrolysis

6.4.3 Analysis of Electrolysis Results

Figure 6-15 (a) through (d) show the corrosion products in detail after electrolysis. The total length of corrosion was 45 in. (the box's length).

(a): Strand after corrosion

(b): Detail of rust/corrosion product

(c): Plastic net used to hold the corrosion product in place

(d): Detail of cross section loss

Figure 6-15: Corroded strand in detail after electrolysis

Figure 6-16 (a) and (b) show two different measurements taken at the non-corroded section (a) and another at the corroded section (b).
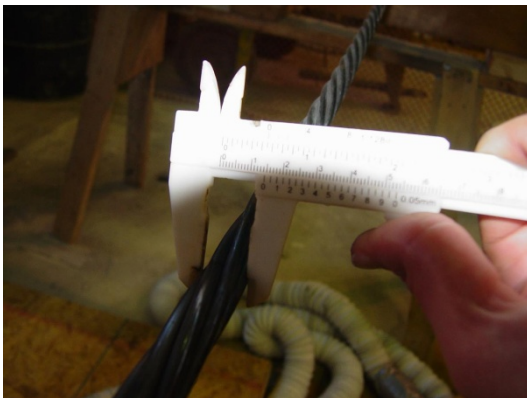
(a): 1.44 cm of diameter at non-corroded region

(b): 0.99 cm of diameter at corroded region

Figure 6-16: Strand measurement at different locations

It is very difficult to obtain the exact diameter of the strand since they are made with seven twisted cables. Table 6-2 shows two different measurements taken based on two considered orientations. A loss of 65% was achieved after four days of electrolysis, which correspond to 46% total loss of cross section.

Table 6-2: Diameter measurements comparison

Measurements Orientation	No Corrosion (cm)	Corroded (cm)	Percentage (%)
⬍	1.55	1.02	65.8 %
↔	1.45	0.95	65.5 %
Area (cm^2)	1.767	0.817	46.2%

6.5 Discontinuous Strands Experiment Results

At first, discontinuous strands were used to simulate the loss of section in the laboratory. An initial test was conducted where no discontinuity was present. This test was considered to be the baseline for further comparison. After obtaining the baseline, two pieces of strands were added at both ends so that approximately in the middle, a gap of 26 inches was formed. Gradually, the number of non-corroded (continuous) strands was increased until there was a total of five non-corroded strands.

Figure 6-17 shows the results plotted from all six experiments. Because of the test setup and also for ease in comparing results, only the electrical potential measured by sensor 2M was plotted here. The legend is based on **Error! Reference source not found.**, previously described in this chapter.

The main conclusions based on Figure 6-17 are:

- If all strands were continuous, the electrical potential would have the same behavior of Setup 1/ Test A.
- The only effect caused by increasing the number of stands was observed only at the ends (the boundary effect).
- The peak and valley formed between 120 to 145 inches was caused by the discontinuous strand.
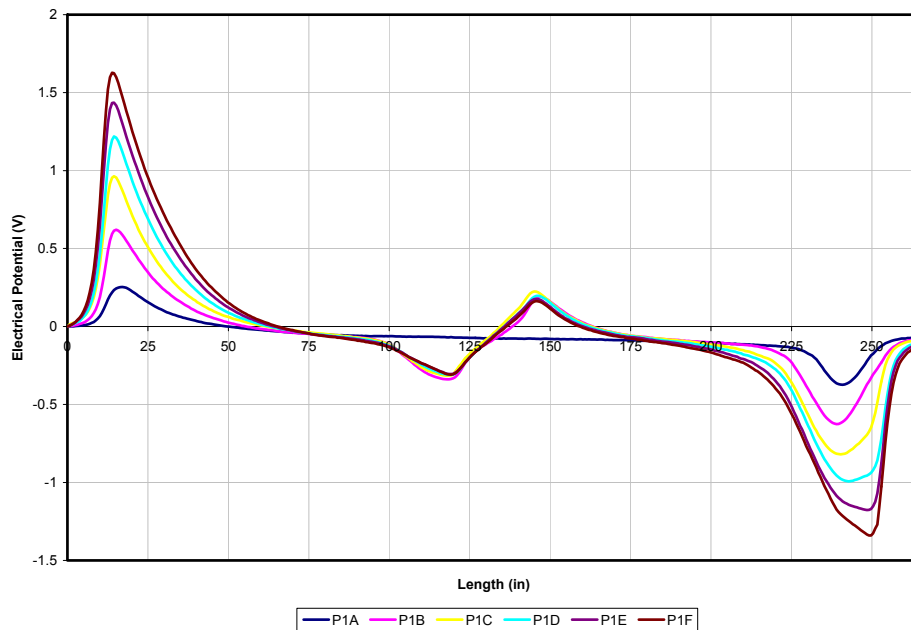- The peak-to-peak amplitude is proportional to the section loss.

Figure 6-17: Test results from Setup 1/ Test A thru F

The strands were arranged such that at the beginning all strands were lined up. Since some of them were not of equal length -- 19 ft. (228 in.) -- a non-uniform response was expected at the end of the experiment, which can be observed in Figure 6-11 between 225 to 250 inches.

Analyzing, it can be seen in Figure 6-17 that the amplitude of the blue line, between 0 to 50 inches, is approximately 0.25V, matching the potential measured at distance 120 in., where the difference is -0.31V – (-0.065V) = -0.245V, proving the proportionality of magnetic flux with the amount of section lost.

6.6 Corroded Strands Experiment Results

A similar approach to the discontinuous experiment was taken so further evaluation between both results could be easily made. An initial test was conducted where no corrosion was present. This test was considered to be the baseline for further comparison. After obtaining the baseline, one corroded strand was added where a corroded region of 45 inches was present. Gradually, the number of non-corroded strands was increased until a total of five non-corroded strands were reached.

Figure 6-18 shows the results plotted from all six experiments. Because of the test setup and also for ease in comparing results, only the electrical potential measured by sensor 2M was plotted here. The legend was based on Table 6-2, previously described in this chapter. No major difference between the results from discontinuous testing to the corroded test was here observed. The main conclusions based on Figure 6-18 are:

- If all strands were continuous, the electrical potential would have the same behavior of Setup 2/ Test A.

- The only effect caused by increasing the number of strands was observed only at the ends.

- The peak and valley formed between 110 to 155 inches was caused by the corroded strand.

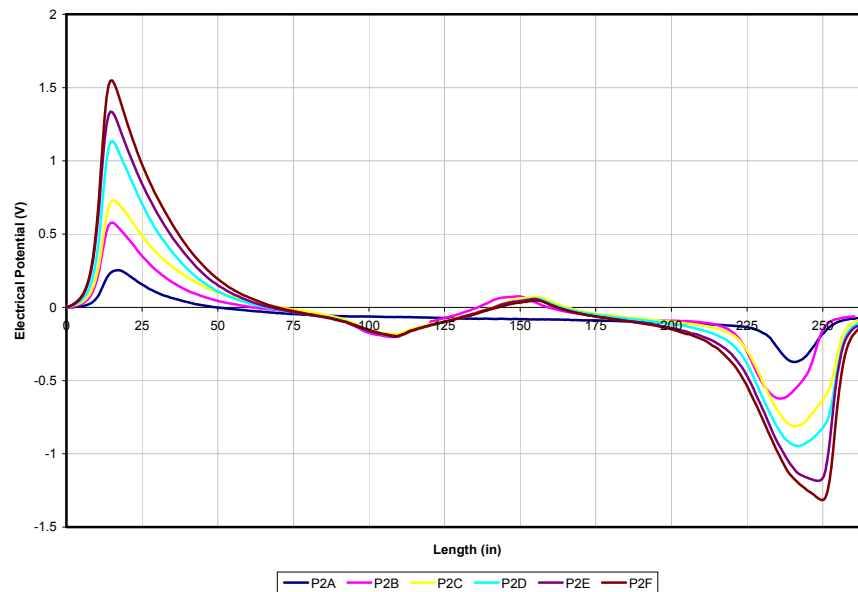- The peak-to-peak amplitude is proportional to the section loss.

Figure 6-18: Test results from Setup 2/ Test A thru F

The strands were arranged such that at the beginning all strands were lined up. Since some of them were not of equal length, 19 ft. (228 in.), a non-uniform response was expected at the end of experiment, which can be observed on Figure 6-11 between 225 to 250 inches.

It was also noticed that Test 2/Setup B (the pink line) had its results shifted to the left. Such effect resulted because the triggering mechanism -- which is responsible for measuring distance -- had missed readings during the experiment.

Analyzing Figure 6-18 more closely, it can be seen that the amplitude of the blue line is approximately 0.25V at 17 inches. This value is approximately double the value measured at 110 inches, where the difference between potential is -0.195V – (-0.065V) = -0.13V. From the plot, one can conclude that 50% of loss implies a 50% of reduction at measured potential.

Table 6-2 pointed out two extra experiments where the only difference was the location of the corroded strand. The objective of those experiments was to observe whether or not the measured electrical potential would suffer any changes if the corroded strand where located at the bottom of a set of strands.

Figure 6-19 shows the results of two additional tests which were performed in the laboratory.
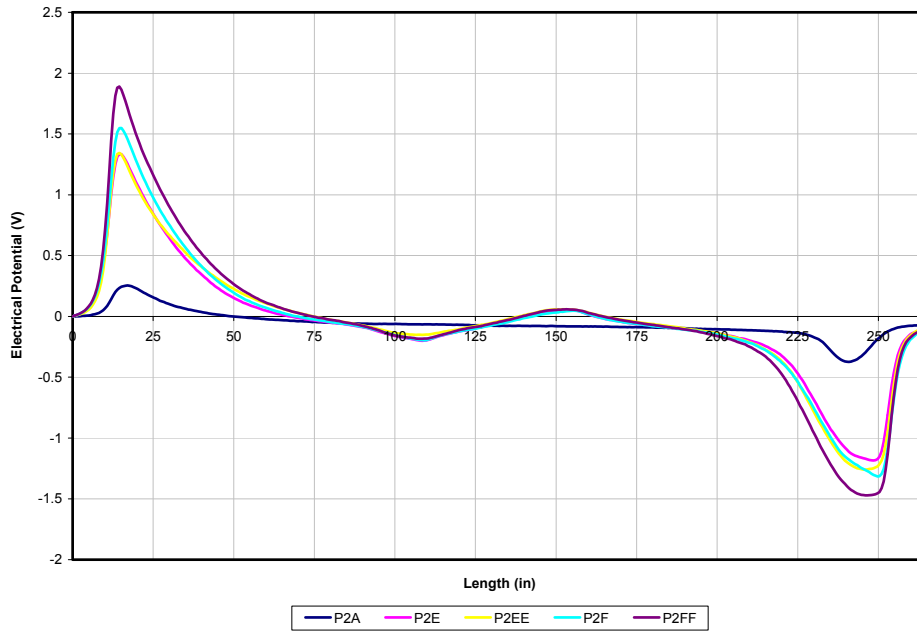

Figure 6-19: Test results from Test 2/Setup EE and FF

Once again, the obtained results follow the same trend. The only difference observed was noticed at the boundaries on Test 2/Setup F and FF. Both had the same number of strands, but the measured potential was different since some strands at Setup

FF were now much closer to the Hall-cell sensors. Such behavior proves the dependency of the electrical potential on the distance that separated the sensor and the metal.

The software MATLAB® 2007 was used to create the plots. The values between sensors where calculated by using a cubic interpolation available in MATLAB.

Figure 6-20 shows respectively the 3D and contour plots from Setup 1/ Test A. The green area in the middle shows – once again – a very steady magnetic field, since no corrosion or discontinuity was present in this experiment. It is easily noticed that the peak and valley formed at the ends. Also, it can be noted that the middle sensor has the highest value and gradually decreases as one approximates to the left or right sensor.

Figure 6-20: 3D plot (left) and contour plot (right) of P1A experiment

Figure 6-21 shows respectively the 3D and contour plots from Test 1/Setup B. Because of discontinuity, the green region is now perturbed and a new peak and valley is formed in the middle.
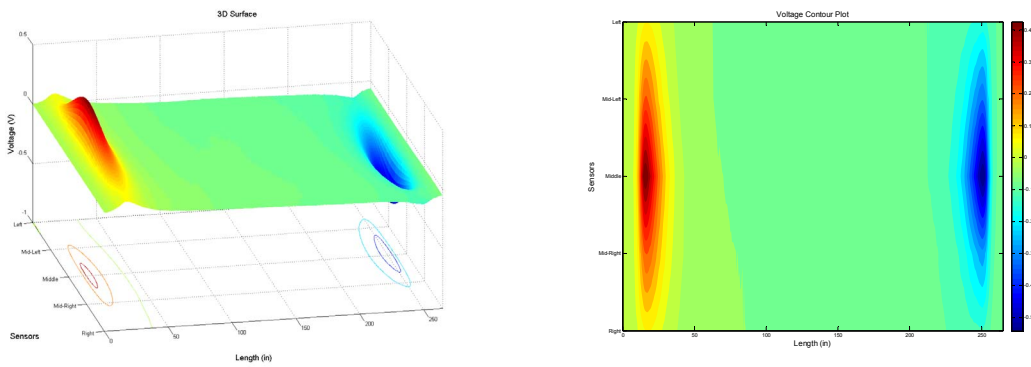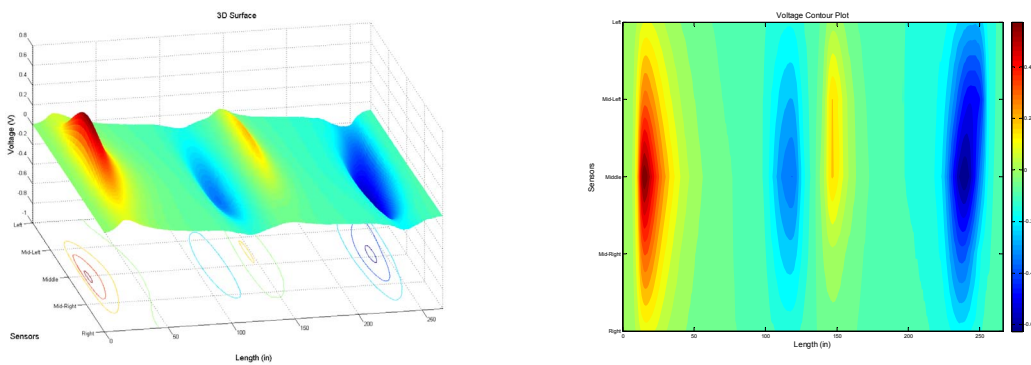

Figure 6-21: 3D plot (left) and contour plot (right) of P1B experiment

Figure 6-22 shows respectively the 3D and contour plots from Test 2/Setup B. Comparing Figure 6-21 with Figure 6-22, it can be observed that the peak and valley amplitude are greater at Figure 6-21, as expected since the experiment P1B (discontinuous strand) had a greater ratio of cross section loss than in the experiment P2B (corroded strand).
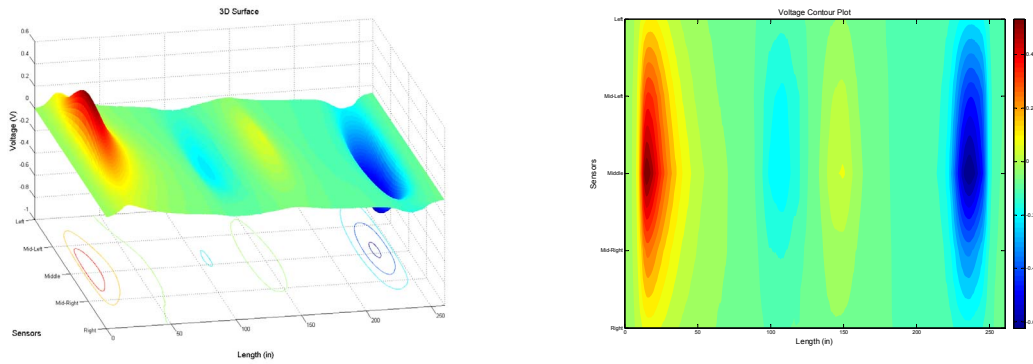

Figure 6-22: 3D plot (left) and contour plot (right) of P2B experiment

6.7　Conclusion

Figure 6-23 shows the results from two different approaches considered here. Discontinuous and corroded strands are analyzed here.

It can be easily noted that the discontinuous approach returns a higher disturbance in the measured magnetic field when compared with the corroded approach. This difference has a straight forward explanation. As previously mentioned, the electrical potential is proportional to cross section loss, since the difference of section loss from discontinuous to the corroded is approximately 50%. This implies a measured electrical potential which is also 50% less.

Since the numbers of strands are kept constant, no other difference at the ends are observed. Both graphics are identical and only differ in the middle because of the presence of either corrosion or gap.

As previously mentioned, another advantage of having more sensors transversal to the direction of the experiment is the possibility of creating 3D surface plots and contour plots. Such plots are very easy to interpret and results are easy to understand since colorful scale and profundity now can be added to the picture.
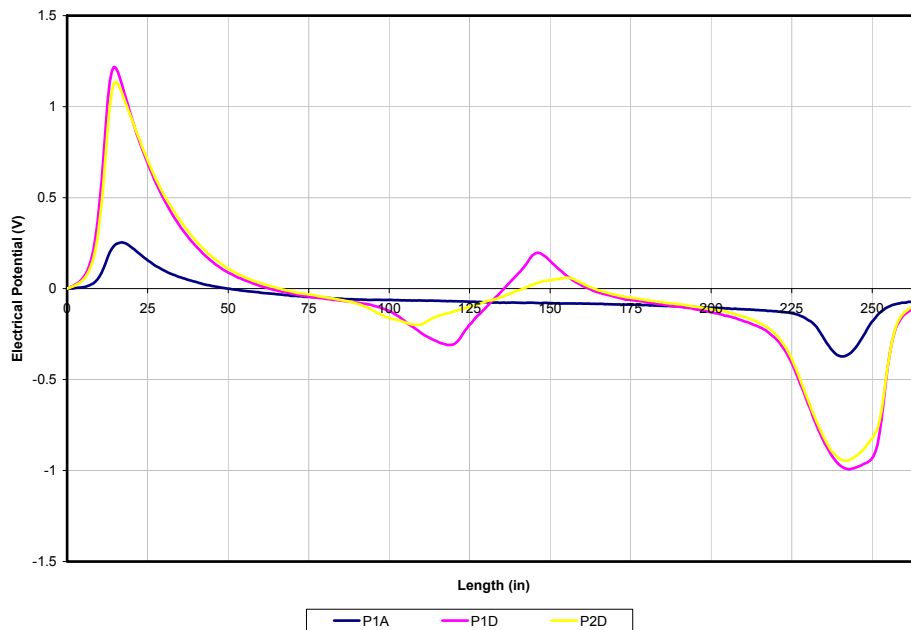

Figure 6-23: Test results comparing discontinuous and corroded results

Chapter 7

Conclusion

This report provides a summary of the findings obtained during the development of a new non-destructive evaluation system, which is based on the concept of magnetic flux leakage (MFL).

When magnetic field is applied to ferromagnetic material, such as prestressing strands and/or rebar, magnetic flux will flow through this material. The presence of flaws such as corrosion or fracture alters the natural path of the flow, which forces the magnetic flux to leak. The leakage can be measured by using non-destructive techniques such as MFL devices that are equipped with Hall-effect sensors. The correlation of magnetic flux leaked and the amount of section loss can be determined.

Magnetic configuration no. 5 is considered to be the best permanent magnet developed here. The U-shaped magnet yoke consists of seven grade 45 neodymium magnets with a residual flux density of 13300 Gauss each alternating between six V-shaped spacers made of highly permeable, high saturation, magnetic iron.

The MFL device, with a group of 15 Hall-effect sensors has been shown to be the best sensor configuration. In addition, the best locations for those sensors are here concluded to be between the two magnetic Poles. This configuration allows simultaneous measurement of both the longitudinal and transverse magnetic field with respect to the direction of testing. The device is lightweight for easy transportation and runs over rails avoiding uneven surface during a field application. A laptop computer is easily connected to the device to acquire and analyze the MFL data as well as to control all electronic boards and sensors. The device, after minor changes, can perform tests on a vertical surface. The installation and operation of the MFL device was successfully demonstrated by laboratory studies.

Wide ranges of test specimens were considered to simulate all possible situations. No difference was observed if the tests were carried out over a concrete or wooden

specimen. It was also noticed that there is no difference between the signal measured considering a gap (discontinuity) or corrosion in the strands. The MFL device here developed was capable of detecting corrosion levels that varied from 8% and up in loss. Based on laboratory testing, the residual MFL method of detection may prove to be more sensitive with respect to low levels of corrosion.

The MFL response is influenced by a larger number of factors, including:

- Concrete cover or distance from the sensor to the ferromagnetic material

- Cross-sectional area of the prestressing steel or reinforcement

- Number of prestressing steel wires in the duct and shielding effect if a metal duct is used

- Number of wires that are broken or corroded in the cross-sectional

- Presence of other ferromagnetic components, especially mild reinforcement

- Magnetic properties of the steel and surrounding materials

- Strength of the magnet used and saturation level of elements

- Location of the sensors with respect to flaws

In summary, a series of laboratory tests were carried out to develop the methodology and the non-destructive device itself. An extensive amount of numerical analyses were carried out to comprehend the meaning of different signal types that were being obtained from the non-destructive device. Finally, limited field studies were carried out to develop a comprehensive methodology adoptable to field conditions.

Corrosion of steel reinforcing bars or strands in concrete bridges present a great challenge for inspection and safety evaluation of these structures. The non-destructive equipment and associated methodology developed in this project allows effective and rapid assessment of bridges for the presence of corrosion.

Appendix A - Test Setups and Results

Figure A.1 through Figure A.10 show alternately the test setup and test results carried out at plywood specimen no.1 (PS1) using magnetic configuration no.1 (MC1) with nine magnets. The number of boards that separate the specimen from the magnetic source varied from one through five. Each plot contains data collected at every inch from a voltmeter connected to the sensor as the device moved through the specimen. The vertical axes in each plot represent voltage and the horizontal axis represents the location of the device from the point at which the experiment was started. The vertical lines on the horizontal axis represent the location of induced damages.

Figure A.1: Setup of plywood specimen no.1 tested using magnet configuration no.1 with nine magnets and one board
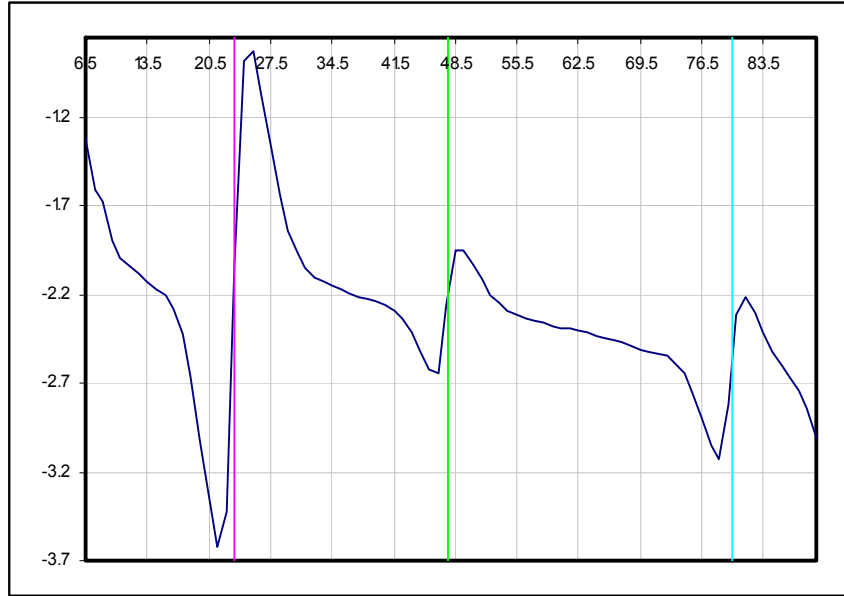
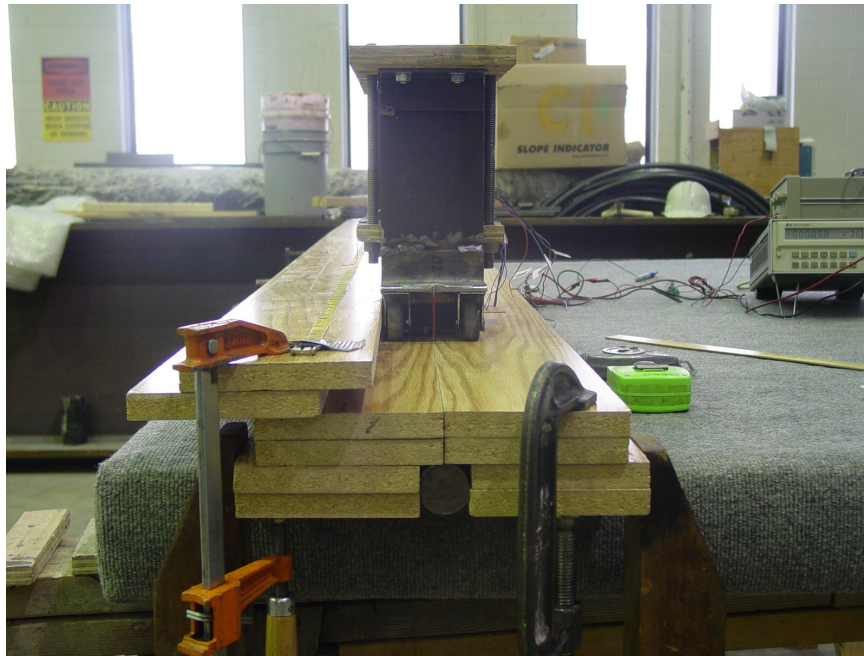**Figure A.2: Results of PS1 tested using MC1 with nine magnets and one board**

Figure A.3: Setup of PS1 tested using MC1 with nine magnets and two boards
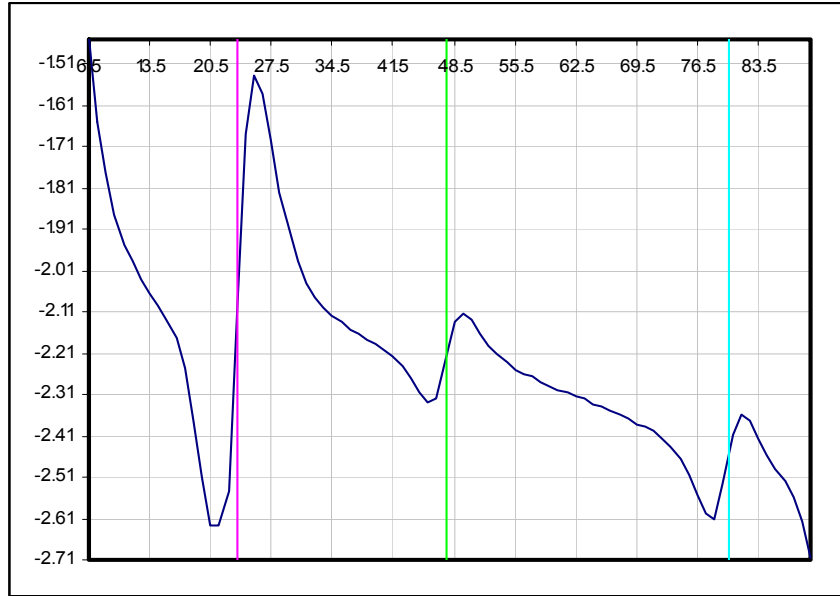
Figure A.4: Results of PS1 tested using MC1 with nine magnets and two boards

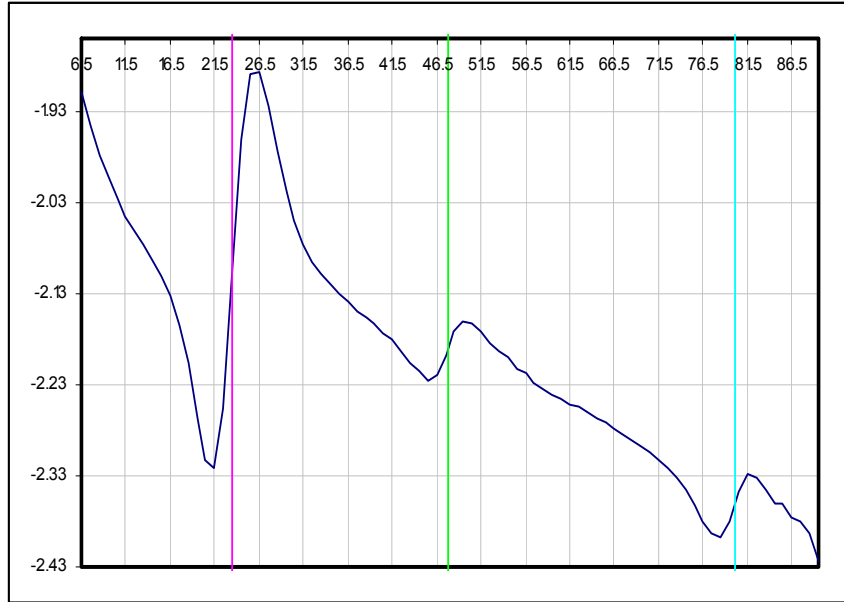**Figure A.5: Setup of PS1 tested using MC1 with nine magnets and three boards**

Figure A.6: Results of PS1 tested using MC1 with nine magnets and three boards

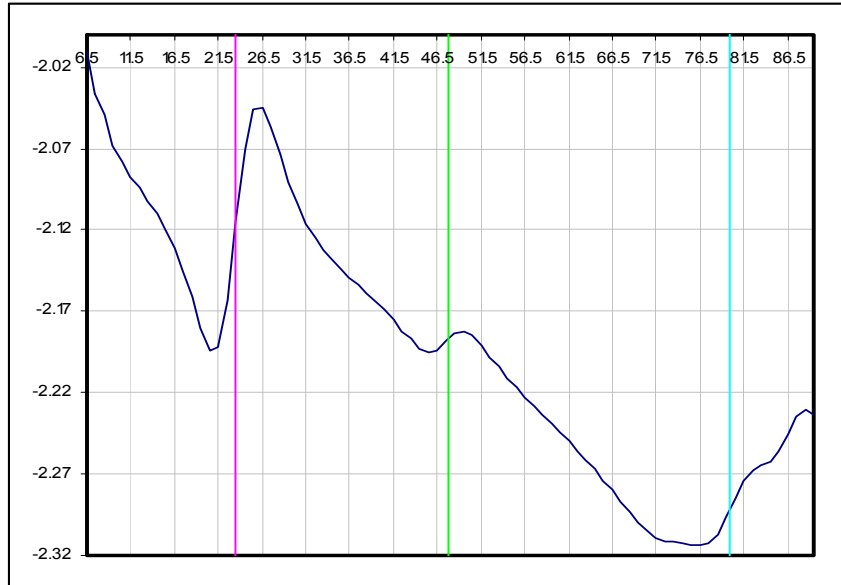**Figure A.7: Setup of PS1 tested using MC1 with nine magnets and four boards**

Figure A.8: Results of PS1 tested using MC1 with nine magnets and four boards

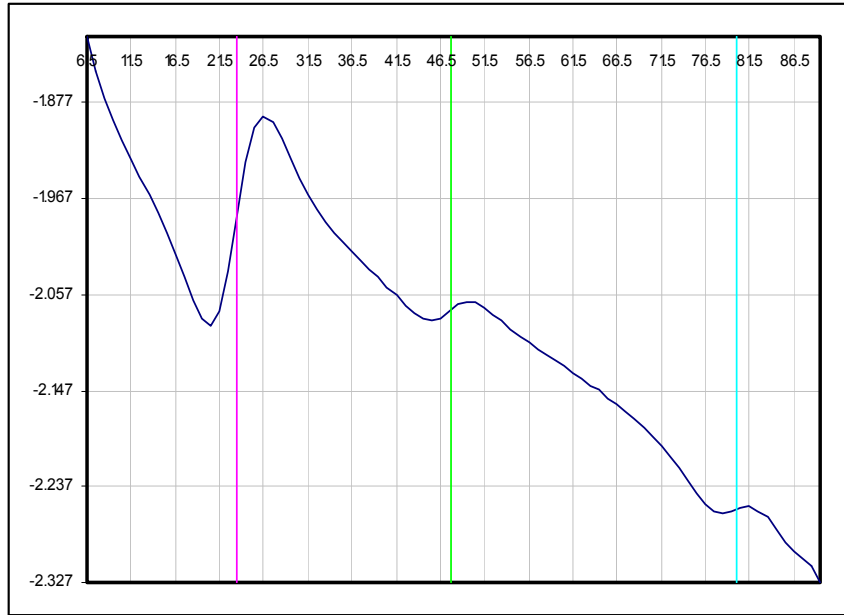**Figure A.9: Setup of PS1 tested using MC1 with nine magnets and five boards**

Figure A.10: Results of PS1 tested using MC1 with nine magnets and five boards

Figure A.11 through Figure A.20 show alternately the test setup and test results carried out at plywood specimen no.1 (PS1) using magnetic configuration no.1 (MC1) with seven magnets. The number of boards that separate the specimen from the magnetic source varied from one through five. Each plot contains data collected at every inch from a voltmeter connected to the sensor as the device moved through the specimen. The vertical axes in each plot represent voltage and the horizontal axis represents the location of the device from the point at which the experiment was started. The vertical lines on the horizontal axis represent the location of induced damages.

Figure A.11: Setup of plywood specimen no.1 tested using magnet configuration no.1 with seven magnets and one board
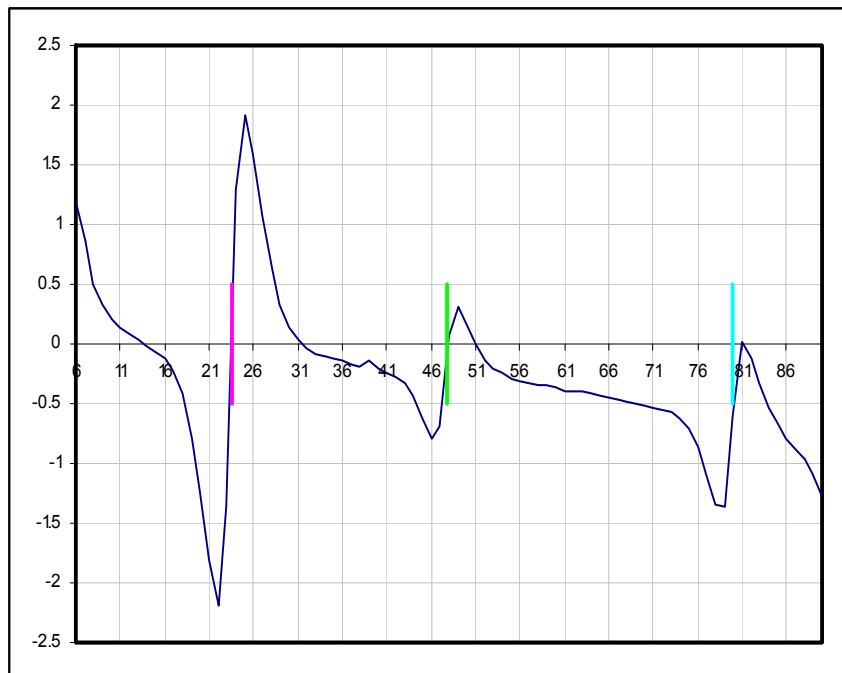

Figure A.12: Results of PS1 tested using MC1 with seven magnets and one board

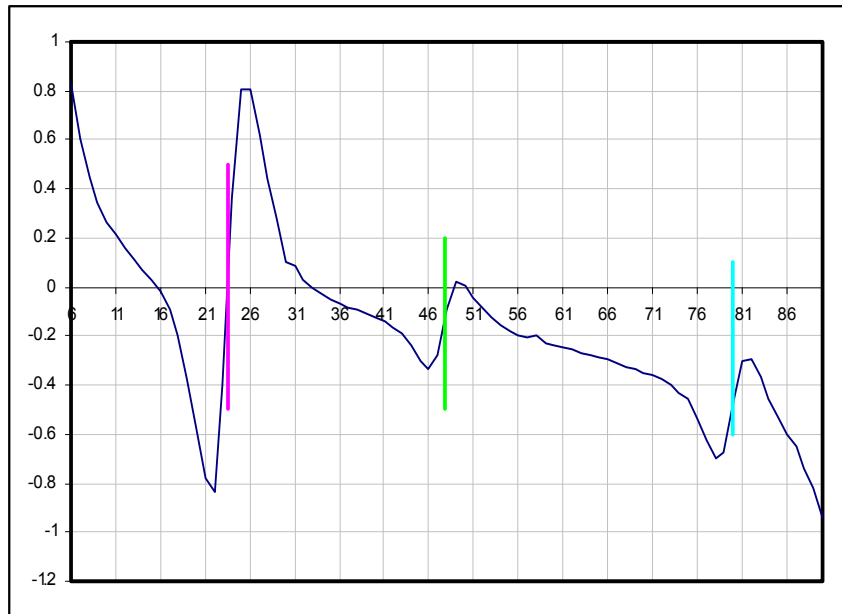**Figure A.13: Setup of PS1 tested using MC1 with seven magnets and two boards**

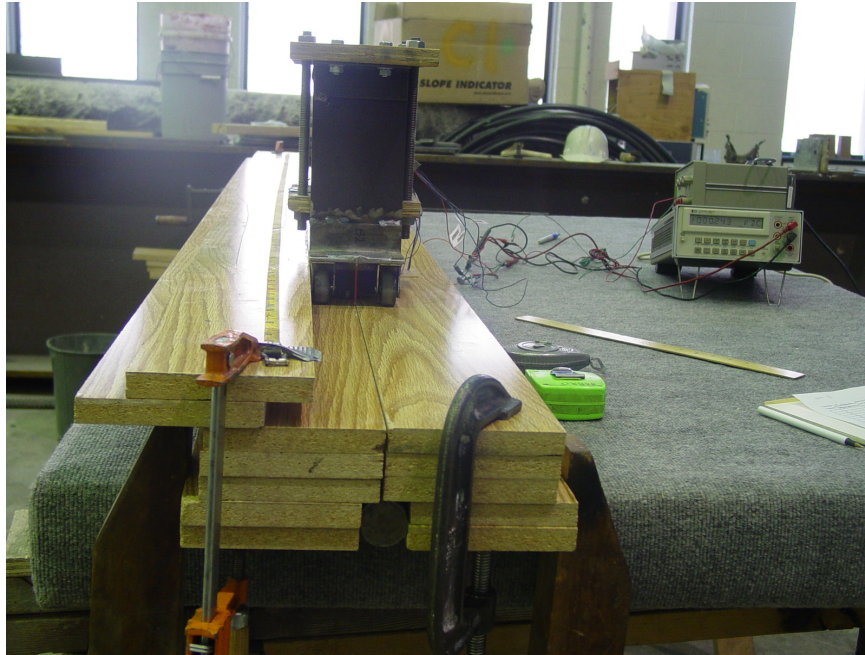**Figure A.14: Results of PS1 tested using MC1 with seven magnets and two boards**

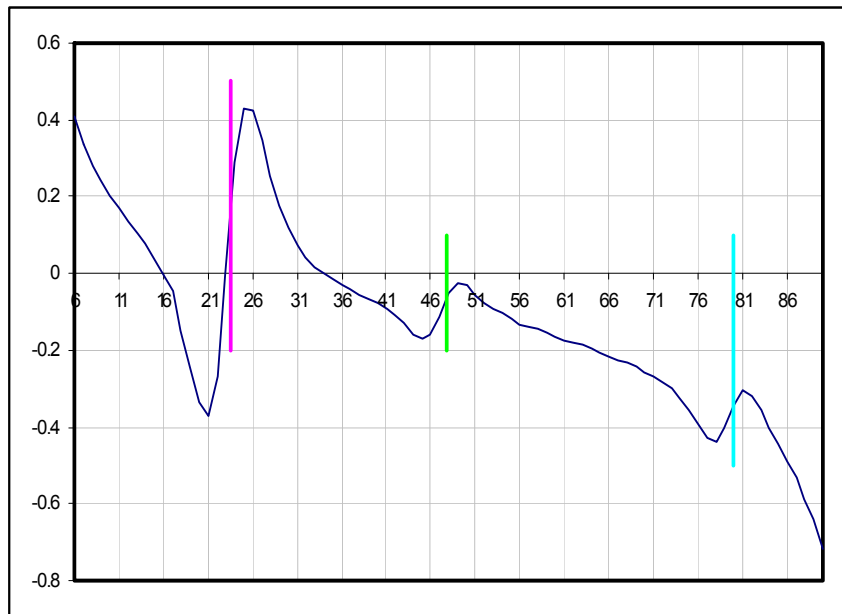**Figure A.15: Setup of PS1 tested using MC1 with seven magnets and three boards**

Figure A.16: Results of PS1 tested using MC1 with seven magnets and three boards
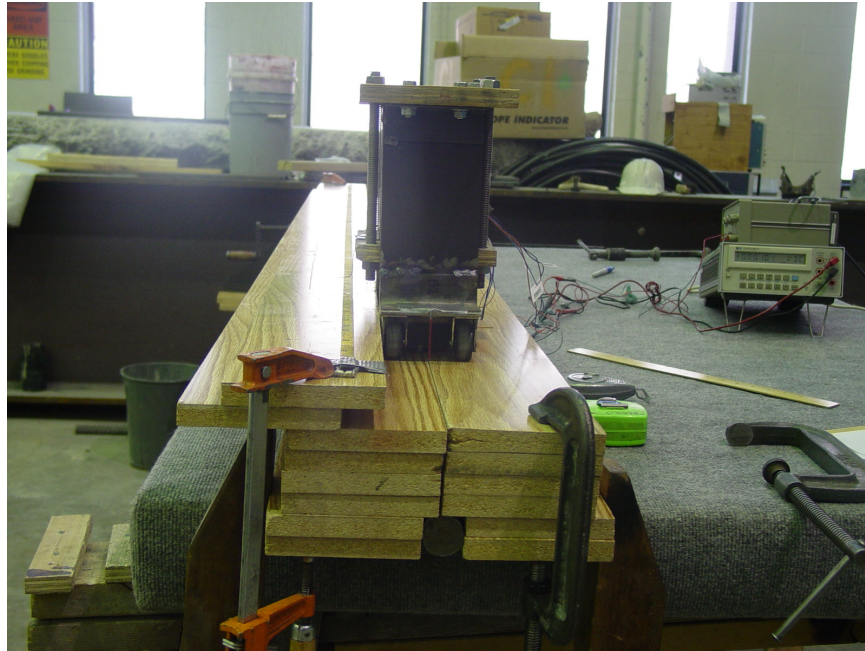
Figure A.17: Setup of PS1 tested using MC1 with seven magnets and four boards
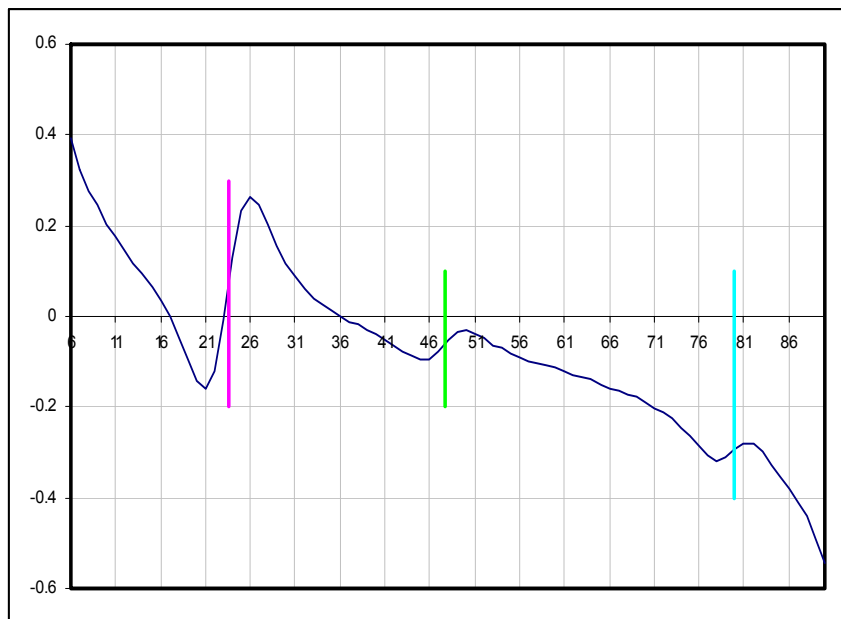

Figure A.18: Results of PS1 tested using MC1 with seven magnets and four boards

Figure A.19: Setup of PS1 tested using MC1 with seven magnets and five boards
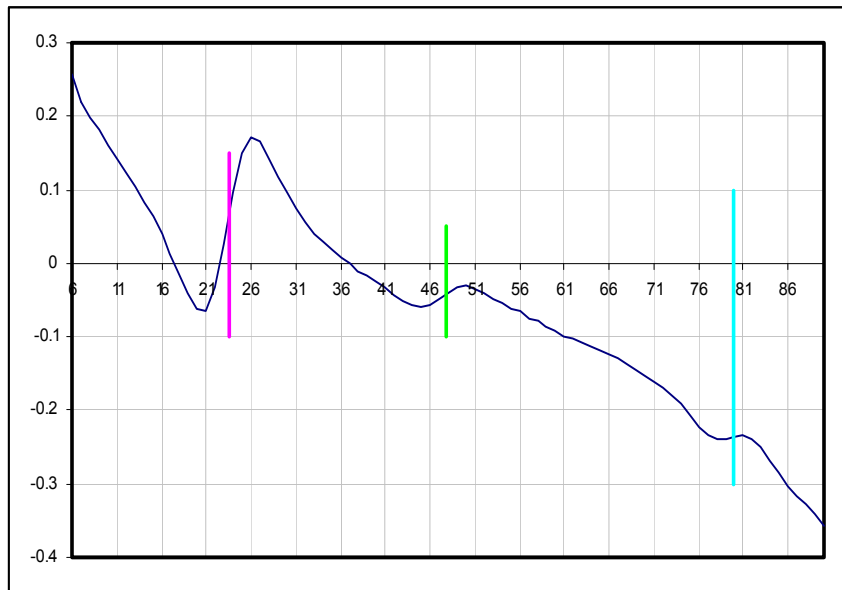

Figure A.20: Results of PS1 tested using MC1 with seven magnets and five boards

Figure A.21 and Figure A.22 show the test setup and test results carried out at plywood specimen no.1 (PS1) using magnetic configuration no.1 (MC1) with five magnets, respectively. Two boards were used to separate the specimen from the magnetic source. The plot contains data collected at every inch from a voltmeter connected to the sensor as the device moved through the specimen. The vertical axis represents voltage and the horizontal axis represents the location of the device from the point at which the experiment was started. Auxiliary lines have been drawn to identify the location of induced damages.

Figure A.21: Setup of plywood specimen no.1 tested using magnet configuration no.1 with five magnets and two boards
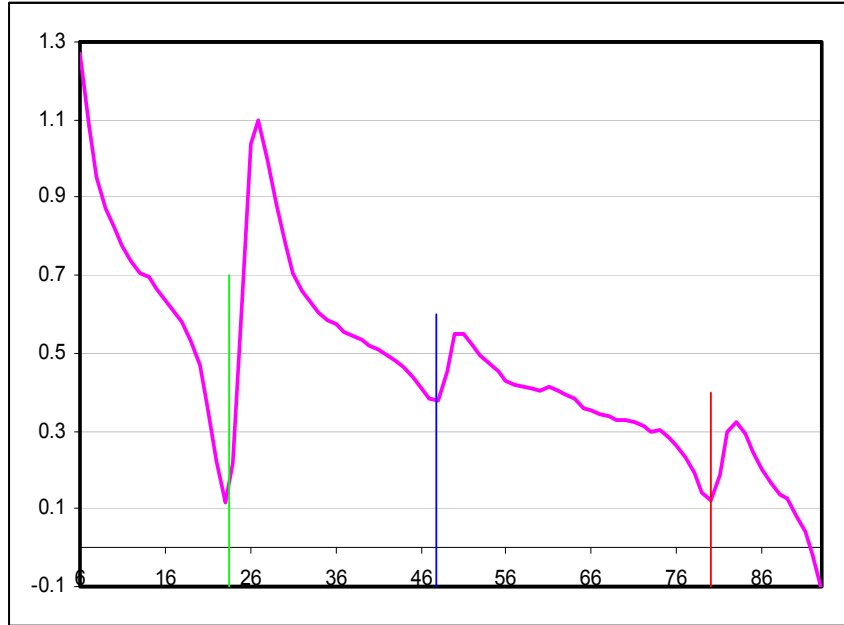
Figure A.22: Results of PS1 tested using MC1 with five magnets and two boards

Figure A.23 and Figure A.24 show the test setup and test results carried out at plywood specimen no.1 (PS1) using magnetic configuration no.1 (MC1) with three magnets, respectively. Two boards separate the specimen from the magnetic source. The plot contains data collected at every inch from a voltmeter connected to the sensor as the device moved through the specimen. The vertical axis represents voltage and the horizontal axis represents the location of the device. Auxiliary lines have been drawn to identify the location of induced damages.

Figure A.23: Setup of plywood specimen no.1 tested using magnet configuration no.1 with three magnets and two boards
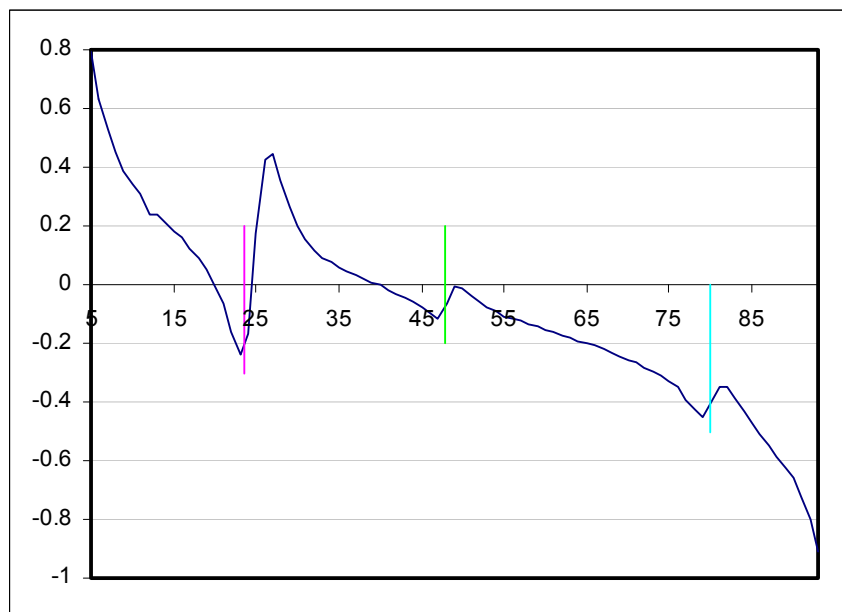

Figure A.24: Results of PS1 tested using MC1 with three magnets and two boards

Figure A.25 and Figure A.26 show the test setup and Figure A.27 and Figure A.28 show the test results carried out at plywood specimen no.1 (PS1) using magnet configuration no.3 (MC3). Two boards separate the specimen from the magnetic source. The two sensor activations (SA) were considered: SA#1 assumes sensors 6-10 ON from group B and ALL OFF from group A and SA#2 assumes ALL sensors ON from group B and ALL OFF from group A. The plot contains data collected at every inch from a voltmeter connected to the sensor as the device moved through the specimen. The vertical axis in each plot represents voltage and the horizontal axis represents the location of the device. Auxiliary lines have been drawn to identify the location of induced damages.

Figure A.25: Setup of plywood specimen no.1 tested using magnet configuration no.3, two boards and two different sensor activations
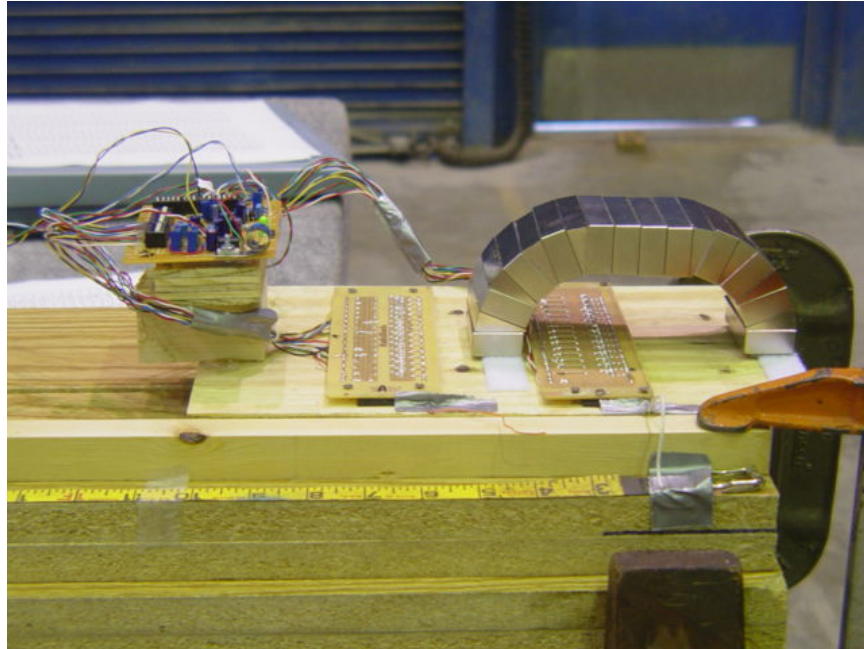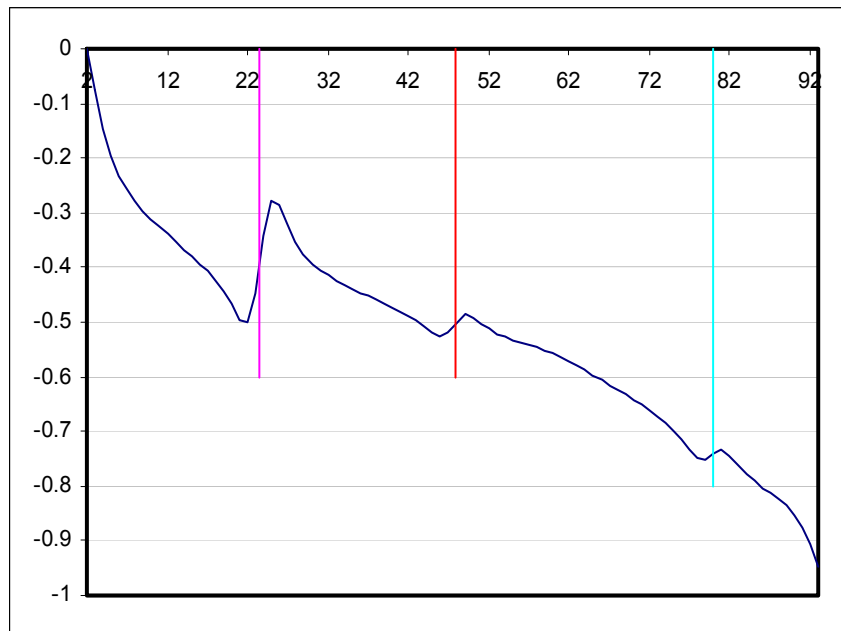
Figure A.26: Lateral view of PS1 tested using MC3

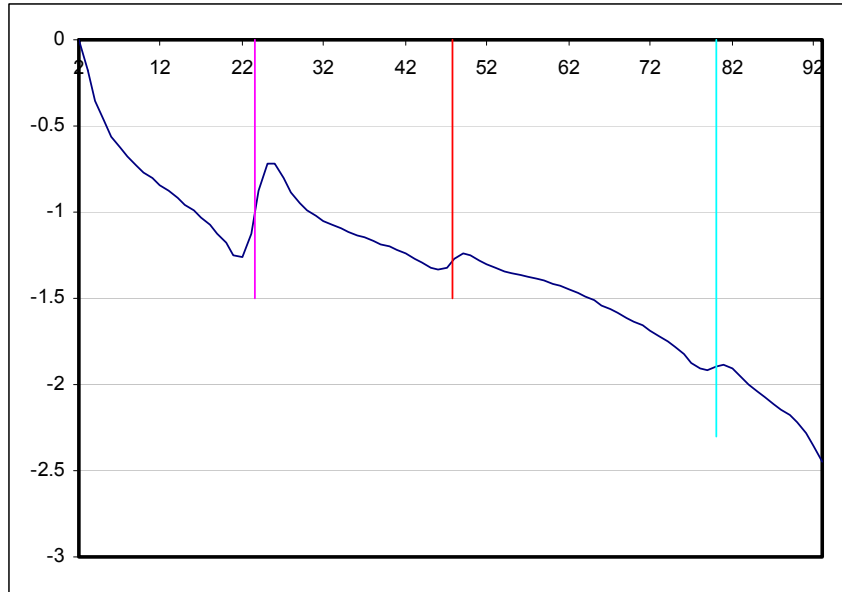**Figure A.27: Results of PS1 tested using MC3, two boards and SA#1**

Figure A.28: Results of PS1 tested using MC3, two boards and SA#2

Figure A.29 through Figure A.32 show the test setup and results from the test carried out at plywood specimen no.2 (PS2) using magnet configuration no.3 (MC3). Only one board was used to separate the specimen from the magnetic source, also one sensor activation (SA). SA#1 considers ALL sensors ON from group B and ALL OFF from group A. The plot contains data collected at every inch from a voltmeter connected to the sensor as the device moved through the specimen. The vertical axis represents voltage and the horizontal axis represents the location of the device. Auxiliary lines have been drawn to identify the location of induced damages.

Figure A.29: Setup of plywood specimen no.2 tested using magnet configuration no.3, one board and one sensor activation

Figure A.30: Overview of all rebar considered for PS2

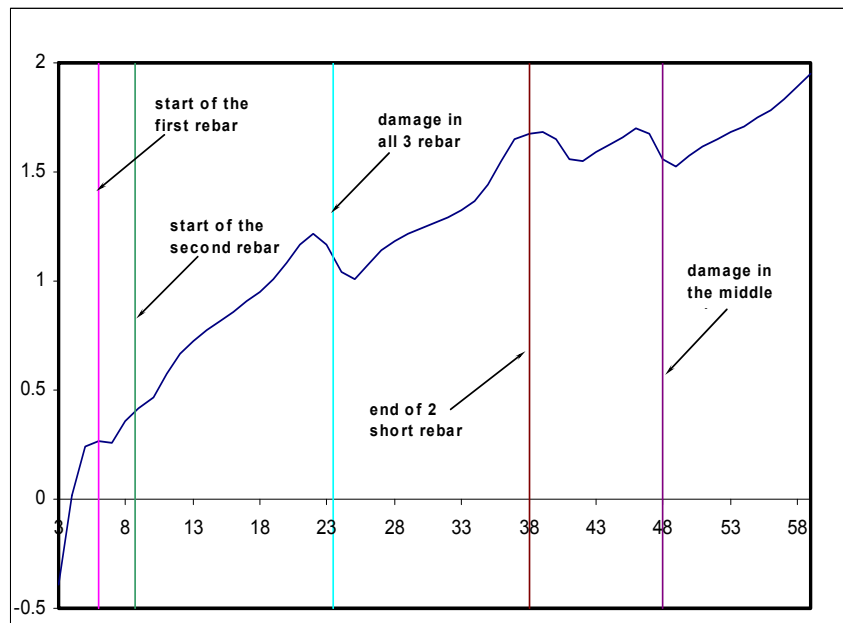**Figure A.31: Close-up view of the alignment of damage at PS2**

Figure A.32: Results of PS2 tested using MC3, one board and SA#1

Figure A.33 and Figure A.34 show the test setup and results carried out at plywood specimen no.4 (PS3) using magnet configuration no.3, respectively. Only one board was used to separate the specimen from the magnetic source, also one sensor activation (SA). SA#1 considers sensors 6-10 ON from group B and ALL OFF from group A. The plot contains data collected at every inch from a voltmeter connected to the sensor as the device moved through the specimen. The vertical axis represents voltage and the horizontal axis represents the location of the device.
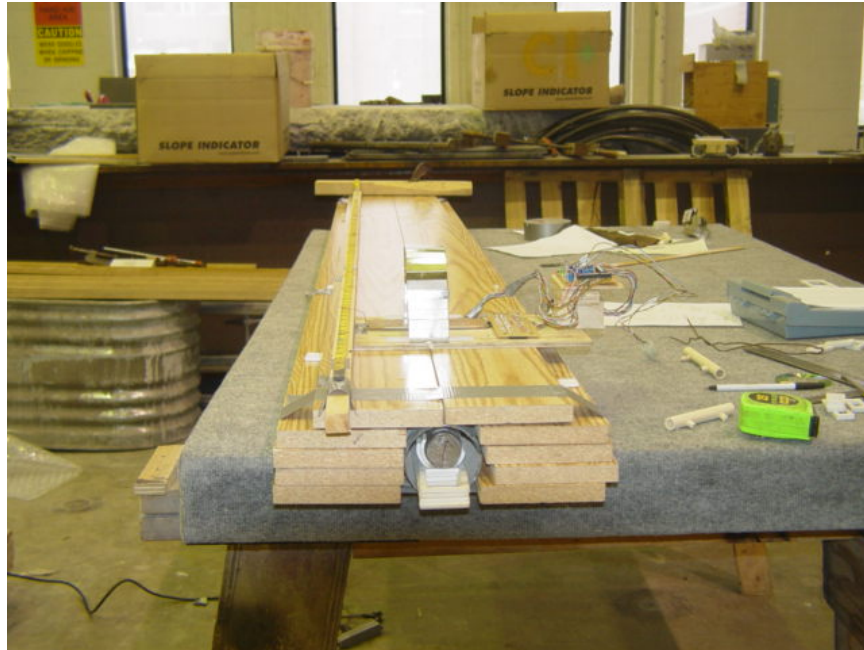

Figure A.33: Setup of plywood specimen no.4 tested using magnet configuration no.3, one board and one sensor activation
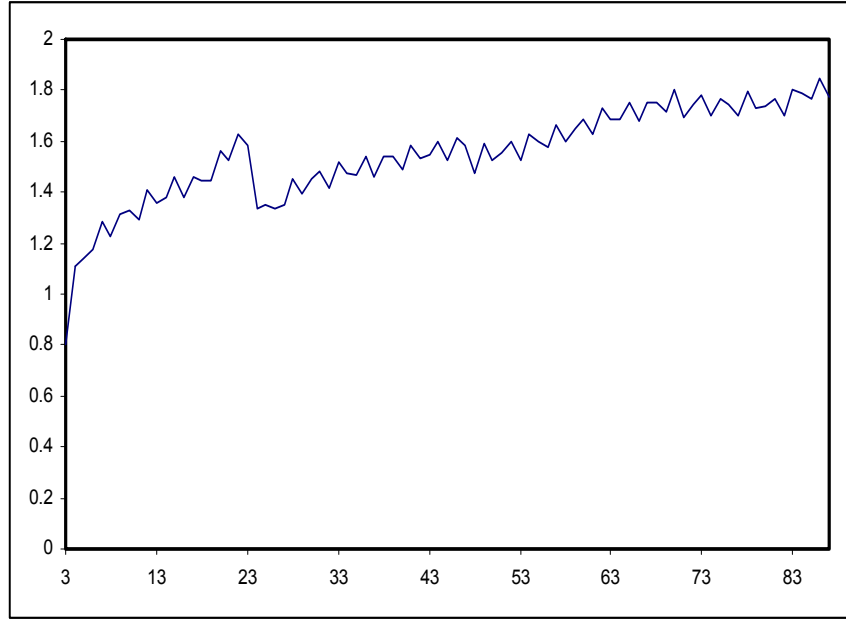
Figure A.34: Results of PS4 tested using MC3, one board and SA#1

Figure A.35 through Figure A.37 show the test setup and Figure A.38 through Figure A.41 show the test results carried out at plywood specimen no.4 (PS4) using magnet configuration no.4 (MC4). Two boards separate the specimen from the magnetic source. The four different sensor activations (SA) were considered: SA#1 assumes sensors 6-10 ON from group B and ALL OFF from group A, SA#2 assumes ALL sensors ON from group B and ALL OFF from group A, SA#3 assumes ALL sensors OFF from group B and 6-10 ON from group A, and SA#4 assumes ALL sensors OFF from group B and ALL ON from group A. The plot contains data collected at every inch from a voltmeter connected to the sensor as the device moved through the specimen. The vertical axis in each plot represents voltage and the horizontal axis represents the location of the device. Auxiliary lines have been drawn to identify the location of induced damages.
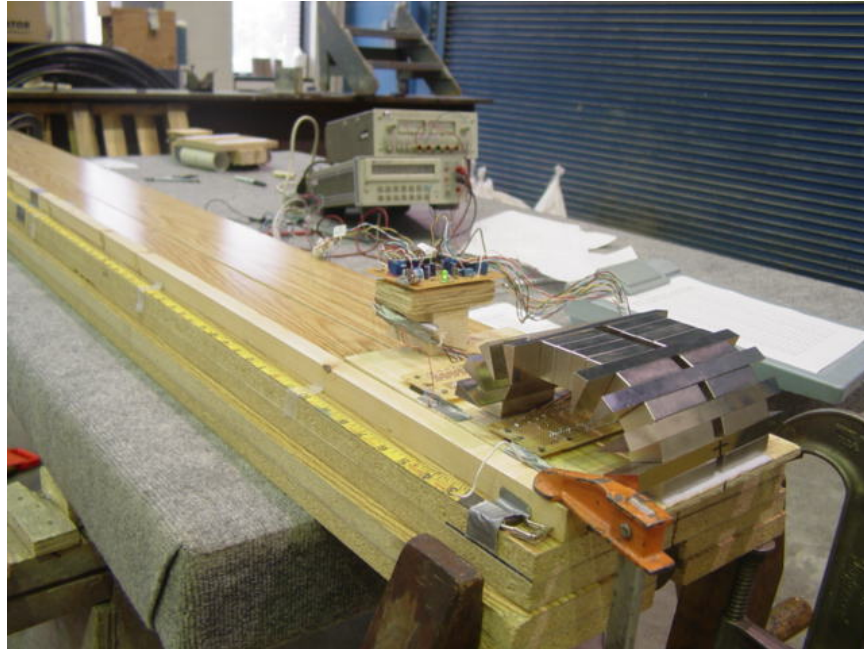
Figure A.35: Setup of plywood specimen no.4 tested using magnet configuration no.4, two boards and four different sensor activations

Figure A.36: Lateral view of PS4 tested using MC4

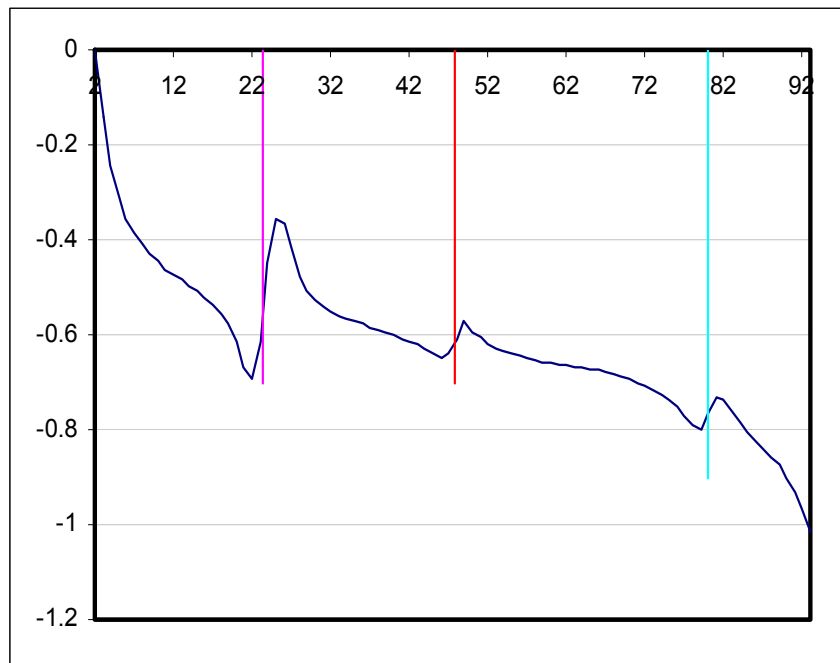**Figure A.37: Front view of PS4 tested using MC4**

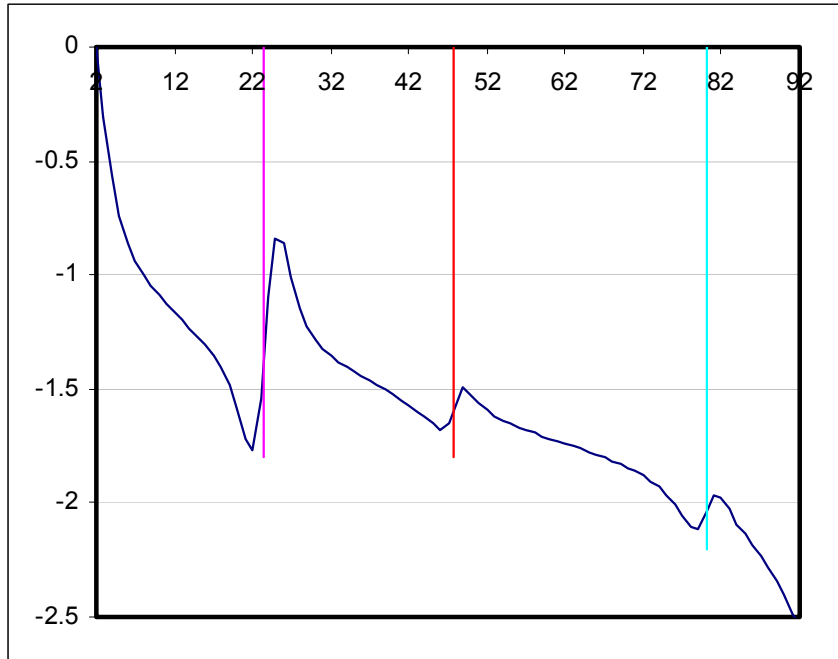**Figure A.38: Results of PS4 tested using MC4, two boards and SA#1**

Figure A.39: Results of PS4 tested using MC4, two boards and SA#2
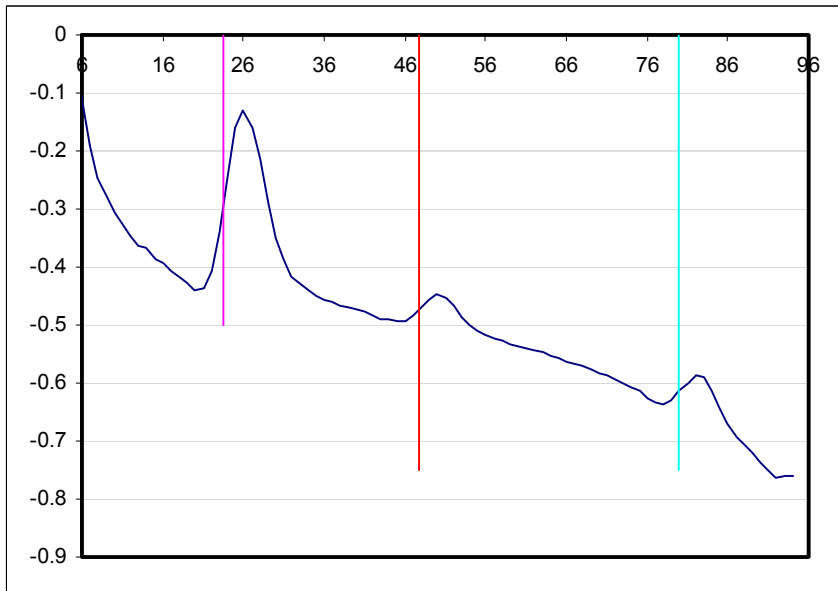

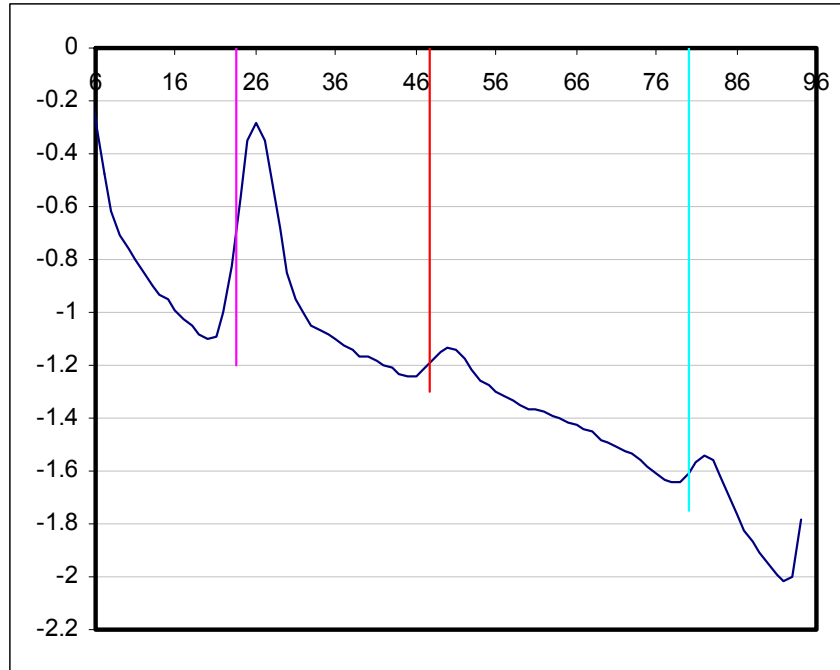**Figure A.40: Results of PS4 tested using MC4, two boards and SA#3**

Figure A.41: Results of PS4 tested using MC4, two boards and SA#4

Figure A.42 and Figure A.43 show the test setup and Figure A.44 through Figure A.47 show the test results carried out at plywood specimen no.4 (PS4) using magnet configuration no.5 (MC5). Two boards were used to separate the specimen from the magnetic source. The four different sensor activations (SA) were considered: SA#1 assumes sensors 6-10 ON from group B and ALL OFF from group A, SA#2 assumes sensors 4-12 ON from group B and ALL OFF from group A, SA#3 assumes ALL sensors ON from group B and ALL OFF from group A, and SA#4 assumes sensors 1-5 ON and 11-15 ON from group B and ALL OFF from group A. The plot contains data collected at every inch from a voltmeter connected to the sensor as the device moved through the specimen. The vertical axis in each plot represents voltage and the horizontal axis represents the location of the device.

Figure A.42: Setup of plywood specimen no.4 tested using magnet configuration no.5, two boards and four different sensor activations

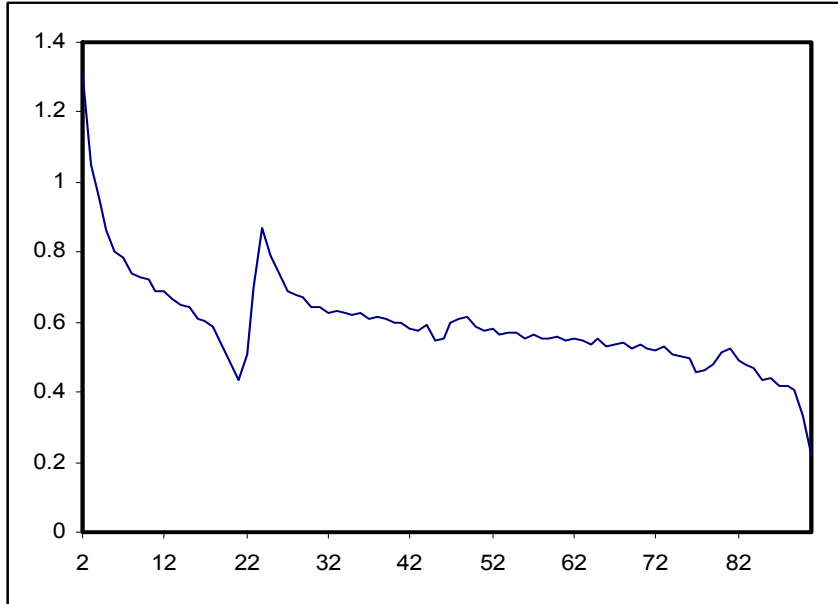**Figure A.43: Front view of PS4 tested using MC5**

Figure A.44: Results of PS4 tested using MC5, two boards and SA#1
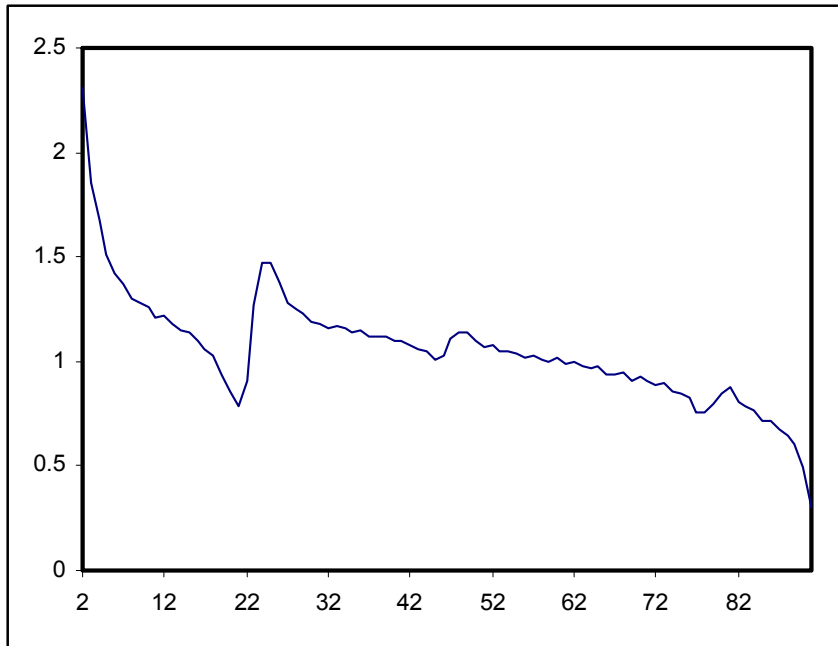

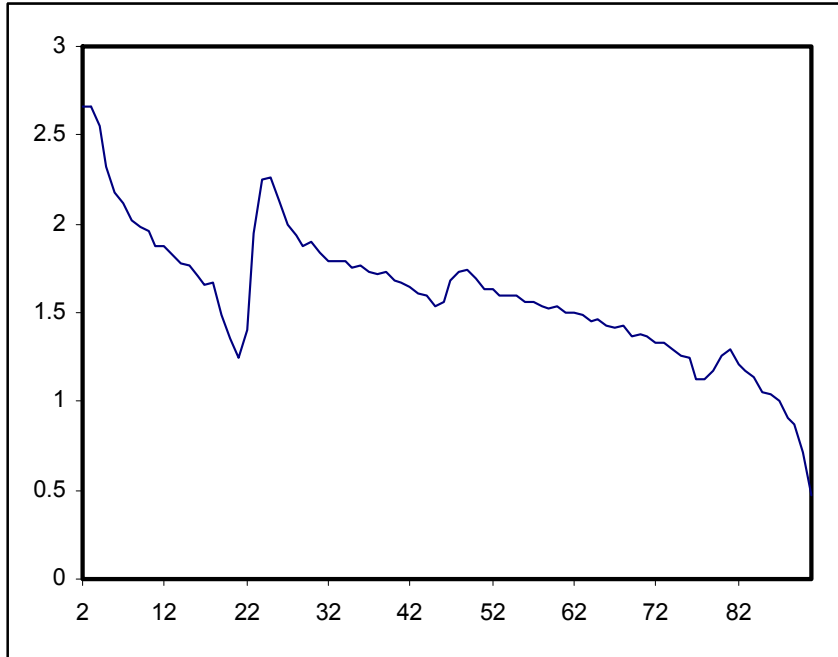**Figure A.45: Results of PS4 tested using MC5, two boards and SA#2**

151

Figure A.46: Results of PS4 tested using MC5, two boards and SA#3
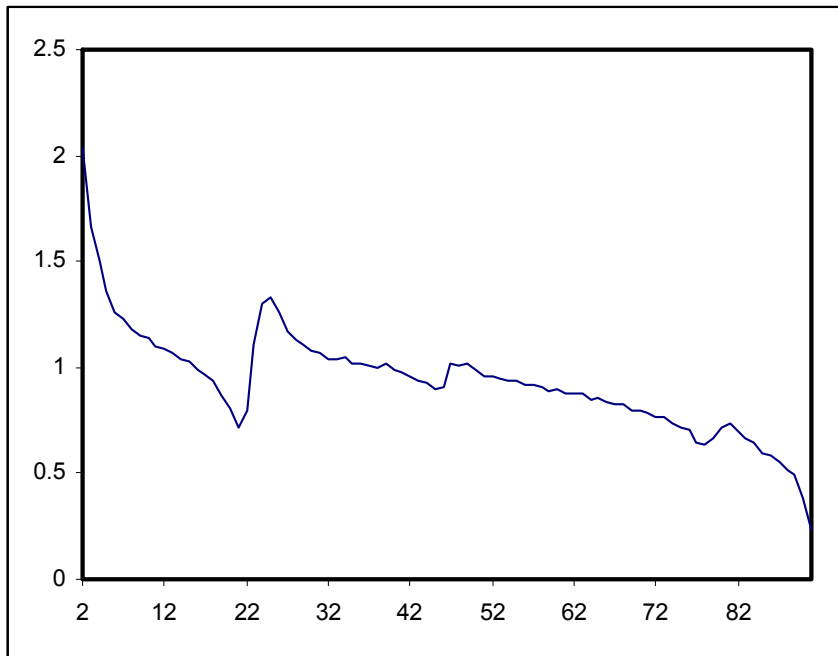

Figure A.47: Results of PS4 tested using MC5, two boards and SA#4

Figure A.48 and Figure A.49 show the test setup and results from the test carried out at plywood specimen no.5 (PS5) using magnet configuration no.5 (MC5), respectively. Two boards were used to separate the specimen from the magnetic source and only one sensor activation (SA) was assumed. SA#1 considers sensors 6-10 ON from group B and ALL OFF from group A. The plot contains data collected at every inch from a voltmeter connected to the sensor as the device moved through the specimen. The vertical axis represents voltage and the horizontal axis represents the location of the device.

Figure A.48: Setup of plywood specimen no.5 tested using magnet configuration no.5, two boards and one sensor activation
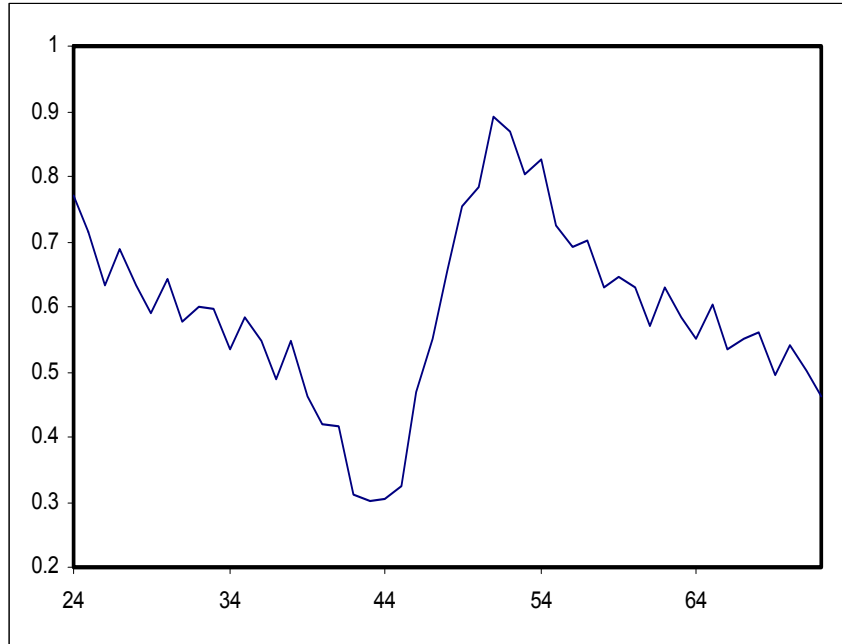
Figure A.49: Results of PS5 tested using MC5, two boards and SA#1

Figure A.50 and Figure A.51 show the test setup and results from the test carried out at plywood specimen no.6 (PS6) using magnet configuration no.5 (MC5), respectively. Two boards were used to separate the specimen from the magnetic source and only one sensor activation (SA) was assumed. SA#1 considers sensors 6-10 ON from group B and ALL OFF from group A. The plot contains data collected at every inch from a voltmeter connected to the sensor as the device moved through the specimen. The vertical axis represents voltage and the horizontal axis represents the location of the device.

Figure A.50: Setup of plywood specimen no.6 tested using magnet configuration no.5, two boards and one sensor activation
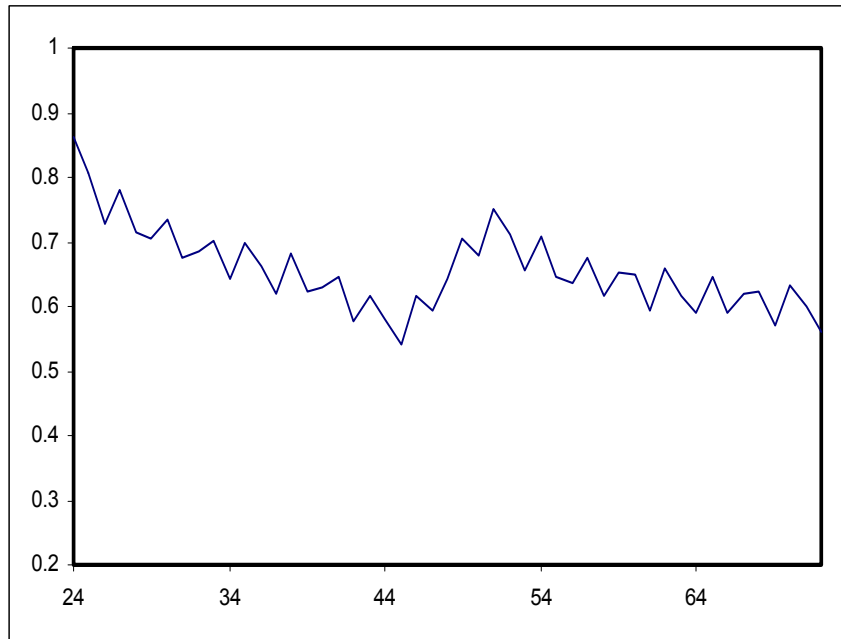

Figure A.51: Results of PS6 tested using MC5, two boards and SA#1

Figure A.52 through Figure A.55 show the test results carried out on plywood specimen no.7 (PS7) using magnet configuration no.5 (MC5). Four different strands arrangement were assumed in PS7, in addition two boards and one sensor activation (SA) was used. SA#1 considers sensors 6-10 ON from group B and ALL OFF from group A. The plot contains data collected at every inch from a voltmeter connected to the sensor as the device moved through the specimen. The vertical axis represents voltage and the horizontal axis represents the location of the device.
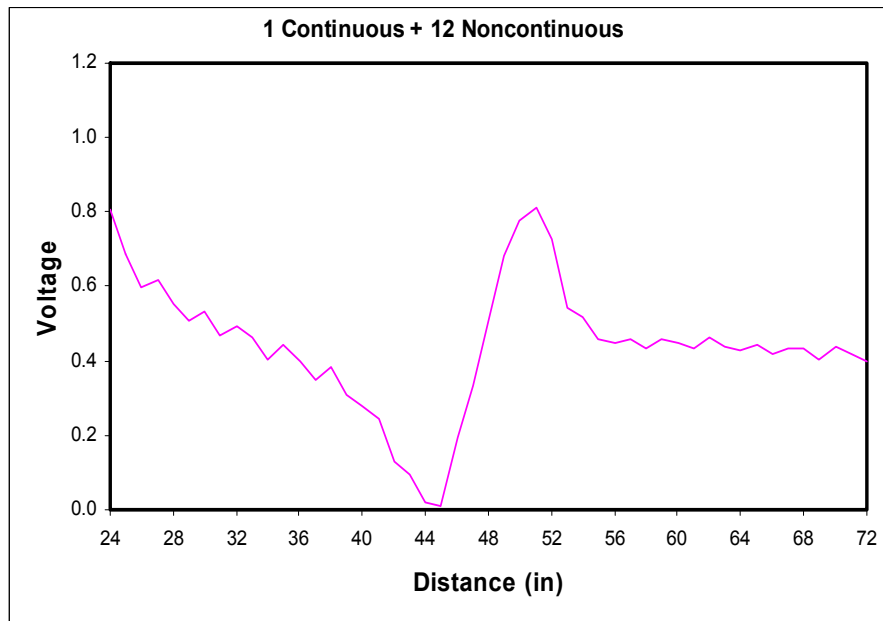

Figure A.52: Results of plywood specimen no.7 (one continuous and 12 non-continuous strands) tested using magnet configuration no.5, two boards and one sensor activation
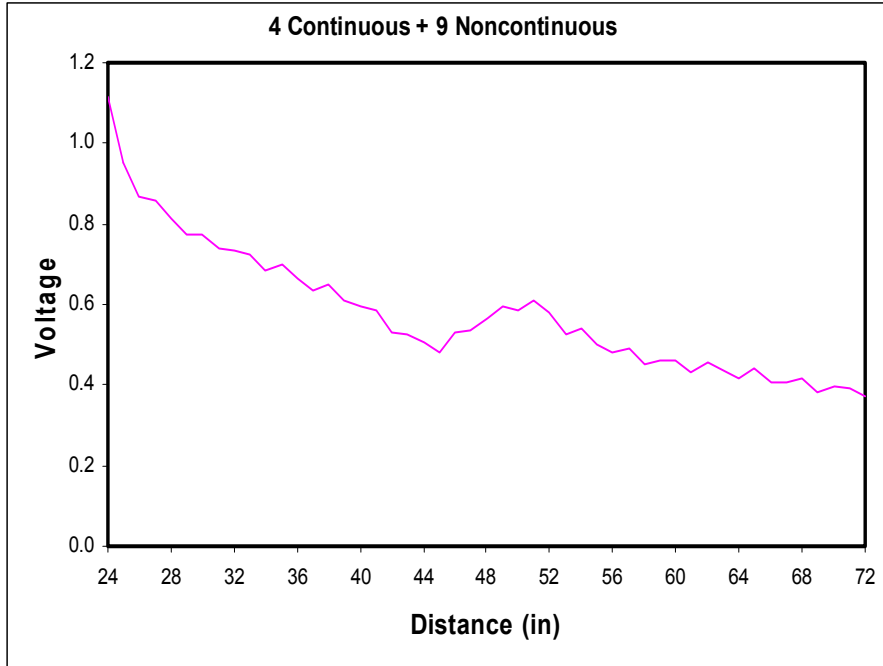
Figure A.53: Results of plywood specimen no.7 (four continuous and nine non-continuous strands) tested using magnet configuration no.5, two boards and one sensor activation
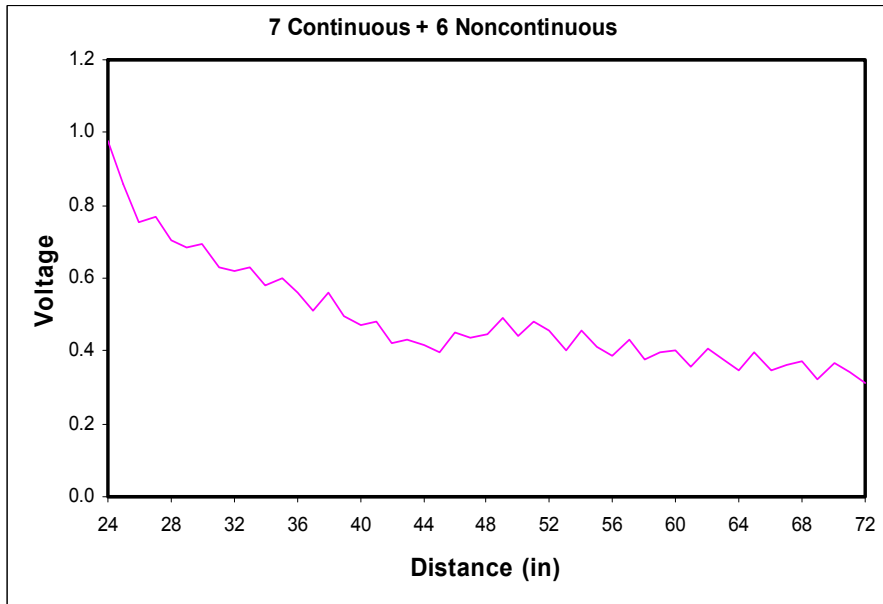

Figure A.54: Results of plywood specimen no.7 (seven continuous and six non-continuous strands) tested using magnet configuration no.5, two boards and one sensor activation
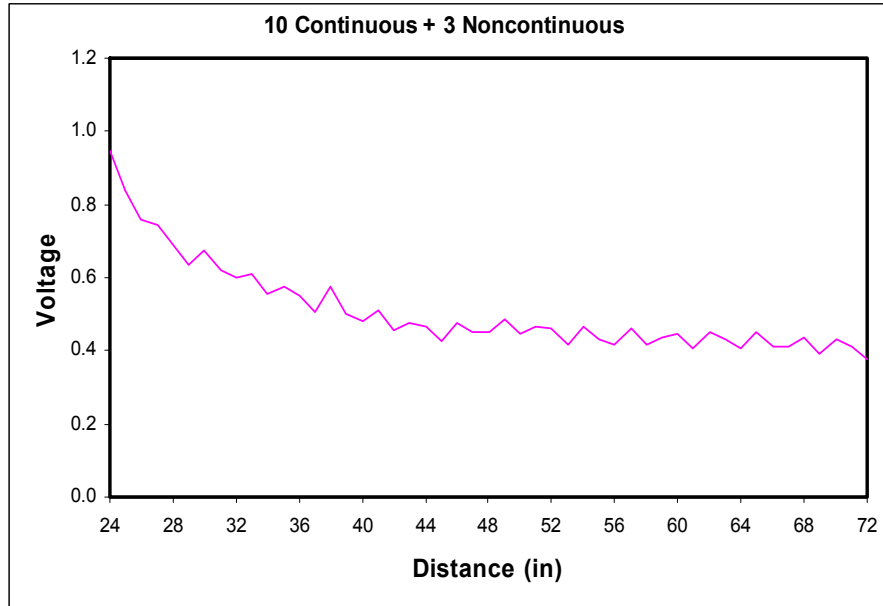
157

10 Continuous + 3 Noncontinuous

Figure A.55: Results of plywood specimen no.7 (10 continuous and three non-continuous strands) tested using magnet configuration no.5, two boards and one sensor activation

Figure A.56 through Figure A.61 show the test setup and test results of experiment carried out on concrete specimen no.1 (CS1), no.2 (CS2) and no.3 (CS3) using magnetic configuration no.1 (MC1) with seven magnets. Each plot contains data collected at every inch from a voltmeter connected to the sensor as the device moved through the specimen. The vertical axis in each plot represents voltage and the horizontal axis represents the location of the device. The vertical lines on the horizontal axis represent the location of induced damages.

Figure A.56: Setup of concrete specimen no.1 tested using magnet configuration no.1 with seven magnets
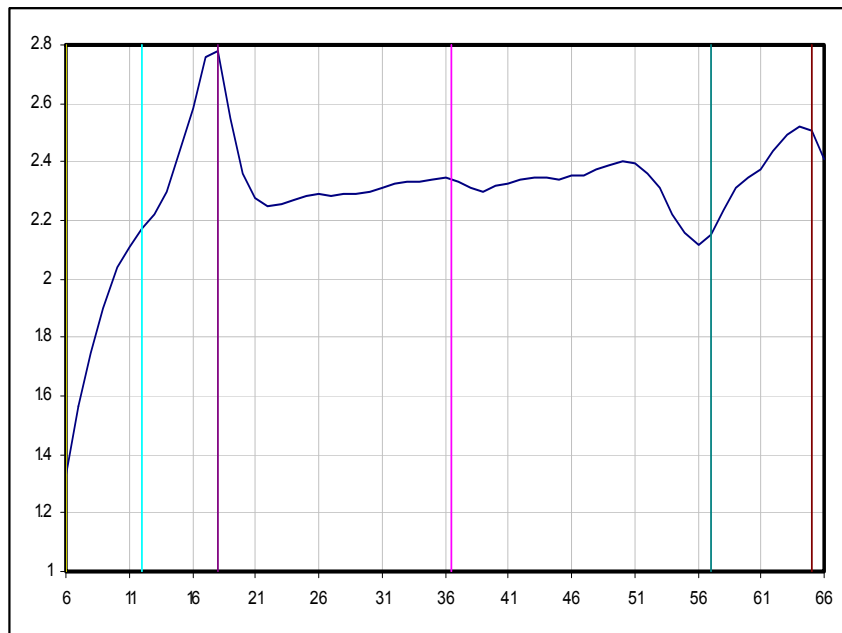

Figure A.57: Results of CS1 tested using MC1 with seven magnets

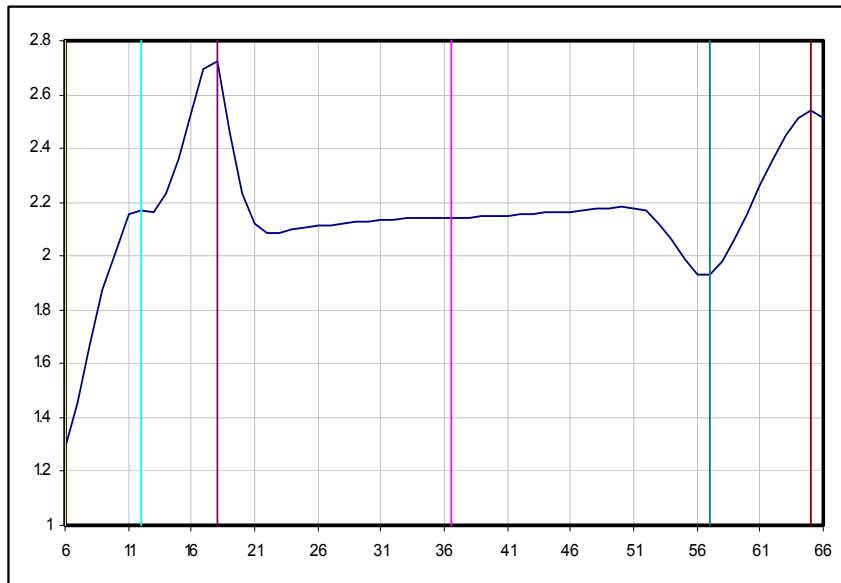**Figure A.58: Setup of CS2 tested using MC1 with seven magnets**

Figure A.59: Results of CS2 tested using MC1 with seven magnets

Figure A.60: Setup of CS3 tested using MC1 with seven magnets
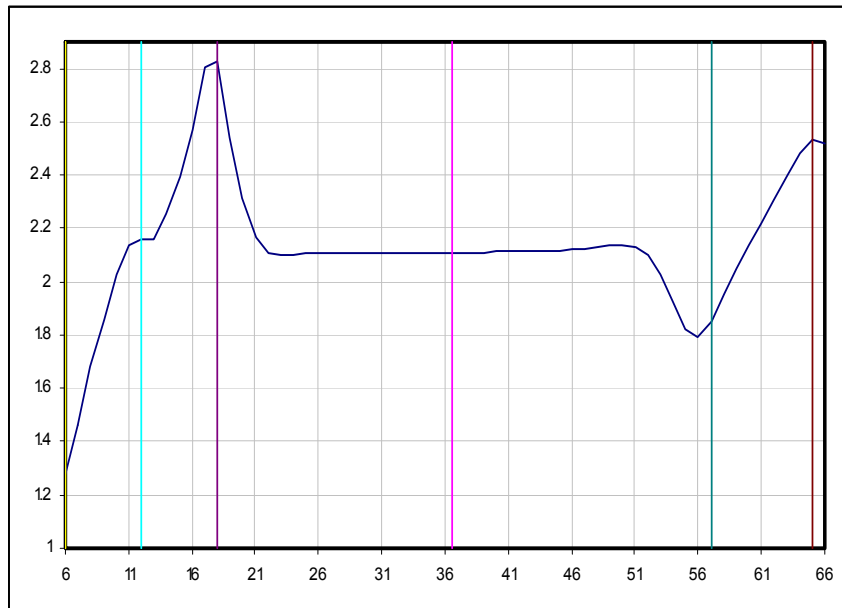

Figure A.61: Results of CS3 tested using MC1 with seven magnets

Figure A.62 through Figure A.65 show the test setup and test results of experiment carried out on concrete specimen no.1 (CS1) and no.2 (CS2) using magnetic configuration no.4 (MC4). The sensor activation (SA) was ALL sensors ON from group B and ALL OFF from group A. Each plot contains data collected at every inch from a voltmeter connected to the sensor as the device moved through the specimen. The vertical axis in each plot represents voltage and the horizontal axis represents the location of the device.

Figure A.62: Setup of concrete specimen no.1 tested using magnetic configuration no.4
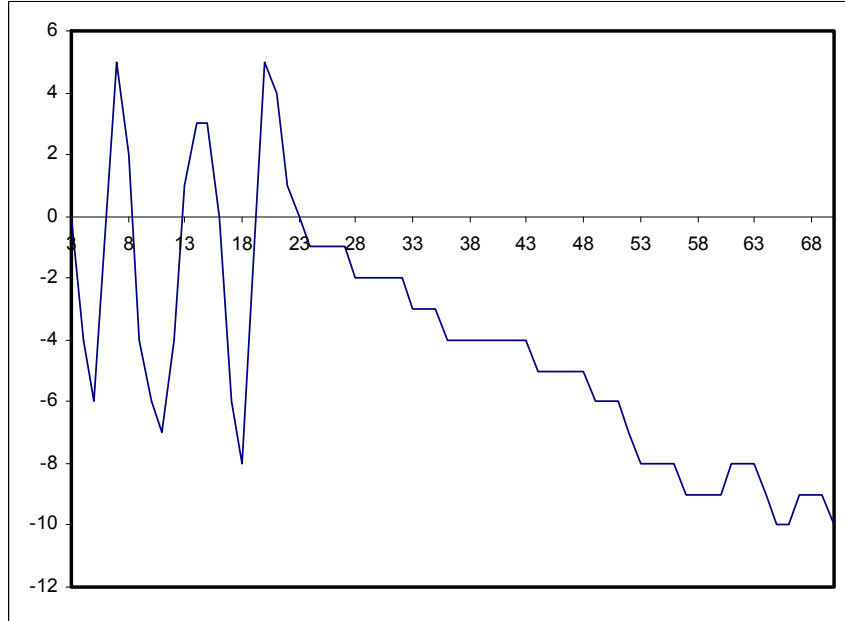
Figure A.63: Results of CS1 tested using MC4

Figure A.64: Setup of CS2 tested using MC4
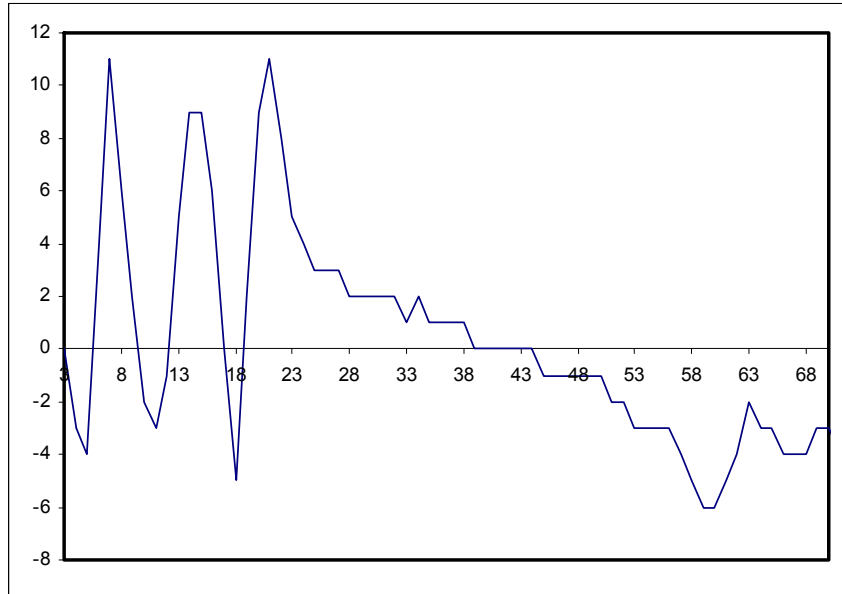
Figure A.65: Results of CS2 tested using MC4

Figure A.66 shows the test results carried out on concrete specimen no.1 (CS1) using magnetic configuration no.5 (MC5). The sensor activation (SA) considered was ALL sensors ON from group B and ALL OFF from group A. The plot contains data collected at every inch from a voltmeter connected to the sensor as the device moved through the specimen. The vertical axis in each plot represents voltage and the horizontal axis represents the location of the device.

Figure A.66: Results of concrete specimen no.1 tested using magnetic configuration no.5
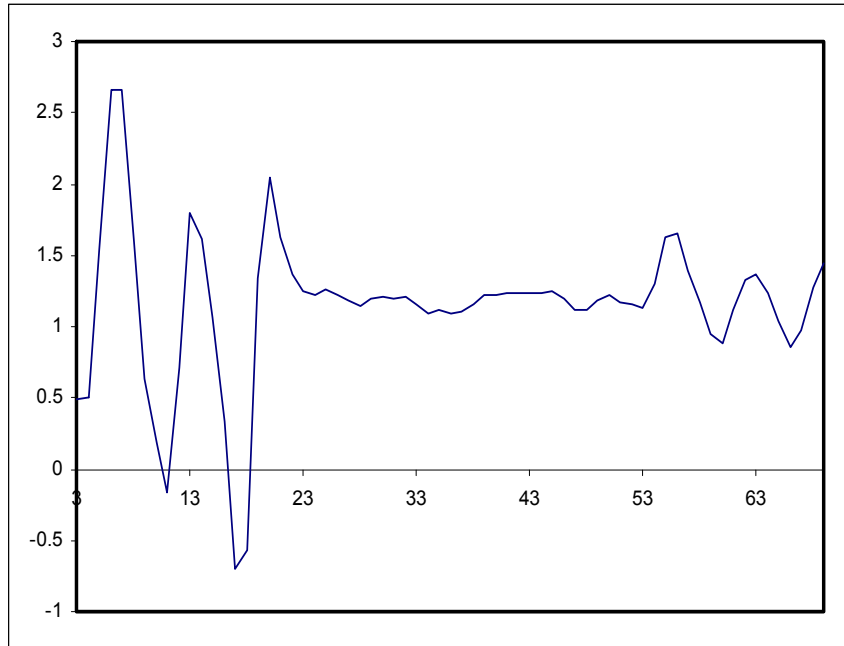
Appendix B - Data Plots from All Tests Setups

Each test lane has six plots covering three rows of sensors at two different magnet positions, low and high. A few of these plots were presented in chapter five. Due to the large number of the plots, they will be available based upon request.

Appendix C - The Signal Processing of MFL Curves Using the FFT Method

C.1   Introduction

There are many methods available to study and process a complex signal. Fast Fourier Transform (FFT) is one of the most widely used methods to process signals. In this method, a signal is studied in the frequency domain. In other words, a signal is divided into many simple sinusoidal curves with specific frequencies. Therefore, every signal can be written as a summation of sinusoidal curves with different amplitudes and frequencies. Each frequency depends on a set of factors.

For example, in Figure C.1, which shows the amount of voltage in a MFL test, the voltage variations have been influenced by many factors such as the location of the transverse bars, bents of metal duct, material properties and many other factors.

Each of these factors creates a change in the curve by a specific frequency or a combination of some simple frequencies. In this study, the frequencies caused by magnetic leakage have been investigated.
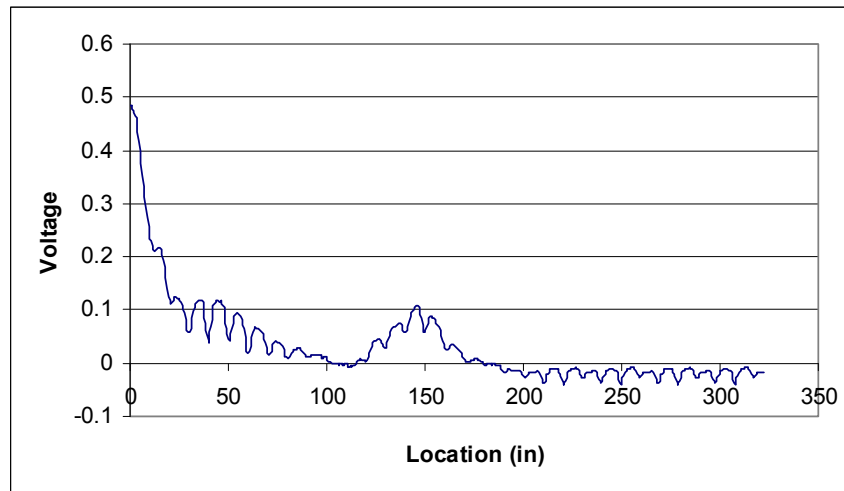

Figure C.1: Results from MFL test

C.2   Frequency Spectrum

Although many different FFT algorithms are available, the decision was made to implement a well-know algorithm called the radix-2 FFT algorithm. The MATLAB software has been used as the platform of implementation and further analyses.

In this method, the number of points should be the power of two. Figure C.2 shows a laboratory test result that was obtained with the passage of the MFL device over a set of strands. To simulate the corrosion, some of those strands were discontinuous leaving a gap at some location.
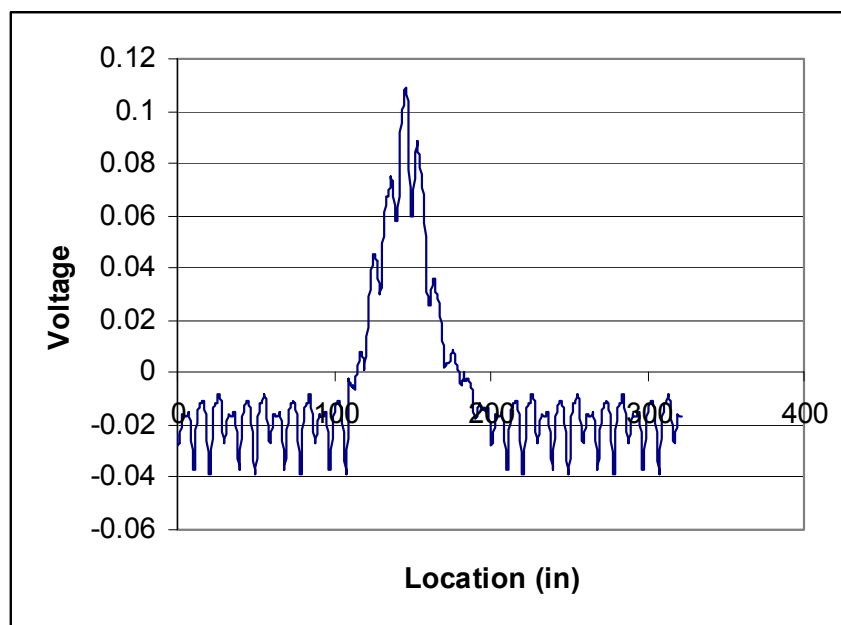

Figure C.2: Modified curve with 512 points in the MFL test

The frequency spectrum was calculated considering the points in calculation which caused different levels of accuracy. Figure C.3, Figure C.4, and Figure C.5 show the frequency spectrum for 512, 8192 and 32768 points, respectively.

According to the graphs, most major frequencies are between 0 and 0.2. Figure C.6 shows the frequency spectrum in the above range.

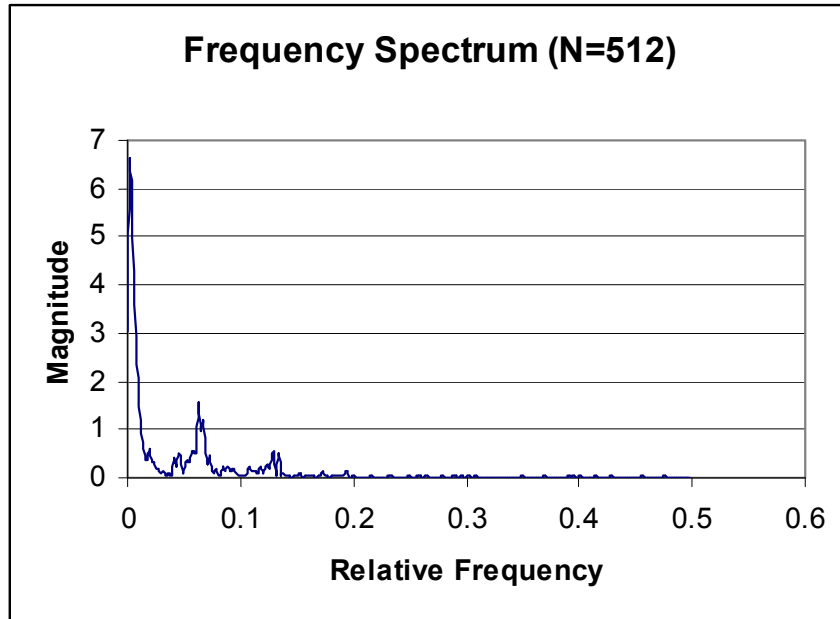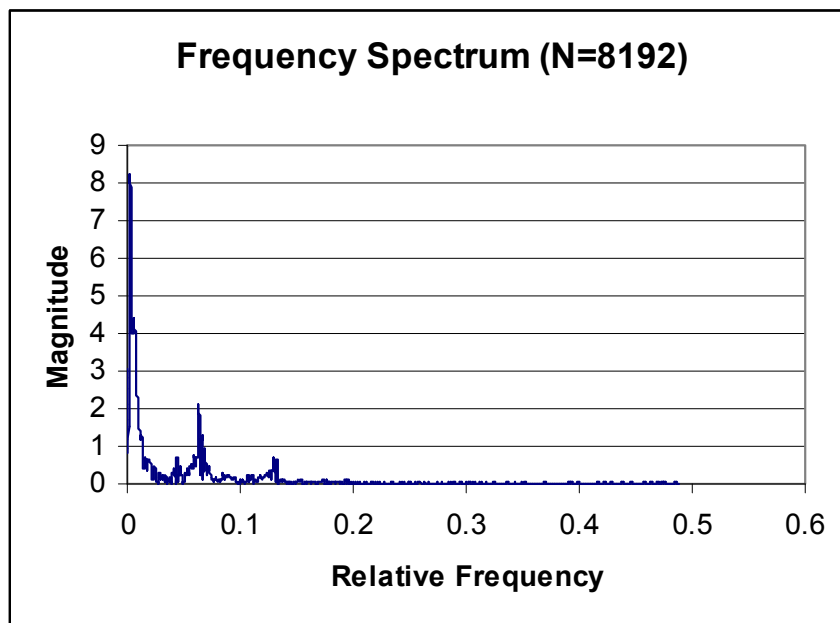**Figure C.3: Frequency spectrum considering 512 points**

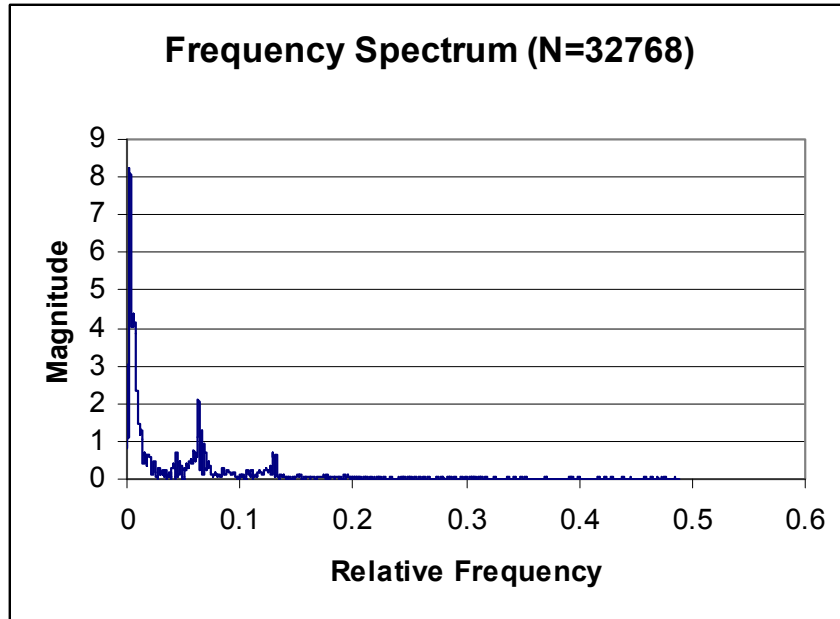**Figure C.4: Frequency spectrum considering 8192 points**

Figure C.5: Frequency spectrum considering 32768 points
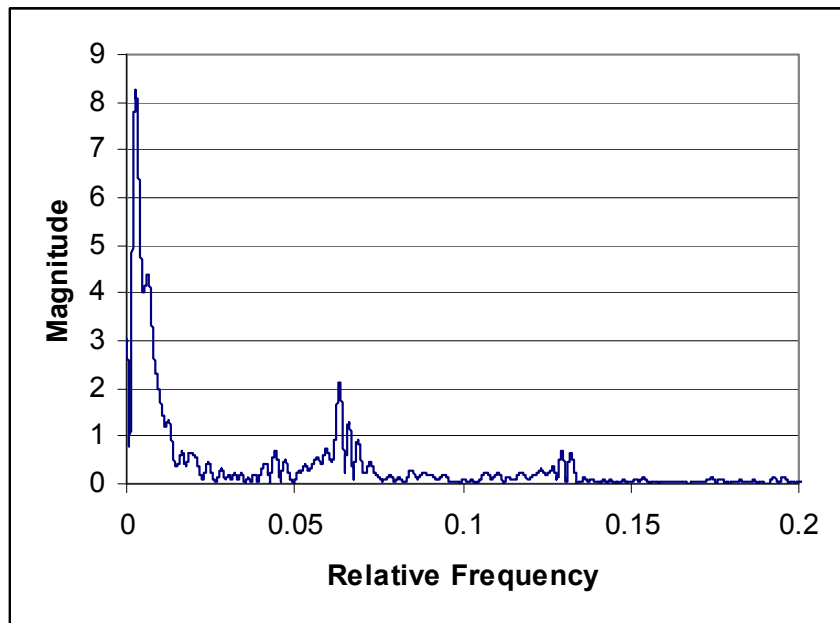

Figure C.6: Frequency spectrum considering major frequencies

C.3   Denoising the Curve

In this study, all frequencies except those created by magnetic leakage were considered noise. According to Figure C.6, the curve has three main frequencies that have a large magnitude. All other frequencies are low with a similar magnitude.

Consequently, all low frequencies with a similar magnitude are considered as noise created by unwanted effects and are removed from the frequency spectrum.

After denoising, the Inverse FFT algorithm is used to gain the denoised curve.

Among more than 16000 frequencies, only three frequencies were considered. It is possible that fewer frequencies also could be also considered. Therefore, denoising by considering one and two frequencies was considered also. Figure C.7 shows the denoised curve which was considered one, two and three frequencies.
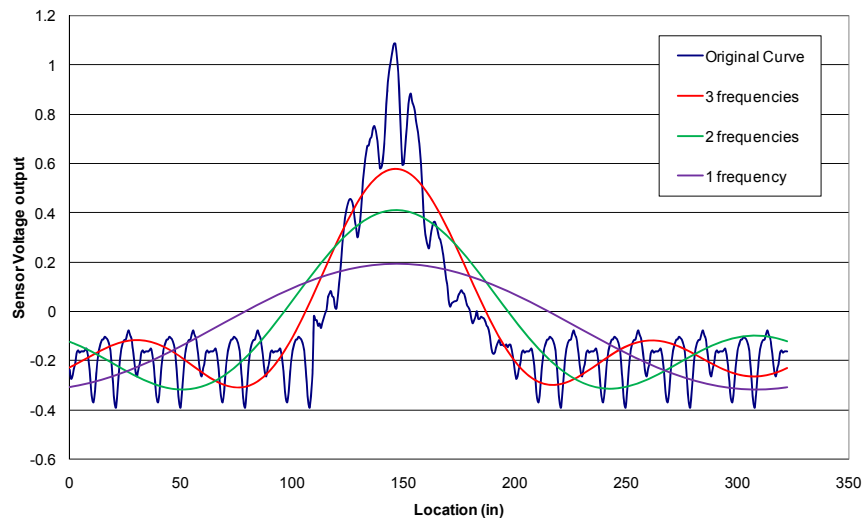

Figure C.7: Comparison of denoised curves considering one, two, and three frequencies
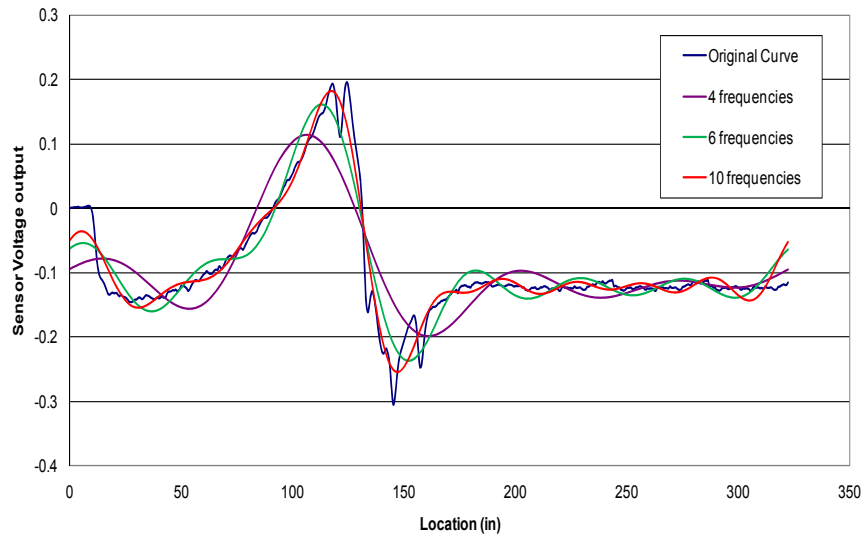
Figure C.8: Comparison of denoised curves considering four, six, and 10 frequencies

C.4   Conclusion

The FFT is an effective method for processing MFL test results.

The frequency and magnitude of the corroded region affect the magnetic field differently if compared with other signals caused by factors like transverse rebars. The curve can be denoised (filtered) by removing undesirable frequencies and keeping the major frequencies untouched.

This method can be very useful in processing and filtering MFL results, which would assist engineers to better analyze and comprehend laboratory and field results.

174

REFERENCES

1. Kusenberger, F.N. and Barton, J.R. (1981). "Detection of Flaws in Reinforcing Steel in Prestressed Concrete Bridge Members," *Final Report, Report No. FHWA/RD-81/087*, Federal Highway Administration.

2. Kusenberger, F.N. and Birkelback, R.S. (1983). "Detection of Flaws in Reinforcing Steel in Prestressed Concrete Bridge Members," *Final Report, Report No. FHWA/RD-83/081*, Federal Highway Administration.

3. Ghorbanpoor, A., Borchelt, R., Edwards, M., and Abdel Salam, E., (2000). "Magnetic-Based NDE of Prestressed and Post-Tensioned Concrete Members-The MFL System," *Publication FHWA-RD-00-026, FHWA*, U.S. Department of Transportation.

4. Makar, J.M. and Desnoyers, R. (2001). "Magnetic Field Techniques for the Inspection of Steel Under Concrete Cover," *Report No. NRCC-43699*, Canada.

5. Scheel, H. and Hillemeier, B. (2003). "Location of Prestressing Steel Fractures in Concrete," *Journal of Materials in Civil Engineering*, ASCE, Vol.15, No. 3, pp. 228-234.

6. Hillemeier, B. and Scheel, H. (2002). "Non Destructive Location of Prestressing Steel Fractures in Post Tensioned and Prestressed Concrete," (TRB) *Committee A2C03 – Concrete Bridges*, Washington, D.C., USA.

7. Valentine, F. (2000). *Effect of Debris-Induced Lift-off on Magnetic Flux Leakage Inspection Results*, M.Sc. Thesis, Department of Mechanical and Aerospace Engineering, Morgantown, West Virginia.

8. Ciolko, A.T. and Tabatabai, H. (1999). "Nondestructive Methods for Condition Evaluation of Prestressing Steel Strands in Concrete Bridges," *CTL, Inc.*, Skokie, Illinois.

9. Mix, P.E. (2005). "*Introduction to Nondestructive Testing*," John Wiley and Sons, Inc.

10. Ghorbanpoor, A. (November 2000). "Condition Assessment of External P-T Tendons in the Mid Bay Bridge," *Final Report - FDOT*.

11.   Ida, N. and Lord, W. (September 1983). "3-D Finite Element Predictions of Magnetostatic Leakage Fields," *IEEE Transactions on Magnetics*, Vol. MAG-19, No. 5, pp. 2260-2265.

12.   Babbar, V. and Clapham, L. (December 2003). "Residual Magnetic Flux Leakage: A Possible Tool for Studying Pipeline Defects," *Journal of Nondestructive Evaluation*, Vol. 22, No. 4, pp. 117-125.

13.   Cholowsky, S. and Westwood, S. (February 2004). "Tri-axial Sensors and 3-Dimensional Magnetic Modeling of Defects Combine to Improve Defect Sizing From Magnetic Flux Leakage Signals," *NACE International Corrosion Society*, Northern Area Western Conference.